

The study of cosmological radio backgrounds
with the Sunyaev-Zel'dovich effect

Mohammad Shehzad Emritte

A thesis submitted to the Faculty of Science,
University of Witwatersrand,
in the fulfilment of the requirements for the degree of
Doctor of Philosophy

Johannesburg, South Africa, 2017

Abstract

According to the standard model of cosmology, the Universe has evolved from a thermal bath of elementary particles and photons towards one comprising of collapsed structures such as stars, galaxies and clusters of galaxies. The Cosmic Microwave Background (CMB) spectrum and its angular anisotropy across the sky contain information on the physical processes, matter distribution and evolution of the Universe across cosmic time. Primordial spectral distortions of the CMB and its anisotropy can be studied through the inverse Comptonization process occurring in cosmic structures, known as the Sunyaev-Zel'dovich effect (SZE). This present study demonstrates how the SZE can be used to obtain information on the 21 cm background produced between the Dark Ages (DA) and the Epoch of Reionization (EoR), on Non-Planckian (NP) modifications of the CMB due to plasma frequency at the recombination epoch, and on the anisotropy of the CMB at cluster locations, through the study of the polarization of the SZE. To these aims, a full relativistic approach is employed, that allows us to calculate the spectra of the SZE and its polarization component with high precision, and allows to calculate it for any kind of electron population (thermal or non-thermal plasma), and for an input spectrum that can deviate from the standard black-body spectrum.

The SZE-21cm, which is the Comptonized spectrum of the modified CMB due to physical processes occurring during the DA and the EoR, is calculated for four models of the 21-cm background. A full spectral analysis of the signal is performed and the importance of relativistic effects are highlighted. The results demonstrate that relativistic effects are non-zero over the entire frequency spectrum and hence cannot be ignored, particularly for hot clusters. It is found that the amplitude of the SZE-21cm signal is of the order of μJy and is within the reach of the SKA instrument. Clusters with high temperature and optical depth are optimal targets to search for the SZE-21cm signal. The SKA can measure the signal in the frequency interval 75-90 MHz for clusters with temperature higher than 5 keV. Discerning the SZE-21cm from the standard SZE can be achieved using the SKA depending on the 21-cm background model for temperatures > 10 keV.

Using CMB spectral data at both low and high frequencies, upper limits (206, 346 and 418 MHz at 1, 2, 3 σ confidence level) are placed on NP effects associated with a non-zero

plasma frequency at the recombination epoch. The SZE_{NP} is derived for a CMB spectrum modified due to plasma effects using these upperlimits and a unique spectral feature is obtained. A peak occurs at the plasma frequency in the SZE_{NP} independent of cluster parameters and the possibility of measuring the plasma frequency with the SKA and eVLA is shown. Plasma effects are also investigated on the spectrum of the cosmological 21-cm background and it is found that such an effect is important to consider when recovering the history of the Universe during these epochs.

Polarization is a natural outcome of inverse Compton (IC) scattering and the anisotropy of the CMB plays a big role in the production of polarization in Comptonization process. The SZE polarization associated with the anisotropy of the CMB is derived in the full relativistic regime for any general electron distribution. The spectral shapes of the Stokes parameters induced by the IC scattering of the multipoles of the CMB for thermal and non-thermal electrons are derived, focusing mainly on the quadrupole and octupole which provide the largest possible detectable signals in cosmic structures. Our results demonstrate the implication of relativistic effects, which become important for high temperature or non-thermal cluster environments. When relativistic effects are accounted for, all the multipoles of the CMB are involved in the production of polarization. The octupole induced polarization spectrum reveals the existence of a cross-over frequency which is dependent on cluster parameters such as temperature, minimum momentum and spectral index. The possibilities to disentangle the quadrupole spectrum from the octupole one are discussed, which would allow the measurements of these multipoles at cluster locations. The generality of our approach allows us to calculate the SZE polarization spectra of the Bullet cluster using multifrequency SZE data in intensity and compare the results with the sensitivities of the SKA, ALMA, *Millimetron* and *CORE++* instruments.

Although the effects that we studied here are small, however, they are still within the detection limits of the SKA, due to its very high sensitivity. Therefore, the SKA will play a big role in the study of cosmological radio backgrounds by providing high precision SZE data.

Acknowledgements

I acknowledge the support from the Square Kilometre Array (SKA) and the continuous and enlightening supervision of Prof. S. Colafrancesco, the SKA Research Chair in radioastronomy at Wits University, and this was a great opportunity for me to work with such a great astrophysicist like him. He has been a very good source of guidance for me during these past 3 years. I am also very grateful for the support of the School of Physics and the Faculty of Science of Wits University and I show my appreciation for Prof Daniel Joubert as well as Prof John Carter. I am also very grateful to my friend Dr P. Marchegiani for his encouragement as well as the useful discussions that I've had with him. I am also very thankful to all my colleagues and the people at Wits, in particular Nebiha, Asha and Salome.

I also acknowledge Marco Tullio for his discussions and for giving me the right information concerning the work. Thanks also goes to my parents, Salim and Banon as well as my brothers Umar and Zeehad for always believing in me and supporting me from the start till the end of this journey. An appreciation also goes to Mr Sanjeevi Cuneapen, Mr Tamir Husam and Mr Jamil Laloo. I would like to also thank my cousins Anass and Yasmina Emritte, Mohammad and Surayya Santally and my uncle Yusuf Santally. Finally, I say thank you to Zainab Bassawon for the support.

Contents

1	Introduction	16
1.1	The Standard Model of Cosmology	18
1.1.1	Observational Evidence	20
1.1.2	Dark Matter	22
1.1.3	Dark Energy	23
1.1.4	Inflation	24
1.1.5	Structure Formation within the Λ CDM Model	24
1.2	Galaxy Clusters	26
1.2.1	Intracluster medium	27
1.2.2	Cosmic rays and non-thermal emissions	29
1.3	The Sunyaev-Zel'dovich effect (SZE)	30
1.3.1	The SZE spectrum	32
1.3.2	The relativistic SZE spectrum	33
1.3.3	Relevance of the SZE	37
1.4	Polarization of the SZE	38
1.4.1	Non-relativistic SZE polarization	38
1.4.2	Relevance of the SZE polarization	41
1.5	Objectives of this Thesis	42
2	The EoR and the SZE-21cm	43
2.1	The Cosmological 21-cm background	43
2.2	Physics of the 21-cm radiation	44
2.3	Measurement of the 21-cm background	45
2.4	The SZE of the 21-cm	46
2.5	The 21-cm background models	47
2.6	Derivation of the SZE-21cm	48
2.6.1	The SZE-21 cm spectrum	49
2.6.2	Spectral Analysis	51
2.7	Discussion	56

<i>CONTENTS</i>	5
2.7.1 Differential analysis techniques and foreground contamination	58
2.7.2 Detectability with the SKA	59
2.8 Conclusion	63
3 Non-Planckian effects	65
3.1 Observables	67
3.2 Spectral modification of the CMB spectrum	68
3.3 The SZE_{NP}	71
3.4 Modification to the 21-cm background	73
3.5 Discussions and conclusions	78
4 Relativistic SZE polarization in cosmic structures	80
4.1 The polarized Boltzmann equation	82
4.1.1 The distribution function in the Thomson approximation	85
4.1.2 Stokes parameters	89
4.1.3 The Stokes parameter I	90
4.1.4 Anisotropic incident CMB radiation	92
4.1.5 CMB multipoles and polarization of the SZE	97
4.2 Polarization spectra	101
4.2.1 Application to the Bullet cluster	107
4.3 Polarized IC scattering at high energies	109
4.4 Polarization spectra at high frequencies	110
4.5 Discussion and conclusions	111
5 Conclusions and remarks	116
A Fractional error analysis	127

List of Figures

1.1	The recessional velocities of galaxies against their distances showing the direct proportionality between the two quantities (Figure from Turner & Tyson 1999).	20
1.2	The abundances of deuterium, helium-3, lithium-7 and helium-4 Y as a function of the photon to baryon ratio, η . The measured abundances of the respective elements and the photon to baryon ratio by <i>WMAP</i> are shown by the horizontal lines and the vertical line respectively (Figure from Garrett & Duda 2011).	21
1.3	The blackbody spectrum of the CMB measured by <i>COBE-FIRAS</i> with error bars enlarged 400 times (Figure from Mather et al. 1994).	22
1.4	Bright galaxies used in the SDSS as tracers to produce 3D maps of the Universe (Eisenstein et al. 2011). Each dot represents a galaxy.	25
1.5	The galaxy cluster Abell 1989 observed by the Hubble space telescope (Figure from Kravtsov & Borgani 2012).	26
1.6	The Coma galaxy cluster in the X-ray band showing the existence of a hot ICM gas (Figure from Bohringer & Werner 2009).	28
1.7	Radio emission for several galaxy clusters illustrating the diffuse emission location and morphology (Figure from Feretti 2012).	30
1.8	The electron Lorentz factor plotted against the observed/critical frequency for different magnetic fields. It is clearly noticed for the radio bands and for magnetic field around the μG , this would roughly correspond to Lorentz factors within 10^3 to 10^6 (Govoni & Feretti 2004).	31
1.9	The spectral distortion of the SZE computed for a thermal electron distribution of optical depth $\tau = 10^{-3}$ for different temperatures $T_e = 1$ (red), 7 (purple), 15 (blue) keV in the relativistic (dotted) and non-relativistic case (solid).	35
1.10	The SZE spectrum of a non-thermal plasma of spectral index $\alpha = 2.5$ for $p_1 = 0.5$ (red), 1 (purple), 3 (blue). We use an optical depth $\tau = 10^{-4}$.	36

1.11	The Stokes parameter Q computed in the non-relativistic approach for a value $ a_{2,2} = 1.3 \times 10^{-5}$ and $\tau = 0.01$	40
2.1	The cosmological 21-cm brightness signal emitted by hydrogen starting from the DA ($z \approx 200$) down to the reionization ($z \approx 6$) (Furlanetto 2006, Pritchard & Loeb 2012).	45
2.2	The frequency dependence of the cosmological 21-cm brightness signal relative to the CMB, δT , calculated using the 21cmFAST code for four models: a fiducial model without dark matter (solid line, benchmark model), an extreme model without dark matter (dashed line) and two fiducial models with dark matter with $M_{\min} = 10^{-3} M_{\odot}$ (dot-dashed line) and $M_{\min} = 10^{-6} M_{\odot}$ (three dot-dashed line), where M_{\min} is the mass of the smallest DM halo (Colafrancesco et al. 2016b, Evoli priv.comm).	47
2.3	The SZE-21cm (solid line) calculated using the benchmark model (solid line in Fig 2.2) assuming an intracluster temperature of 7 keV and optical depth $\tau = 5 \times 10^{-3}$. The dashed line shows the standard SZE effect in the absence of the 21-cm perturbations (Colafrancesco et al. 2016b).	50
2.4	The standard SZE with no perturbation from the 21-cm for the case of a thermal electron gas of temperature 5 keV and optical depth $\tau = 5 \times 10^{-3}$ (solid line) and for the case of a non-thermal gas following a power-law distribution with minimum momentum $p_1 = 10$, $\alpha = 3.5$ and $\tau = 1 \times 10^{-4}$ (dashed line) (Colafrancesco et al. 2016b).	50
2.5	The SZE-21cm in the case of a thermal electron distribution illustrated for four different temperatures: 5 (solid), 10 (dashed), 15 (dot-dashed) and 20 (dash three dots) keV. A constant value of the optical depth, $\tau = 5 \times 10^{-3}$, is adopted (Colafrancesco et al. 2016b).	51
2.6	The fractional error between the relativistic and the non-relativistic approach plotted against frequency for thermal plasmas present in galaxy clusters with temperatures, 20 (solid line), 15 (dashed line) and 7 (dot-dashed line) keV (Colafrancesco et al. 2016b).	52
2.7	The difference, $\Delta T_{mod} - \Delta T_{st}$, between the SZE-21cm and standard SZE for galaxy clusters of temperatures 5 (solid), 10 (dashed), 15 (dot-dashed) and 20 (dash-three dots). The optical depth used is 5×10^{-3} (Colafrancesco et al. 2016b).	53
2.8	The SZE-21cm computed in the case of non-thermal electrons following a single power-law for values of the minimum momentum $p_1 = 0.1$ (solid line), 1 (dashed), 5 (dot-dashed), 10 (dash-three dots) and spectral index $\alpha = 3.5$. A value of $\tau = 1 \times 10^{-4}$ has been used (Colafrancesco et al. 2016b).	54

- 2.9 The difference between the SZE-21cm and the standard SZE, computed in the case of non-thermal electrons following a single power-law for values of the minimum momentum $p_1 = 0.1$ (solid line), 1 (dashed), 5 (dot-dashed), 10 (dash-three dots) and spectral index $\alpha = 3.5$. A value of $\tau = 1 \times 10^{-4}$ has been adopted (Colafrancesco et al. 2016b). 54
- 2.10 We show the SZE-21cm for a thermal plasma of temperature 7 keV and optical depth $\tau = 5 \times 10^{-3}$ in the standard benchmark model and for the case in which the background 21-cm is shifted by a factor of 3 in the frequency domain (Colafrancesco et al. 2016b). 55
- 2.11 We show the SZE-21cm for a thermal electron distribution of temperature 5 (left) and 20 keV (right) for each model as the background radiation; fiducial model without dark matter (solid), extreme model without dark matter (dashed line), two fiducial models with dark matter with $M_{min} = 10^{-3} M_{\odot}$ (dot-dashed line) and $M_{min} = 10^{-6} M_{\odot}$ (three dot-dashed line). A constant optical depth value of 5×10^{-3} is used (Colafrancesco et al. 2016b). 56
- 2.12 We show the SZE-21cm for non-thermal electron distributions of minimum momentum $p_1 = 0.1$ (left) and $p_1 = 10$ (right) for each model as the background radiation; fiducial model without dark matter (solid), extreme model without dark matter (dashed line), two fiducial models with dark matter with $M_{min} = 10^{-3} M_{\odot}$ (dot-dashed line) and $M_{min} = 10^{-6} M_{\odot}$ (three dot-dashed line). A constant optical depth value of 1×10^{-4} and spectral index $\alpha = 3.5$ are used (Colafrancesco et al. 2016b). 57
- 2.13 The SZE-21cm for thermal plasmas at 5 (short dashed line) and 20 (solid line) keV compared to the synchrotron emission for the Coma cluster with redshift $z_{\text{Coma}} = 0.02$ (Long dashed line) and for a Coma-like cluster at redshift $z = 1$ (dashed-three dots) (Colafrancesco et al. 2016b). 59
- 2.14 The surface brightness of the standard SZE calculated for a galaxy cluster at temperatures: 20 (solid line), 15 (dashed), 10 (dot-dashed) and 5 (three dots-dashed) keV assuming a value of $\tau_0 = 5 \times 10^{-3}$, $\theta_c = 300$ arcsec, $\beta = 0.75$ and $\theta_{\text{max}} = 10\theta_c$ (Colafrancesco et al. 2016b). 60
- 2.15 Left panel: The SZE-21cm (solid lines), ΔI_{mod} , and the standard SZE (dashed lines), ΔI_{st} , fluxes in μJy units. Right Panel: The absolute difference, $\Delta I_{\text{mod}} - \Delta I_{\text{st}}$, fluxes in the units of μJy . In both panels we are using the benchmark model, which is the one without extreme heating and in the absence of dark matter. The results are for thermal plasmas of temperature, 5 (cyan), 10 (red), 15 (black), 20 (green) keV computed for $\tau_0 = 5 \times 10^{-3}$, $\theta_c = 300$ arcsec, $\beta = 0.75$, $\theta_{\text{max}} = 10\theta_c$ (Colafrancesco et al. 2016b). 61

2.16	Same as Fig 2.15 but for the model without dark matter but with extreme heating (Colafrancesco et al. 2016b).	62
2.17	Same as Fig 2.15 but for the model with dark matter for $M_{min} = 10^{-3} M_{\odot}$ (Colafrancesco et al. 2016b).	62
2.18	Same as Fig 2.15 but for the model with dark matter for $M_{min} = 10^{-6} M_{\odot}$ (Colafrancesco et al. 2016b).	63
3.1	The non-Planckian spectral distribution of the CMB for different values of the plasma frequency ν_p as derived from the fit to the data. The experimental data are shown for both low (Howell & Shakeshaft 1967, Sironi et al. 1990, 1991) and high frequencies (Fixen et al. 1996). Other data in the range $\sim 1.3 - 50$ GHz obtained from ground-based, ballon-borne and from the <i>COBE-DR</i> experiment (see http://asd.gsfc.nasa.gov/archive/arcade/cmb_spectrum.html) are not shown here but they lie almost exactly along the curves of the CMB spectrum shown in the plot.	69
3.2	The non-Planckian effects due to a finite value of the plasma frequency ν_p on the CMB spectrum at $\nu < 1$ GHz for different values of the upper limit on ν_p as obtained from the fit to the CMB spectrum data (Colafrancesco et al. 2015a). Experimental data are from Howell & Shakeshaft 1967, Sironi et al. 1990, 1991.	70
3.3	The effect of a non-Planckian distribution on the CMB spectrum in frequency range 143 GHz to 191 GHz is shown for different values of the plasma frequency x_p (Colafrancesco et al. 2015a). Experimental data are from <i>COBE-FIRAS</i> (Fixen et al. 1996).	72
3.4	The thermal SZ effect spectral distortions computed for galaxy clusters with increasing plasma temperature (see various panels) for a standard Planck distribution (solid line) and including the effect of non-Planckian distribution of photons for the values of the plasma frequency x_p derived at 1σ , 2σ and 3σ level. The cluster plasma optical depth is fixed to the value $\tau = 0.001$ (Colafrancesco et al. 2015a).	74
3.5	The non-thermal SZE spectral distortion for the case of non-thermal plasmas with increasing electron minimum momentum p_1 (see various panels) for a usual Planck distribution (solid line) of photons and the effect of non-Planckian distribution at 1σ , 2σ and 3σ level computed in the case of a single power law for different minimum momentum p_1 . We use here an optical depth of $\tau = 0.001$ (Colafrancesco et al. 2015a).	75

3.6	The difference between the SZE_{NP} and the Planck SZE for a Bullet-like cluster with temperature of 15 keV (see Markevitch et al. 2002) subtending an angle of $5'$ to its R_{500} . An optical depth of $\tau = 0.001$ is assumed. The SKA1 (red) and SKA-50% (orange) sensitivity is calculated for 1000 hrs integration while the eVLA sensitivity (green) is calculated for 12 hrs integration (Colafrancesco et al. 2015a).	76
3.7	The change in brightness temperature $\delta\tilde{T}$ for $\nu_p = 0$ (solid line), $\nu_p = 0.2$ (dotted), 1 (dashed), 10 (dot-dashed), 20 (three dots-dashed) and 100 MHz (long dashed) as a function of the frequency (Colafrancesco et al. 2015a). . .	78
4.1	The redistribution function $P_{l,m}(s)$, for $l = 0, 1, 2, 3$ and $m = 0, 2$, for thermal electrons at different temperatures as indicated (Emritte et al. 2016).	95
4.2	The redistribution function $P_{l,m}(s)$, for $l = 0, 1, 2, 3$ and $m = 0, 2$, for a single power law distribution of electrons with spectral index $\alpha = 2.5$ for different minimum momenta p_1 (Emritte et al. 2016).	96
4.3	The spectrum of the Stokes parameter Q for different temperatures of a thermal electron distribution arising from the quadrupole (left) and octupole (right) of the CMB, assumed here to be $a_{2,2} = 1.3 \times 10^{-5}$ and $a_{3,2} = 8.7 \times 10^{-6}$, respectively. The red curve represents the non-relativistic Q . The optical depth value is $\tau = 0.001$ (Emritte et al. 2016).	97
4.4	The spectrum of the Stokes parameter Q for the quadrupole (left) and octupole (right) in the case of a single power law distribution of electrons of spectral index $\alpha = 2.5$. The quadrupole of the CMB is assumed here to be $a_{2,2} = 1.3 \times 10^{-5}$ and that of the octupole to be $a_{3,2} = 8.7 \times 10^{-6}$. The optical depth value is $\tau = 1 \times 10^{-5}$ (Emritte et al. 2016).	98
4.5	The spectrum of the Stokes parameter Q for the superposition of the CMB quadrupole and octupole for a thermal electron distribution (dashed curves in left panel) and for a non-thermal electron distribution (dashed curves in right panel). Optical depth values of 10^{-3} and 10^{-5} have been used for the thermal and non-thermal distributions, respectively. The spectral index of the power-law distribution is $\alpha = 2.5$. The straight curves represent the spectrum of Q where the contribution of only the quadrupole is considered (Emritte et al. 2016).	98
4.6	The spectrum of the Stokes parameter Q for the CMB quadrupole and octupole computed for different spectral index α of a single power-law distribution of electrons. The values of the minimum momentum and optical depth here are $p_1 = 1$ and 1×10^{-5} , respectively (Emritte et al. 2016).	100

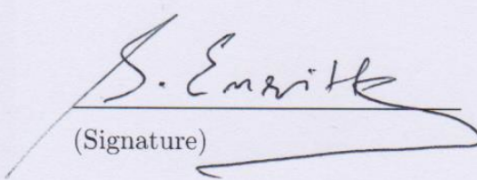
- 4.7 The spectrum of the Stokes parameter Q for the quadrupole (left panel) and the octupole (right panel) computed for a combination of two thermal electron populations (blue curves): a thermal electron population with $kT = 10$ keV and $\tau = 0.001$ (red curves) and another thermal electron population with $kT = 20$ keV and $\tau = 0.002$ (green curves) (Emritte et al. 2016). 101
- 4.8 The spectrum of the Stokes parameter Q for the CMB quadrupole (left panel) and octupole (right panel) for a thermal electron distribution with $kT = 10$ keV and $\tau = 10^{-3}$ (red curves) combined with a power-law electron distribution, spectral index $\alpha = 2.5$ and $\tau = 10^{-4}$, for different minimum momentum p_1 . The blue curves represent the resulting spectrum for different values of p_1 (Emritte et al. 2016). 102
- 4.9 The variation of the cross-over frequency ν_0 as a function of the electron temperature (top panel) for the case of a thermal distribution of electrons, of the minimum normalized momentum p_1 for a non-thermal electron distribution (mid panel) for a fixed $\alpha = 2.5$, and of the spectral index α (bottom panel) in the case of a power-law electron distribution for a fixed $p_1 = 1$ (Emritte et al. 2016). 104
- 4.10 The scattering of primordial CMB anisotropies in intensity for a plasma temperature of 20 KeV showing the spectrum of Quad-I (blue) and Oct-I (red) (Fig from Chluba & Dai 2014). The quantity x is the dimensionless frequency. 106
- 4.11 The polarization spectrum (dashed-red) of the Bullet cluster calculated over 5 arcmin². The dashed- blue curve is the quadrupole spectrum whereas the dotted-blue is that of the octupole. The green curves represent the non-thermal quadrupole (dashed green) and octupole (dotted green). The brown, purple and the black curves represent the sensitivity of SKA, ALMA and *Millimetron* for 260 and 1000 hrs of integration. The yellow curve represents the sensitivity of CORE++ (Emritte et al. 2016). 108
- 4.12 The polarized IC scattering of the CMB associated with the quadrupole (blue) and octupole (green) computed in the X-ray (left) and gamma-ray (right) bands for $p_1 = 1, 10, 100$ (bottom to top) and for $\alpha = 3.7$. In the left panel, we also show the sensitivity of *Chandra* for 5000 hrs at 3 sigma as well as *ASTROH-HXI* for 5000 hrs at 3 sigma. We also show in the right panel the sensitivity of AstroMeV for 10 years at 3 sigma, *FERMI* for 10 years at 5 sigma, H.E.S.S. and CTA at 5 sigma for 5000 hrs. 110

A.1	Spectral analysis of the first model (solid line of Fig 2.2).Top-panel :The relativistic (solid) and non-relativistic SZE-21cm (dashed line) together with the standard relativistic (long-dashed line) and non-relativistic SZE (dotted line) calculated for a thermal plasma of temperature 7 keV and optical depth 5×10^{-3} . Middle-panel: The fractional difference between the relativistic and non-relativistic results. Bottom-panel: Second derivative of the input spectrum.	129
A.2	Same as Fig A.1 for the second model (dashed line in Fig 2.2).	130
A.3	Same as Fig A.1 for the third model (dashed line in Fig 2.2).	131
A.4	Same as Fig A.1 for the fourth model (dashed line in Fig 2.2).	132

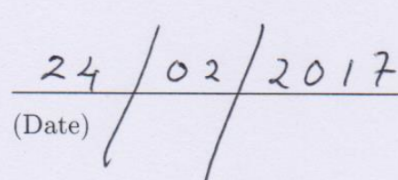
List of Tables

Declaration

I declare that this Thesis is my own, unaided work. It is being submitted for the Degree of Doctor of Philosophy of Science to the University of the Witwatersrand, Johannesburg. It has not been submitted before for any degree or examination to any other University.



(Signature)



(Date)

Declaration

This work is based on three published papers by the author during the three years of his PhD.

1.

Title: Probing the physics and history of cosmic reionization with the Sunyaev-Zel'dovich effect

Authors: Colafrancesco, S., Marchegiani, P. & Emritte, M. S.

Journal: Astronomy & Astrophysics (A&A), 2016, 595, A21 [DOI: 10.1051/0004-6361/201424904]

2.

Title: The impact of Non-Planckian effects on cosmological radio backgrounds

Authors: Colafrancesco, S., Emritte, M.S. & Marchegiani, P.

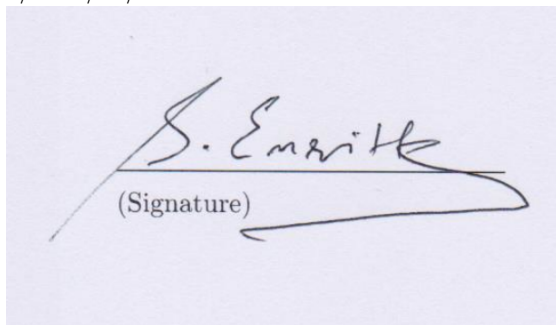
Journal: Journal of Cosmology and Astroparticle Physics (JCAP), 2015, 05, 006 [DOI:10.1088/1475-7516/2015/05/006]

3.

Title: Polarization of the Sunyaev-Zel'dovich effect: relativistic imprint of thermal and non-thermal plasma

Authors: Emritte, M.S., Colafrancesco, S. & Marchegiani, P.

Journals: Journal of Cosmology and Astroparticle Physics (JCAP), 2016, 07, 031 DOI:10.1088/1475-7516/2016/07/031



(Signature)

Chapter 1

Introduction

Astronomy, which is the study of the Universe and its constituents, dates back to the dawn of humanity and is without a doubt one of the oldest if not the oldest among the natural sciences. At a very young stage during early civilizations (Babylonians, Greeks etc), astronomy was practiced only with the naked eyes, observing and predicting the positions of objects in the sky without any understanding of the processes involved. Since then, the human race has always been fascinated with the sky and a lot of questions regarding the Universe have always been asked, ranging from rather simple questions such as "what is the Sun?" up to "How did the Universe begin, what is it made up of and why does it look the way it is". However most of the questions regarding the Universe and its constituents require modern observational instruments and strong understanding of physical laws in order to be answered.

Within the last hundred years, we have seen an exponential improvement in the sensitivities and angular resolutions of telescopes. Furthermore, we have also been able to extend the spectral region over which we observe the sky. In this time and age, astronomical observations are done over the whole electromagnetic spectrum, ranging from radiowave (MHz) up to Gamma rays (TeV). These observations together with our increased understandings of physical laws throughout the years, have allowed us to probe the constituents, phenomenae and evolution of the Universe.

Thanks to modern observational techniques, we currently know that the Universe structures itself on different scales from small systems such as the Solar system, up to bigger ones such as galaxies which are accumulations of billions of stars and farther up to giant systems such as clusters of galaxies containing from hundreds up to thousands of galaxies. The structure and evolution of the Universe can be understood using a theoretical framework, known as the standard model of concordance cosmology, stemming from Einstein theory of general relativity and the Cosmological principle. The former is a theory of the force of gravity, which on cosmological scales rules over other forces such as electromagnetic, weak and

strong nuclear forces. The second, which is the cosmological principle, is a statement that the Universe is isotropic and homogeneous over large scales ($\gtrsim 100$ Mpc scales). Deeper observations have suggested that the Universe consists mainly of two exotic components, dark matter and dark energy and this have lead to further parameterization of our cosmological model. The standard model of cosmology has been the most successful model in allowing us to give a physical explanation to cosmological data.

Measurements of the Cosmic Microwave Background (CMB) spectrum by *COBE-FIRAS* (Fixen et al. 1996) and its fluctuations across the sky by *WMAP* (Bennett et al. 2003, Bennett et al. 2013, Hinshaw et al. 2013) and *Planck* (Ade et al. 2016a, 2016d), has put the standard model of cosmology on a firm observational basis. The isotropy and the blackbody spectral shape of this radiation is a direct natural consequence of an earlier, denser and hotter phase of the Universe (Smoot 1997, Padmanabhan 2002, Dodelson 2003). Within the standard model of cosmology, the Universe started ≈ 14 billions years ago from a singularity popularly known as the Big Bang. Since then, the Universe has been expanding and has evolved through several stages until today. The observed CMB anisotropy is an indication that formation of structures started as tiny inhomogeneities in the primordial matter distribution. The spectrum and the angular distribution of the CMB encode important information regarding the energetics and matter distribution since the recombination epoch, when the Universe was ≈ 400000 years old (Peebles 1993, Padmanabhan 2002, Dodelson 2003, Ade et al. 2016b). The CMB spectrum is sensitive to various physical processes (Furlanetto et al. 2006, Chluba & Sunyaev 2012, Chluba 2014) that occurred during the evolution of the Universe. An important phase in the history of the Universe is its evolution from the recombination epoch (redshift $z_{\text{rec}} \approx 1100$) through the Dark Ages (DA) ($z \approx 1100$ to 20) down to the epoch of reionization (EoR) ($z \approx 20$ to 6) (see e.g. Peebles 1993, Padmanabhan 2002, Furlanetto et al. 2006, Pritchard & Loeb 2012). Many physical processes during these epochs can leave an imprint on the CMB radiation and thus allowing us to access these epochs.

The CMB also interacts with the plasmas hosted by large-scale structures such as galaxy clusters and lobes of radio-galaxies. This interaction, known as the Sunyaev-Zel'dovich effect (SZE), causes a spectral distortion to the CMB radiation (Sunyaev & Zel'dovich 1970, Sunyaev & Zel'dovich 1972, Birkinshaw 1999, Ensslin & Kaiser 2000, Colafrancesco et al. 2003). Polarization is also an eventual outcome of this process, which can be induced by different mechanisms (Sazonov & Sunyaev 1999, Challinor et al. 2000, Lavaux et al. 2004, Portsmouth & Bertschinger 2004a, 2004b, Emritte et al. 2016). The SZE and its polarization can be used to study the atmosphere of large-scale structures and also as a probe to investigate various aspects of cosmology (Carlstrom et al. 2002, Colafrancesco 2009).

One interesting realization is that any spectral distortions of the CMB due to various physical processes in the early Universe will also be present in the SZE spectrum (Cooray 2006, Colafrancesco et al. 2015a, Colafrancesco et al. 2016b). Therefore, this presents us with the possibility of using the SZE as a probe of primordial physical processes using nearby large scale structures. Adding on that, the polarization component of the SZE gives an idea on the anisotropy of the CMB other than our location (Kamionkowski & Loeb 1997, Challinor et al. 2000, Lavaux 2004, Portsmouth 2004, Yasini & Pierpaoli 2016), where cosmic structures reside. Therefore the SZE and its polarization present themselves as a nearly complete package for testing many aspects of the cosmos.

In this present work, we look first in chapter 2, at the possibility of probing the EoR using the SZE produced by large scale structures such as galaxy clusters or the lobes of radio-galaxies. We perform our calculation in the full relativistic limit and in a way that incorporates any electron distribution. Secondly in chapter 2, we investigate on the possibility of non-Planckian (NP) effects on the CMB spectrum associated with a non-zero plasma frequency at the recombination epoch and thirdly in chapter 4, we perform a detailed study of the SZE polarization induced by the CMB anisotropy.

Throughout this work, we use a flat, vacuum-dominated cosmological model with $\Omega_m = 0.308$, $\Omega_\Lambda = 0.692$ and $H_0 = 67.8 \text{ km s}^{-1} \text{ Mpc}^{-1}$ (Ade et al. 2016b).

1.1 The Standard Model of Cosmology

The Standard Model of Concordance Cosmology is based on the metric solutions to the Einstein field equations (see e.g. Carroll 1997, Padmanabhan 2000, Padmanabhan 2002, Dodelson 2003). The latter governs the dynamic of spacetime whereby matter and radiation act as gravitational sources. The equation can be written as follows

$$G_{\mu\nu} = R_{\mu\nu} - (R/2)g_{\mu\nu} = \frac{8\pi G}{c^4}T_{\mu\nu} - \Lambda g_{\mu\nu} , \quad (1.1)$$

where c is the speed of light, $R_{\mu\nu}$ is the Ricci tensor, $g_{\mu\nu}$ is the metric, $T_{\mu\nu}$ is the matter/radiation energy-stress tensor, G is the Newton's gravitational constant and Λ is the cosmological constant. The solution that satisfies the above equation is the Friedmann-Lemaitre-Robertson-Walker (FLRW) metric:

$$ds^2 = c^2 dt^2 - a(t)^2 \left[\frac{dr^2}{1 - Kr} + r^2(d\theta^2 + \sin^2\theta d\phi^2) \right] , \quad (1.2)$$

where $a(t)$ is the scale factor and K is the curvature which can take values, 1, -1 and 0. This metric is obtained by enforcing the Cosmological principle, that is the isotropy and homogeneity of the Universe. Inserting this metric into eq 1.1, one obtains the Friedmann

equations which govern the evolution of the scale factor $a(t)$ as follows

$$\begin{aligned} \left(\frac{\dot{a}}{a}\right)^2 &= \frac{8\pi G}{3}\rho - \frac{Kc^2}{a^2} + \frac{\Lambda c^2}{3} \\ \frac{\ddot{a}}{a} &= -\frac{4}{3}\pi G\left(\rho + \frac{3p}{c^2}\right) + \frac{\Lambda c^2}{3}, \end{aligned} \quad (1.3)$$

where $\rho = \rho_r + \rho_m$ is the energy density (sum of matter and radiation) and p is the pressure. Combining the Friedmann equations results in an energy conservation equation

$$\frac{d}{dt}\left[a^3\rho c^2\right] + p\frac{d}{dt}\left[a^3\right] = 0, \quad (1.4)$$

which is a relation between the scale factor a and the energy densities. The Hubble parameter $H(t)$, which is measure of the expansion rate of the Universe, is defined as

$$H(t) = \frac{\dot{a}}{a}, \quad (1.5)$$

and the Hubble parameter at our present epoch, is denoted as H_0 which has been measured recently by *PLANCK* to be $67.8 \text{ km s}^{-1} \text{ Mpc}^{-1}$ (Ade et al. 2016b). The critical density of the Universe is defined by

$$\rho_{\text{crit}} = \frac{3H^2}{8\pi G}, \quad (1.6)$$

with its present value, $\rho_{\text{crit},0} = 3H_0^2/8\pi G = 8.63 \times 10^{-27} \text{ kg m}^{-3}$. The Hubble parameter is related to the energy densities through the first Friedman equation. In order to show this, we first define the dimensionless densities, which are also known as cosmological parameters, as follows

$$\Omega_r = \rho_r/\rho_c \quad (1.7)$$

$$\Omega_m = \rho_m/\rho_c \quad (1.8)$$

$$\Omega_\Lambda = \rho_\Lambda/\rho_c \quad (1.9)$$

$$\Omega_K = \rho_K/\rho_c, \quad (1.10)$$

where ρ_r is the radiation energy density, ρ_m is the matter energy density, $\rho_\Lambda = \Lambda c^2/(8\pi G)$ and $\rho_K = -3Kc^2/(a^2 8\pi G)$.

Using the energy conservation equation, eq 1.4, one can obtain equations that describe the evolution of matter ($\rho_m \propto 1/a^3$) and radiation ($\rho_r \propto 1/a^4$) with time. Then using these equations and the definition of the cosmological parameters, we can write the first Friedmann equation as follows

$$H(t) = H_0\sqrt{\frac{\Omega_{m,0}}{a^3} + \frac{\Omega_{r,0}}{a^4} + \Omega_\Lambda + \frac{\Omega_{K,0}}{a^2}}, \quad (1.11)$$

where $\Omega_{m,0}$, $\Omega_{r,0}$, $\Omega_{\Lambda,0}$ and $\Omega_{K,0}$ are values of the cosmological parameters at our current epoch. Eq 1.11 can be used to show that the standard model of concordance cosmology implies a Universe which is expanding adiabatically.

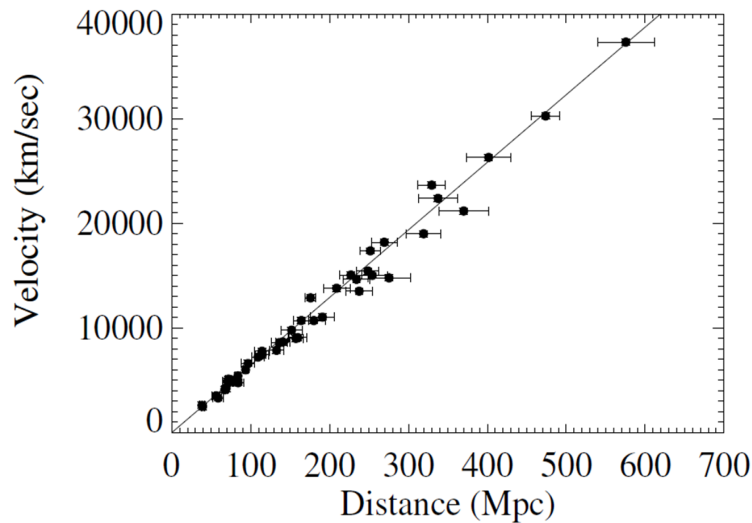


Figure 1.1: The recessional velocities of galaxies against their distances showing the direct proportionality between the two quantities (Figure from Turner & Tyson 1999).

1.1.1 Observational Evidence

The FLRW metric predicts that the Universe must have originated from a classical singularity, which is known as the Big Bang and has been expanding since then. One of the first evidence supporting the expansion of the Universe was discovered around the 1920s. The observed spectra of far away galaxies are found to be shifted towards the red portion of the electromagnetic spectrum. This shift, known as the cosmological redshift, implies that these celestial objects are moving away from our location point. With a detailed analysis of the observations, a relation between the recessional velocities V_{rec} of these objects and their distances D from us, was formulated and is known as the Hubble's law written as follows (Peebles 1993)

$$V_{rec} = H_0 D, \quad (1.12)$$

This relation (which is valid for $z \ll 1$) is in direct agreement with the suggestion that the Universe is expanding.

A second evidence pointing towards the standard model of cosmology lies in the observation of light elements in the Universe (Padmanabhan 2002). By a few seconds after the Universe had emerged from its singularity, the temperature dropped down to \approx few MeV due to cosmological expansion. It is predicted in theory that light elements would have started to be produced by that time (see Sarkar 1996, Steigman 2003). Collision between proton and neutron would lead to the formation of deuterium. Further collisions of deuterium with protons and neutrons would lead to helium, some tritium and lithium. The Big Bang nucleosynthesis (BBN) theory predicts that 25 % of the baryonic matter in the Universe would be in the form of helium, 0.001 % in deuterium and smaller quantities of

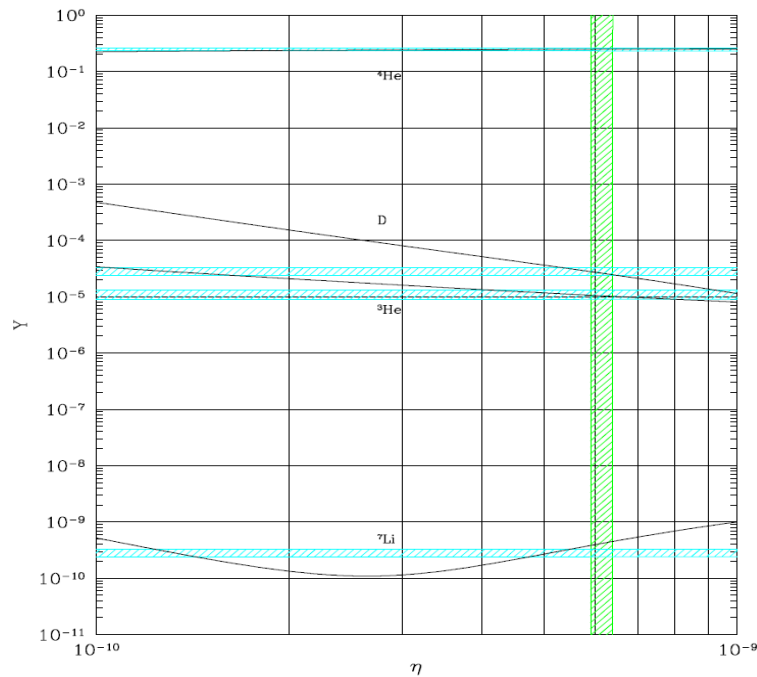


Figure 1.2: The abundances of deuterium, helium-3, lithium-7 and helium-4 Y as a function of the photon to baryon ratio, η . The measured abundances of the respective elements and the photon to baryon ratio by *WMAP* are shown by the horizontal lines and the vertical line respectively (Figure from Garrett & Duda 2011).

lithium. The BBN prediction (see Fig 1.2) is in agreement with observations (Sarkar 1996, Steigman 2003, Garrett & Duda 2011).

Another pillar evidence supporting our current cosmological model is the discovery of the Cosmic Microwave Background (CMB) radiation (Penzias & Wilson 1965). The measured blackbody spectral shape of the radiation by *COBE-FIRAS* (see Fig 1.3) (Fixen et al. 1996) implies that matter and radiation were in thermal equilibrium at earlier times and this radiation is a snapshot of the early Universe around $z \approx 1100$ when radiation decoupled from matter (Dodelson 2003). That moment is known as the recombination epoch and the temperature of the CMB, $T_{\text{CMB}}(z)$, at that redshift ($z_{\text{rec}} = 1100$) was ≈ 3000 K. By the time this radiation reaches us, its temperature has cooled down due to cosmological expansion. The temperature of the CMB is measured today as, $T_{\text{CMB}}(z = 0) = T_0 = 2.725 \pm 0.001$ K, and the radiation is found to be very near to isotropic with small anisotropy on the level of $\delta T/T_0 \approx 10^{-5}$ (Mather et al. 1990, Smoot et al. 1994, Smoot 1997). This is evidence supporting the idea that the Universe is largely isotropic, which supports the cosmological principle and hence favors the FLRW metric.

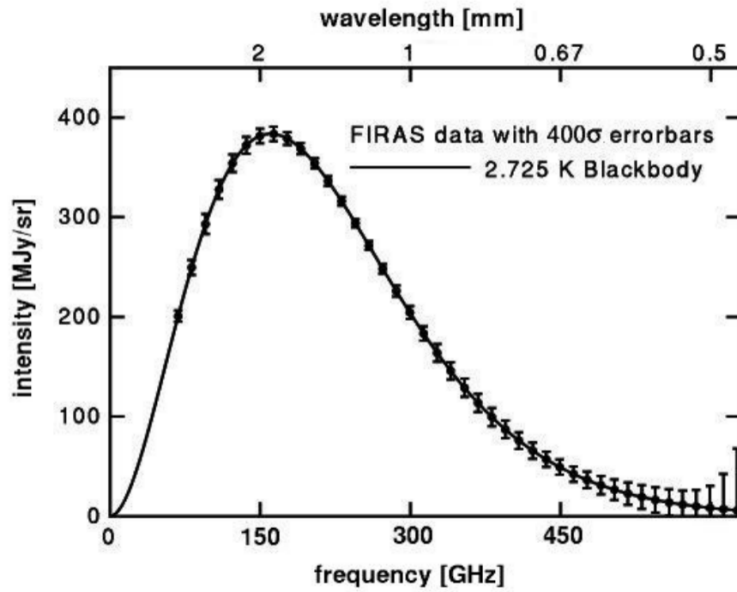


Figure 1.3: The blackbody spectrum of the CMB measured by *COBE-FIRAS* with error bars enlarged 400 times (Figure from Mather et al. 1994).

1.1.2 Dark Matter

In order to account for many observations that could not be explained with the standard model of cosmology, ingredients had to be added to the model. One of those ingredients is dark matter (see e.g. Einasto 2009, Garrett & Duda 2011), an exotic form of matter that permeates the whole Universe. It makes up $\approx 84\%$ of the matter content of the Universe as measured by *Planck* (Ade et al. 2016b). It is found that Dark matter does not interact with normal matter except via the force of gravity and this is the main suggestion of its non-baryonic nature.

One of the first pieces of evidence of dark matter lies in the study of the Coma cluster of galaxies and the high observed velocity dispersion of the galaxies (Zwicky 1933). Applying the virial theorem to the cluster, the visible matter cannot account for the high velocity of the galaxies (Trimble 1987), which suggest that more matter has to be present. Similar scenarios have also been observed in galaxies where the observed rotational curves could not be explained by the presence of only baryonic masses.

The existence of dark matter can also be inferred from the CMB temperature fluctuations (Hu & Dodelson 2002, Einasto 2009, Garrett & Duda 2011), the latter which is interpreted as the imprints of tiny variations in the density of matter around the recombination epoch. Before recombination, ordinary matter were tightly coupled to the photons and they behaved as single entity known as the photon-baryon fluid. Fractional overdensities in ordinary matter distribution around this time couldn't grow because they were tightly coupled to the photons of the CMB. After recombination, overdensities were then

able to grow through gravitational attraction leading to the structures we observed today. However, the observed CMB temperature fluctuation is around the order of $\approx 10^{-5}$ which would not have enough time to grow and produce the structures that we observed today. On the other hand, dark matter overdensities can grow independently since it is not coupled to the photons and baryons and were able to start the structure formation process much earlier. What we observed as variation in the CMB temperature $\approx 10^{-5}$ is the imprint of the photon-baryon oscillation in the potential well of dark matter (see Zackrisson 2005).

Gravitational lensing of far away galaxies also indicates the presence of dark mass in clusters of galaxies. The images of these background galaxies are seen to be distorted and the amount of mass suggested by gravitational lensing measurements are more than what is visible in the clusters (Blandford & Narayan 1992, Bradac et al. 2006, Clowe 2006) .

The nature of dark matter is still unknown till today, however many candidate particles have been proposed such as the WIMPs (weakly interacting massive particles) and axions (Bertone et al 2005, Abazajian et al. 2007, Skivie 2009). A favorite candidate among the WIMPs is the neutralino, which through mutual pair annihilation produces standard model particles which emit radiation over various frequencies from radio up to gamma-rays (Colafrancesco et al. 2015b, Colafrancesco et al. 2016b). Dark matter induced emissions from large scale structures are expected to be measured with the Square Kilometer Array (SKA) (Colafrancesco et al. 2015b).

1.1.3 Dark Energy

Observations of Type-Ia supernovae, which are high redshift distance indicators, suggest that the Universe is in a state of acceleration (Riess et al. 1998, Perlmutter 1999). In order to account for this acceleration, the standard model of cosmology requires a non-zero value of the cosmological constant (≈ 0.69). This implies that space is filled with an unknown form of energy which has an anti-gravity effect responsible for the observed accelerated expansion. This hypothesized form of energy is called dark energy. Further evidence of dark energy comes from cosmological parameters derived from measurements of CMB temperature anisotropies (Spergel et al. 2003, 2007, Komatsu et al. 2009, 2011, Ade et al. 2016b, Ade et al. 2016d) and baryon acoustic oscillations in large samples of galaxies (Eisenstein et al. 2005, Beutler et al. 2011, Ding et al. 2015). These observations indicate that dark energy is the dominant form of energy in the cosmos with $\Omega_{\Lambda,0} = 0.692 \pm 0.012$.

The nature of dark energy is still unknown, but nevertheless, quintessence models (whereby dark energy is in the form of a time-varying scalar field) have been put in place to explain its nature (Yoo & Watanabe 2012). These models are characterized by an equation of state which in the general form can be written as

$$p_Q = w_Q \rho_Q \tag{1.13}$$

where p_Q and ρ_Q are the pressure and energy density respectively, associated with the dark energy. The parameter w_Q takes different values depending on the dark energy model employed. For quintessence models, W_Q is always greater than -1 and for W_Q approaching -1 the cosmological constant is retrieved.

Alternative models, other than dark energy models, has also been put forward to explain the accelerated expansion of the Universe. These models are based on modified gravity theories (see Yoo & Watanabe 2012), whereby the accelerated expansion is due to some form of modification to gravity (Yoo & Watanabe 2012).

1.1.4 Inflation

Cosmological parameters measurement, originally by *WMAP* (Bennett et al. 2003, Bennett et al. 2013, Hinshaw et al. 2013) and later by *Planck* (Ade et al. 2016b), have shown that the Universe at present has a flat geometry ($|\Omega_{K,0}| < 0.005$) or very close to flat. This means that the density of the present Universe is very close to its critical density and therefore is in a well balanced state between a positively and negatively curved one. At early times near the Big Bang, the density would have had to be even closer to the critical density as any deviation would have been magnified over time. This imply that the initial conditions of the early Universe must have been finely tuned and this have lead to the fine tuning problem. Another problem within the model is the horizon paradox, that is opposite patches of CMB are observed to be in thermal equilibrium although these two patches appear to be causally disconnected.

In order to solve these inadequacies, a mechanism called inflation had to be invoked which says that Universe underwent through a period of accelerated exponential expansion from 10^{-35} to 10^{-33} s after its emergence from the Big Bang singularity. This rapid expansion would erase any curvature present and keeps the geometry of the Universe flat. Inflation also solves the horizon paradox because the disconnected patches were in thermal contact prior to inflation and were later driven apart by the extremely rapid expansion (see e.g. Senatore 2016).

With the addition of dark matter, dark energy and inflation to the standard model of cosmology, the standard model of cosmology is referred to as the Λ CDM model.

1.1.5 Structure Formation within the Λ CDM Model

Large scale surveys such as Sloan Digital Sky Survey (SDSS) (Eisenstein et al. 2011) and 2dF Galaxy Redshift Surveys (2dFGRS) (Colless et al. 2001) over a large portion of the sky, have successfully produced 3D maps of the structure of the Universe (see Fig 1.4). These surveys show us that the Universe is very close to homogeneous over scales $\gtrsim 100$ Mpc. On the other hand, for scales $\lesssim 100$ Mpc, the Universe looks inhomogeneous with structures

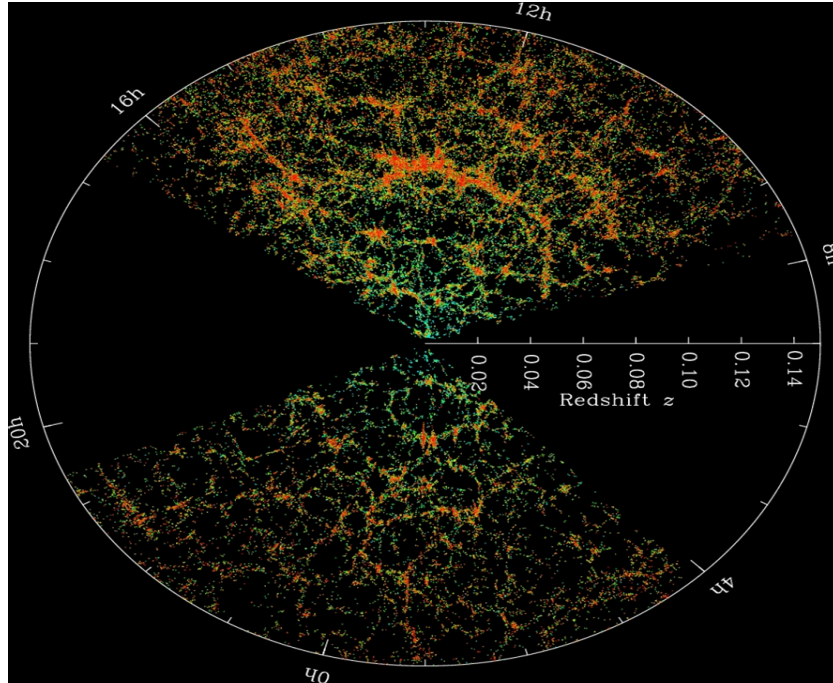


Figure 1.4: Bright galaxies used in the SDSS as tracers to produce 3D maps of the Universe (Eisenstein et al. 2011). Each dot represents a galaxy.

ranging in sizes from our solar system up to large superclusters of galaxies consisting of up to 1000 galaxies.

The formation of structures such as stars, galaxies and clusters of galaxies can be explained within the Λ CDM model by overdensities in the matter distribution around the recombination epoch. These overdensities are then amplified by the force of gravity which then lead to the clustering of matter at regions in space. These regions grow with cosmic time until structures such as galaxies and clusters of galaxies are eventually formed (see e.g. Padmanabhan 2002). Dark matter played an important role in the structure formation process since it was able to collapse before recombination (Primack 2015).

The formation of structures as a result of primordial inhomogeneities in matter distribution involving cold dark matter, imply that structures are formed in a hierarchical "bottom-up" scenario. Smaller structures are formed first, which then later grow due to gravitational forces until large scale structures such as galaxies, groups and galaxy clusters are formed (Kolb & Turner 1990, Yoshida 2009).

The seeds of these inhomogeneities in the matter distribution originated around the inflationary epoch. Inflation tends to drive the Universe towards a simple state, smoothing any curvature, anisotropies and inhomogeneities, but quantum fluctuations in the inflationary field lead to tiny inhomogeneities which are later amplified by the force of gravity. Over super-Hubble scales, these fluctuations can be described by a Gaussian random field,

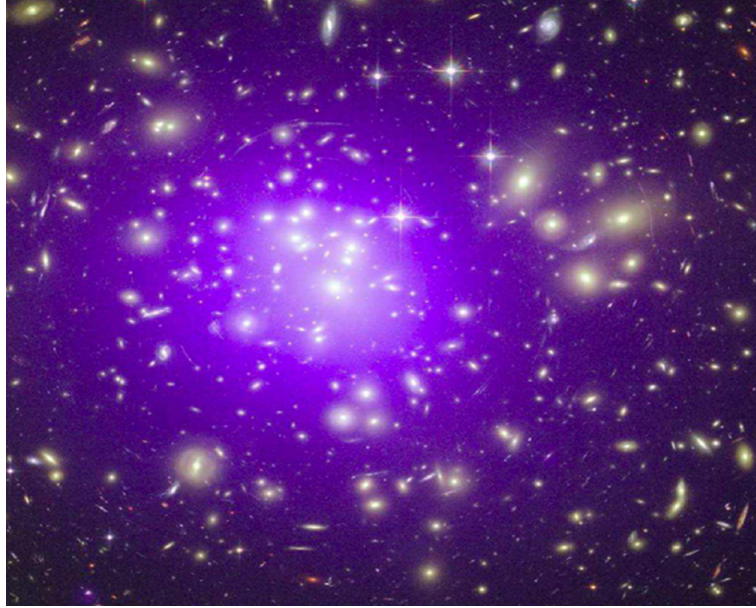


Figure 1.5: The galaxy cluster Abell 1989 observed by the Hubble space telescope (Figure from Kravtsov & Borgani 2012).

$$P(k) \propto Ak^n \text{ with } n \approx 1 \text{ (Baumann 2009).}$$

1.2 Galaxy Clusters

Galaxy clusters are large gravitationally bound cosmic structures, which consist of around 100 to 1000 galaxies distributed spatially over a volume of $\approx 1 \text{ Mpc}^3$. The masses of these objects are $\approx 10^{14} M_{\odot}$ and lies at the top of the hierarchy in the current structure formation paradigm. These objects were first identified via visual inspection and with further optical observations, the Abell catalogue containing many clusters were made. This catalogue provided the first statistical sample of clusters which has subsequently led to the systematic studies and morphological classification of these structures. It is found that these systems can be classified based on their shapes. Some are very irregular with strong subclustering, no central concentration and mainly consisting of spiral galaxies while others are very regular, displaying a smooth centrally condensed galaxy distribution with only few spiral galaxies (see e.g. Sarazin 1986). Fig 1.5 shows the optical image of the cluster Abell 1989 observed by the Hubble space telescope.

According to our current structure formation paradigm, galaxy clusters are formed by a hierarchical process whereby matter is accumulated over cosmic time by the action of gravity. According to this process, smaller units such as galaxies, groups and smaller clusters are built first and with the continuous gravitational pull, galaxy clusters comprising of hundreds to thousands of galaxies are finally formed. This assembling process is known as merger

and these merging events are very energetic events, involving kinetic energies $\approx 10^{64}$ ergs (Govoni & Feretti 2004, Kravtsov & Borgani 2012, Feretti 2012).

Although at optical wavelength, galaxy clusters appear to be just a collection of galaxies over large cosmological distances, modern observations have shown that this is not the case. Actually it has been observed that the galaxies make up only a few percent ($\approx 3\%$) of the matter content of galaxy clusters. Gravitational lensing measurements (Blandford & Narayan 1992, Bradac et al. 2006, Clowe 2006) have demonstrated that the main matter content in galaxy clusters is in the form of dark matter, which comprises around 85% of the mass of the structure. Observations in X-rays (see e.g. Sarazin 1986, Bohringer & Werner 2009, Arnaud et al. 2010) have shown that the space in between galaxies is not empty but is filled with a hot gas called the intracluster medium (ICM), which is the main baryonic component in clusters (comprising $\approx 12\%$ of the matter content). X-rays together with gravitational lensing measurements of the Bullet cluster have provided empirical evidence on the nature of dark matter.

1.2.1 Intracluster medium

Galaxy clusters were first recognized as X-ray sources around the 1970s when emission was first detected in the Virgo cluster (see e.g. Sarazin 1986 for complete historical review). Subsequently, more and more clusters were identified in the X-ray band such as the Coma cluster and Perseus cluster (Kravtsov & Borgani 2012, Sarazin 1986). The X-ray emission regions of clusters are extended and therefore cannot be attributed to any specific galaxies. This revealed the existence of the ICM and modern observations by current instruments such as *Chandra* and *XMM-Newton* have firmly established that the ICM is the main baryonic component of clusters ($\approx 12\%$). Currently, the ICM has been extensively observed and studied for many clusters of galaxies (see e.g. Ota & Mitsuda 2004, Arnaud et al. 2010, Reichert et al. 2011). Fig 1.6 shows the Coma cluster of galaxies in the X-ray region of the electromagnetic spectrum.

The ICM is a hot plasma whose electron temperature, T_e , can range from around ≈ 1 keV up to ≈ 17 keV (Sanderson & Ponman 2010, Reichert et al. 2011, Wik et al. 2014) and the electron number density ranges from 10^{-4} up to 10^{-2} cm^{-3} (Sarazin 1986). Although many mechanisms have been suspected for the X-ray production at this temperature, thermal bremsstrahlung (Rybicki & Lightman 1979) is the one that is most consistent with the spectra of observed clusters in the X-ray band (see Bohringer & Werner 2009). The bolometric X-ray luminosity, $L_X \propto n_{e,\text{th}} T_e^{1/2}$ of the ICM where $n_{e,\text{th}}$ is the thermal electron number density, is around $\approx 10^{44}$ up to $\approx 10^{46}$ erg/s.

Galaxy clusters are treated as self-similar objects, which means that a cluster of higher mass is a scaled-up version of one with lower mass. This relies on the assumption that



Figure 1.6: The Coma galaxy cluster in the X-ray band showing the existence of a hot ICM gas (Figure from Bohringer & Werner 2009).

galaxy clusters are formed from gravitational collapse of matter in the Universe and that the sole input of energy into the ICM comes from the gravitational potential energy. This eventually establishes an equilibrium configuration after the collapse and the virial theorem ($E_k = -1/2E_p$) can be applied to clusters. Based on that, the temperature measured from X-ray emission is a direct measure of the mass of the cluster (including dark matter) and indirectly the gravitational potential. Assuming the ICM is an ideal gas, the temperature-mass relation would follow, $T \propto M^{2/3}$. From this onwards, other physical quantities can be derived (see e.g. Arnaud 2010).

X-ray observations have shown that the spatial variation of the ICM density follows the so-called Beta profile where the electron number density $n_e(r)$ at radius r (Cavaliere & Fusco-Femiano 1976) from the cluster center is given by

$$n_e(r) = n_0 \left(1 + (r/r_c)^2 \right)^{-3\beta/2}, \quad (1.14)$$

where n_0 is the central number density, r_c is the core radius and β is a parameter which can take values between 0.5 and 1. Using this model, the projected X-ray surface brightness at projected angular distance θ from the center is given by

$$S_X(\theta) = S_{X,0} \left(1 + (\theta/\theta_c)^2 \right)^{\frac{1}{2} - \frac{3}{2}\beta}, \quad (1.15)$$

where, $\theta_c = r_c/D_A$, is the projected angular distance of the core with D_A the angular diameter distance to the cluster. The ICM can also be characterized by an optical depth

which can be defined as

$$\tau = \int n_e \sigma_T dl, \quad (1.16)$$

where σ_T is the Thomson's cross-section and the integration is performed along the line of sight. Subsequently one can use eq. 1.14 to calculate the optical depth (see Colafrancesco et al. 2003) at a projected distance from the center of the cluster and this can be achieved as follows

$$\tau_\theta(\theta) = \tau_0 \left(1 + (\theta/\theta_c)^2 \right)^{\frac{1}{2} - \frac{3}{2}\beta}, \quad (1.17)$$

where τ_0 is given by

$$\tau_0 = \sqrt{\pi} n_{e0} \sigma_T r_c \frac{\Gamma(3\beta/2 - 1/2)}{\Gamma(3\beta/2)}. \quad (1.18)$$

Typical values of average optical depth associated with the thermal gas usually range between 10^{-3} to 10^{-2} .

1.2.2 Cosmic rays and non-thermal emissions

In addition to X-rays and gravitational lensing measurements, galaxy clusters have also been observed at radio frequencies (e.g. Giovannini 2004, Govoni & Feretti 2004, Feretti 2012). Some of the radio signals are attributed to individual radio galaxies within the cluster and the emission region can extend beyond the optical boundaries of the galaxy. These types of signals have been extensively observed in isolated radio galaxies that are not attributed to any cluster. However, a more puzzling fact is that some galaxy clusters show diffuse emission regions that cannot be attributed to any specific galaxy or galaxies (Feretti 2005, Ferrari et al. 2008). Therefore, these emissions are attributed to non-thermal activities within the ICM and this has been observed in around $\approx 10\%$ of all the galaxy clusters known today (Feretti 2012). These facts show that the ICM is much more complex than just an accumulation of hot gas.

Depending on the morphologies and location of these diffuse radio emission regions, galaxy clusters are classified as having radio halos or relics or both (see Fig 1.7). Typically speaking radio halos are usually located around the center whereas relics are usually found on the outskirts. Whether there is a relation between the halos and the relics is still unknown (see Feretti 2012 for a review).

The radio luminosity coming from the ICM is of power law shape, $P_\nu \propto \nu^{-(q-1)}$ where ν is the frequency and q is the power law index (Shimwell et al. 2014). Therefore the plausible mechanism responsible for this emission is the synchrotron mechanism, whereby relativistic electrons are interacting with the large scale magnetic fields. The power law shape of the radio luminosity implies that the electrons also follow a power law distribution with spectral index α ($q = (\alpha - 1)/2$). These magnetic fields could have originated before or after the recombination epoch. The energy of the relativistic electrons is dependent on

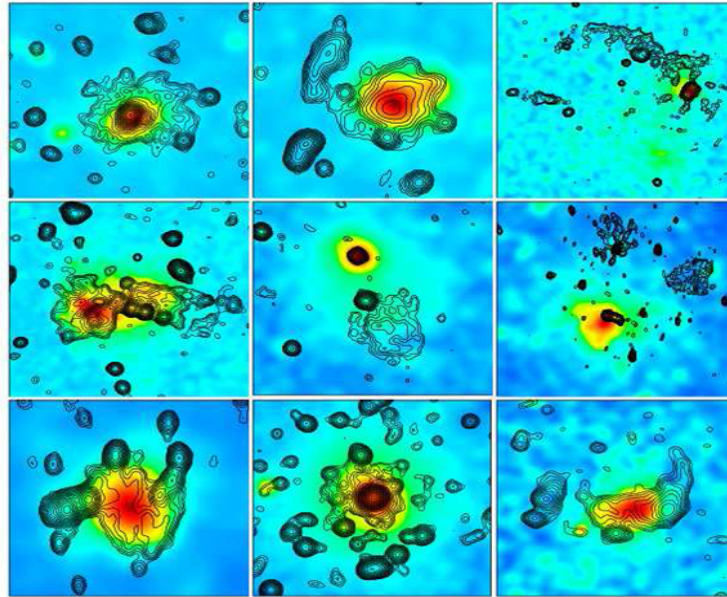


Figure 1.7: Radio emission for several galaxy clusters illustrating the diffuse emission location and morphology (Figure from Feretti 2012).

the strength of the magnetic fields, e.g. higher magnetic fields would imply lower energetic electrons for synchrotron emission observed at a fixed frequency. Magnetic fields of clusters derived from synchrotron emission usually rely on the equipartition distribution of energies among the fields and particles. From this, magnetic fields from around a few μG have been estimated. This would relate to a possible electron lorentz factor γ_e in the range $10^3 - 10^6$. On the other hand, magnetic field values derived from Faraday rotation measurements are higher, ≈ 10 to $50 \mu\text{G}$. Despite all these estimations, cosmic magnetic fields and their origins remain a challenge for cosmologists (see e.g. Govoni & Feretti 2004, Bonafede et al. 2011, Colafrancesco et al. 2011, Feretti 2012).

Finally, non-thermal emissions from clusters have also been attributed to dark matter annihilation. If dark matter is really made up of WIMPS, the decay of these particles will result in standard model particles among which are relativistic electrons and gamma-rays. These can be detected by multifrequency observations (Colafrancesco et al. 2015a, Colafrancesco et al. 2016a, Marchegiani & Colafrancesco 2015, Marchegiani & Colafrancesco 2016).

1.3 The Sunyaev-Zel'dovich effect (SZE)

The Sunyaev-Zel'dovich effect (SZE), as we have mentioned before, is a spectral distortion of the CMB spectrum as a result of photons being inverse Compton (IC) scattered by the electrons found in the atmosphere of cosmic structures (see e.g. Birkinshaw 1999, Ensslin

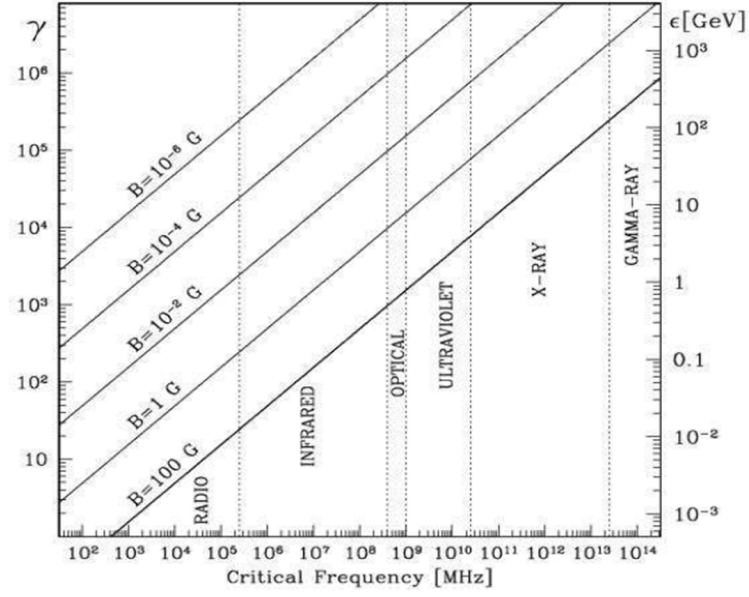


Figure 1.8: The electron Lorentz factor plotted against the observed/critical frequency for different magnetic fields. It is clearly noticed for the radio bands and for magnetic field around the μG , this would roughly correspond to Lorentz factors within 10^3 to 10^6 (Govoni & Feretti 2004).

& Kaiser 2000, Colafrancesco 2003). As a result of this comptonization process, observation of the CMB along the line of sight of a cosmic structure will show a decrease in intensity in the Rayleigh-Jean frequency interval and an increase in the Wien frequency interval. This effect was theorized around the 1970s but at that time, radio/microwave instrumentation was still at its infancy and therefore the SZE could not be observed. Nowadays the SZE has been observed in many clusters of galaxies and the biggest sample up to date comes from the *Planck* instrument (Ade et al. 2011, 2014b, 2016c), whereby many clusters have been able to be identified using SZE observations. The SZE is usually expected within 1 GHz up to 1000 GHz and is becoming very relevant due to current and upcoming instruments such as the SKA, CORE++, *Millimetron* and ALMA.

CMB photons can also be comptonized by electrons during the primordial time (Zel'dovich & Sunyaev 1969) and this will also result in a distortion in the spectrum of the CMB. However, this source of scattering can easily be differentiated from the SZE, as the latter is localized, meaning the distortion is seen towards a cluster which is visible in the optical and X-ray bands. Therefore, the SZE signals will not be confused with comptonization emissions of the early Universe (Birkinshaw 1999).

1.3.1 The SZE spectrum

The SZE is a photon-electron interaction whereby the frequency of the photon is altered due to the motion of the electron. Since the CMB consists mostly of low energy photons, quantum effects and energy transfers can be neglected, and therefore the scattering process in the rest frame of the electron can be described in the Thomson limit, $m_e c^2 \gg \gamma_e h\nu$, where h is the Planck constant, γ_e and m_e are the respective Lorentz factor and mass of the electron (Birkinshaw 1999, Ensslin & Kaiser 2000). Within this limit, the spectrum of the SZE is usually computed for thin plasmas (low optical depth) by solving the Kompaneets equation (Kompaneets 1956) for a thermal electron distribution and is valid only when the speed of the electron is non-relativistic, hence this method is also termed the non-relativistic approach.

The SZE can be described as a change in intensity, $\Delta I(x)$, which upon solving the Kompaneets equation yields the expression as follows

$$\Delta I(x) = 2 \frac{(k_B T_0)^3}{(hc)^2} y_{\text{th}} g(x), \quad (1.19)$$

where $x = h\nu/k_B T_0$ is the a-dimensional frequency, k_B is the Boltzmann constant. The quantity y is the Compton parameter for a thermal electron distribution and is given by

$$y = \tau \frac{k_B T_e}{m_e c^2} \quad (1.20)$$

where m_e is the mass of the electron and T_e is the electron temperature. The spectral function $g(x)$ is given by

$$g(x) = \frac{x^4 e^x}{e^x - 1} \left[x \frac{e^x + 1}{e^x - 1} - 4 \right], \quad (1.21)$$

in the non-relativistic limit. The Kompaneets approximation is valid as long as y remains small, which means that it is only appropriate for cosmic structures of low temperatures and low optical depths. Note that the spectral function $g(x)$ is independent of the cluster temperature, which means that the spectral shape of the SZE in the Kompaneets limit is insensitive to the plasma temperature.

Although the Kompaneets solution is useful, it is very limited. The first limitation is the reliance on the non-relativistic limit, which makes it adequate only for low temperature cosmic structures, up to $T_e \approx 2$ keV. As a matter of fact, it has been observed that galaxy clusters can have temperatures around 10 keV or even higher (see e.g. Reichert et al. 2011, Wik et al. 2014). This will make this approximation inadequate to compute the SZE spectrum for hot clusters. Secondly, the Kompaneets equation is only valid for a thermal electron distribution and therefore cannot be applied to a general electron distribution. The atmospheres of galaxy clusters do contain non-thermal electrons (relativistic or power law distribution of electrons) which will also scatter the CMB photons and therefore will produce a non-thermal SZE effect (Birkinshaw 1999, Ensslin & Kaiser 2000, Colafrancesco

et al. 2003). Therefore it is important to address this issue and compute the SZE in a full relativistic approach which is valid for any general electron distribution. Furthermore, the non-thermal emission regions can co-spatially exist with the X-ray emitting regions (Colafrancesco & Marchegiani 2008), hence the Comptonization process would involve two electron distributions simultaneously (Colafrancesco et al. 2003, 2011). Also, it is possible to have two thermal electron distributions of different temperatures and optical depths co-spatially existing together in a given cosmic structure. These situations have been shown in the case of the Bullet cluster, whereby the SZE spectral data is best described using two electron distributions (Colafrancesco et al. 2011, Marchegiani & Colafrancesco 2015). In addition to that, the Kompaneets solution is only valid for thin plasmas ($\tau \ll 1$) and therefore is not valid for thick atmospheres whereby multiple scatterings become substantial.

These above considerations demand a full relativistic approach for computing the SZE, which is valid for any general or combination of electron distributions.

1.3.2 The relativistic SZE spectrum

In order to compute the relativistic SZE spectrum, one has to solve the relativistic Boltzmann equation (Nozawa & Kohyama 2009) in the Thomson limit approximation, $m_e c^2 \gg \gamma_e h\nu$. The change in intensity is then given to first order in optical depth, τ , by

$$\Delta I(x) = \tau \left[\int_{-\infty}^{\infty} ds P_1(s) I_0(xe^{-s}) - I_0(x) \right], \quad (1.22)$$

where $I_0(x)$ is the incident CMB radiation spectrum which is given by

$$I_0(x) = 2 \frac{(k_B T_0)^3}{(hc)^2} \frac{x^3}{e^x - 1}, \quad (1.23)$$

and $P_1(s)$ is the photon redistribution function with $s = \ln \nu'/\nu$, where ν' and ν are the initial and final frequency of the photon after scattering with an electron (see Birkinshaw 1999, Ensslin & Kaiser 2000). This function is computed by convolving the electron distribution function, $f_e(p_e)$, with another function $P(s, p_e)$ which represents the redistribution function for a single electron, where $p_e = \beta_e \gamma_e$ is the normalized momentum. Therefore we write as follows;

$$P_1(s) = \int_{p_{\min}}^{\infty} P(s, p_e) f_e(p_e) dp_e, \quad (1.24)$$

where p_{\min} is the minimum momentum of the electron required to cause a shift s (see e.g. Birkinshaw 1999, Ensslin & Kaiser 2000, Colafrancesco et al. 2003). This p_{\min} depends on the electron distribution. The function $P(s, p_e)$ is given by

$$P(s, p_e) = \frac{3(1 + e^s)e^s}{8p_e^5} \left[\frac{3 + 3p_e^2 + p_e^4}{\sqrt{1 + p_e^2}} - \frac{3 + 2p_e^2}{2p_e} (2 \sinh^{-1} p_e - |s|) \right] + \frac{3|1 - e^s|}{32p_e^6} \left[1 + (10 + 8p_e^2 + 4p_e^4)e^s + e^{2s} \right]. \quad (1.25)$$

Notice that this approach allows the SZE to be computed for any generic electron distribution and therefore can safely be applied to compute the spectrum for thermal or non-thermal electron distributions. It also allow the computation of the SZE spectrum for a combination of electron populations. It is important to stress that $f_e(p_e)$ is always normalized such that $\int f_e(p_e)dp_e = 1$. This relativistic approach is valid for electron lorentz factor $\gamma_e < 10^8$ so that the Thomson approximation is not violated.

For a thermal electron distribution (like those responsible for the X-ray emission in galaxy clusters), a relativistic Maxwellian distribution is used (Birkinshaw 1999, Ensslin & Kaiser 2000, Colafrancesco et al. 2003) and $f_e(p_e)$ is written as

$$f_e(p_e) = \frac{\beta_{\text{th}}}{K_2(\beta_{\text{th}})} p_e^2 e^{-\beta_{\text{th}} \sqrt{1+p_e^2}}, \quad (1.26)$$

where $\beta_{\text{th}} = m_e c^2 / k_B T_e$ and $K_2(\beta_{\text{th}})$ is the modified Bessel function of the second kind. In this case, the minimum momentum p_{min} is given by $p_{\text{min}} = \sinh(|s|/2)$. We show in Fig 1.9 the SZE spectrum using eq.1.22 for this distribution of electron for different values of the electron temperature T_e . We also superimposed the non-relativistic description (solid) and we clearly see that the relativistic approach boils down to the Kompaneets approach in the limit of low temperature. The spectral shape of the SZE, contrary to the one calculated using the Kompaneets equation, is sensitive to the temperature of the electron. This is so, because the spectrum of the SZE is dependent on $f_e(p_e)$ and for thermal electrons, $f_e(p_e)$ depends on temperature. A relativistic analogue to the spectral function $g(x)$ can be defined as $\bar{g}(x) = \Delta I(x)/y$ (see Ensslin & Kaiser 2000, Colafrancesco et al. 2003).

The Kompaneets solution can also be written similar to eq. 1.22 by using the redistribution kernel as follows

$$P_K(s) = \frac{1}{\sqrt{4\pi y}} e^{-\frac{(s+3y)^2}{4y}}. \quad (1.27)$$

Using the above kernel, $P_K(s)$, the solution to the Kompaneets equation can be written similar to eq. 1.22 as follows

$$\Delta I(x) = \left[\int_{-\infty}^{\infty} ds P_K(s) I_0(xe^{-s}) - I_0(x) \right]. \quad (1.28)$$

On the other hand, for non-thermal electrons (like those responsible for non-thermal emission in radio-halos/relics and lobes of radio-galaxies), we usually use a power law electron distribution. This is given by

$$f_e(p_e) = A(p_1, p_2, \alpha) p_e^{-\alpha}, \quad (1.29)$$

and the normalization $A(p_1, p_2, \alpha)$ is given by:

$$A(p_1, p_2, \alpha) = \frac{\alpha - 1}{p_1^{1-\alpha} - p_2^{1-\alpha}}. \quad (1.30)$$

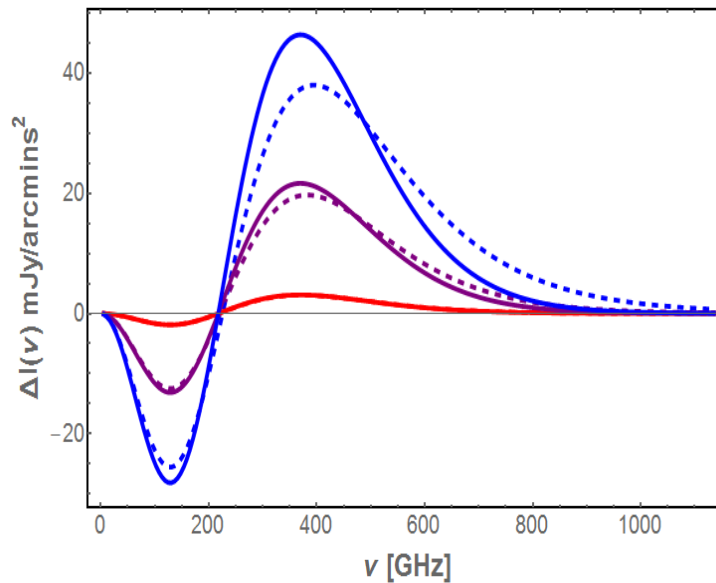


Figure 1.9: The spectral distortion of the SZE computed for a thermal electron distribution of optical depth $\tau = 10^{-3}$ for different temperatures $T_e = 1$ (red), 7 (purple), 15 (blue) keV in the relativistic (dotted) and non-relativistic case (solid).

The maximum momentum p_2 is usually taken as infinity and α is the spectral index. The momentum p_1 is usually treated as a free parameter. This is the simplest electron distribution that is consistent with the spectra of radio-halos and radio-galaxies observed (Ensslin & Kaiser 2000, Feretti 2001, Colafrancesco et al. 2011, Feretti 2012, Colafrancesco et al. 2013, Marchegiani & Colafrancesco 2015). Quantities such as pressure and temperature can be calculated for this type of electron distribution as well (see Ensslin & Kaiser 2000, Colafrancesco et al. 2003). We show the SZE spectrum in the case of a non-thermal electron distribution for different values of p_1 in Fig 1.10. One can clearly see that the spectral feature of the non-thermal SZE is completely different from that of the thermal one.

We clearly see that if relativistic effects are taken into account, the SZE spectrum becomes different from the usual non-relativistic one. In addition to that, non-thermal electrons that are present in cosmic structures will also produce a non-thermal SZE effect in addition to the thermal one.

By following the same approach, the SZE coming simultaneously from two electron distributions that exist within the same region can be calculated. If we assume that the two electron distributions are independent and there is no interaction between them, then one can write in this case the distribution function

$$f_e(p_e) = C_A f_{e,A}(p_e) + C_B f_{e,B}(p_e), \quad (1.31)$$

where $f_{e,A}$ and $f_{e,B}$ are the electron distributions for population A and B respectively. The

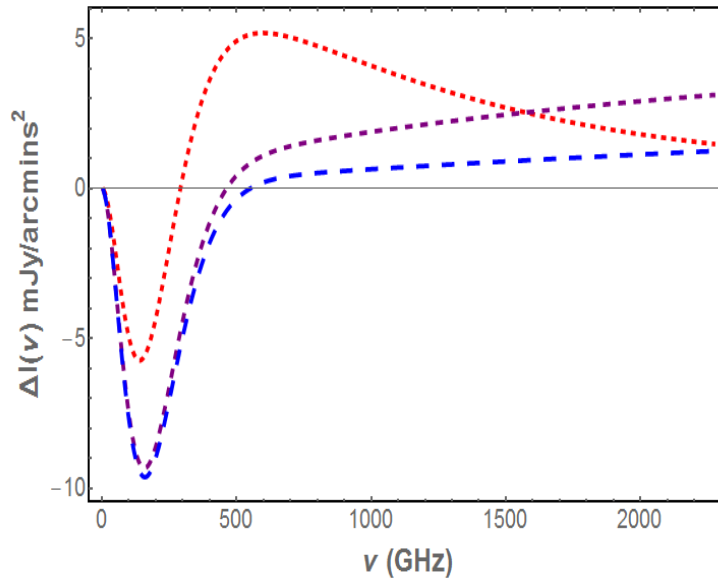


Figure 1.10: The SZE spectrum of a non-thermal plasma of spectral index $\alpha = 2.5$ for $p_1 = 0.5$ (red), 1 (purple), 3 (blue). We use an optical depth $\tau = 10^{-4}$.

values C_A and C_B are related to the optical depths of each electron population. Given that $f_e(p_e)$ is normalized, the constants C_A and C_B are related through $C_A + C_B = 1$. One can write $C_A = \tau_A/\tau$ and $C_B = \tau_B/\tau$, where τ_A and τ_B correspond to the optical depth of each electron population and $\tau = \tau_A + \tau_B$. The scattering kernel $P_1(s)$ is then given by

$$P_1(s) = C_A P_{1,A}(s) + C_B P_{1,B}(s), \quad (1.32)$$

whereby $P_{1,A}(s)$ and $P_{1,B}(s)$ are the redistribution functions corresponding to each electron population. Then inserting $P_1(s)$ into eq 1.22, one can obtain the SZE spectrum resulting from two electron distributions that exist co-spatially within a region (Colafrancesco et al. 2003).

The above approach is valid for thin optical depth whereby a photon is scattered only once, but it can be extended to include the effect of multiple scattering which is more appropriate in describing thick plasmas (see e.g. Colafrancesco et al. 2003). However, the low optical depth approximation is still valid for describing plasmas found in the atmosphere of clusters and radio-galaxies ($\tau \approx 10^{-6}$ to 10^{-2}). Also, multiple scattering will induce SZE distortions of the order of τ^n , which can be neglected given the order of magnitude of the optical depth ($\approx 10^{-6} - 10^{-2}$) of clusters or radio-galaxy atmospheres. It is also worth mentioning here that the approach above does not take into consideration the anisotropy of the CMB and therefore neglect higher order terms that could be present. Higher order multipoles-induced effects, rather than just the monopole, can also be present in SZE intensity (Chluba & Dai 2014) but this will not be the main focus in this present work. This

effect can also be reduced if the SZE observation is done symmetrically around the center of the structure.

1.3.3 Relevance of the SZE

The SZE is a powerful astrophysical probe that can be used to put constraints on various phenomena that happen in the atmosphere of cosmic structures. Strong constraints on the spatial distribution of the thermal gas that are present in galaxy clusters can be obtained by using the SZE together with X-ray measurements (Carlstrom et al. 2002, Arnaud et al. 2010). In addition to that, the SZE can provide information on the non-thermal particles that are found in cluster cavities, radio-halos and relics. Every astrophysical model used to explain these non-thermal activities relies on the existence of non-thermal electrons. The non-thermal SZE would allow one to constrain these models since the SZE spectrum is sensitive to the electron distribution (Colafrancesco 2005, Colafrancesco et al. 2011, Prokhorov et al. 2011, Marchegiani & Colafrancesco 2015). This can also be applied to the lobes of radio-galaxies, whereby these extended structures also host a population of relativistic particles (Colafrancesco et al. 2013).

Furthermore, the spectral distortion associated with the SZE has important cosmological relevance (see e.g. Birkinshaw 1999, Carlstrom et al. 2002, Colafrancesco 2009 for a full review). Cluster identification is one of the first anticipated use of the SZE since it is a measure of the pressure of the ICM along the line sight, allowing us to identify cosmic structures at any location. Among other interesting aspects of the SZE is its redshift independence, which would allow high redshift clusters to be detected, e.g. the cluster CL0016+16 which has a redshift of $z \approx 0.5$ was observed via SZE (Birkinshaw 1999). This means that the SZE is ideal as a tracer of cosmic structures up to high redshift, allowing the study of the evolution of large scale structures across cosmic time. Since the evolution of cluster density is highly dependent on the underlying cosmological model, the equation of dark energy can be determined (Weller et al. 2002). Additionally, coupled with X-ray observations, the SZE can be used to measure cluster distances (Cavaliere et al. 1977, Birkinshaw 1979, Silk & White 1978) which would allow the Hubble constant to be determined. In a similar fashion, SZE together with X-ray measurements can also be used to put constraints on the gas mass fraction in clusters and hence estimate Ω_M at cluster locations (Arnaud et al. 2010). Since galaxy clusters are large scale structures, the value of Ω_M derived from these measurements would be expected to reflect its universal value. Another cosmological use of the SZE is in revealing the nature of dark matter. If dark matter particles are made up of WIMPS, then relativistic electrons will be produced as a product of annihilation. These electrons will produce an SZE and with very sensitive measurements, the spectrum can be identified (Colafrancesco 2004).

1.4 Polarization of the SZE

Polarization is a natural outcome of IC scattering and therefore the SZE is expected to have a polarized component in addition to an intensity spectral distortion (Sazonov & Sunayev 1999, Challinor et al. 2000, Lavaux et al. 2004, Portsmouth & Bertschinger 2004a, 2004b, Emritte et al. 2016). The intrinsic multipoles of the CMB, which originate from the small temperature variations created from spatial fluctuations of energy densities, bulk velocities and gravitational potentials at the surface of last scattering, are mainly responsible for the induced polarization in the SZE (Sazonov & Sunayev 1999). The CMB then appears anisotropic and upon IC scattering by the electrons that are present in cosmic structures, result in polarization. Without taking into consideration relativistic corrections, attempts in calculating the polarization associated with the SZE have shown that the polarization is proportional to the quadrupole of the CMB at the cluster location and is of the order of $\tau a_{2,2}$, where $a_{2,2}$ is the quadrupole of the CMB (Sazonov & Sunayev 1999, Lavaux et al. 2004).

1.4.1 Non-relativistic SZE polarization

Preliminary calculations of the SZE polarization relied on the assumption that the electrons involved in the scattering process are not moving at relativistic speeds ($\beta_e = v_e/c \ll 1$). Assuming the Thomson approximation and that the incident radiation is not polarized but anisotropic, the outgoing radiation will have a degree of linear polarization proportional to the CMB quadrupole moment in the angular distribution of the incident radiation. If the frame of reference is chosen such that the z-axis coincides with the line of sight of the scattered radiation at first scattering, the Stokes parameters Q and U can be written follows (Chandrasekhar 1960):

$$\frac{\partial Q}{\partial \tau}(x) = \frac{3}{16\pi} \int \sin^2(\theta) \cos(2\phi) I(x, \theta, \phi) d\Omega \quad (1.33)$$

$$\frac{\partial U}{\partial \tau}(x) = \frac{3}{16\pi} \int \sin^2(\theta) \sin(2\phi) I(x, \theta, \phi) d\Omega . \quad (1.34)$$

The angle θ is the polar angle measured with respect to the z-axis whereas ϕ is the azimuth angle. The intrinsic temperature anisotropy of the CMB can be described using a unit vector $\hat{n}(\theta, \phi)$. Hence, the intensity $I(x, \theta, \phi)$, in a given direction written using spherical harmonic expansion is given as follows

$$I(x, \theta, \phi) = 2 \frac{(k_B T_0)^3}{(hc)^2} \frac{x^3}{\exp\left[\frac{h\nu}{kT(\theta, \phi)}\right] - 1} = \sum_{l,m} I_{l,m}(x) Y_{l,m}(\theta, \phi) , \quad (1.35)$$

where $T(\hat{n})$ is given by

$$T(\theta, \phi) = T_0 [1 + \delta(\theta, \phi)] \quad (1.36)$$

and

$$\delta(\theta, \phi) = \sum_{l,m}^{\infty} a_{l,m} Y_{l,m}(\theta, \phi). \quad (1.37)$$

By inserting eq. 1.37 into eq. 1.36 and then substituting into eq. 1.35, the intensity of the incident radiation can be written as an expansion in terms of spherical harmonics, given that the variations in the temperature of the CMB are generally small:

$$I(x, \theta, \phi) = \frac{2(k_B T_0)^3}{(hc)^2} \left[\frac{x^3}{e^x - 1} + \frac{e^x x^4}{(e^x - 1)^2} \sum_{l,m}^{\infty} a_{l,m} Y_{l,m}(\theta, \phi) \right] + O(\delta^2) = \sum_{l,m}^{\infty} I_{l,m}(x) Y_{l,m}(\theta, \phi). \quad (1.38)$$

After inserting this into eq. 1.33 and eq. 1.34 and integrating over the solid angle, we are left with only two terms, namely $l = 2, m = \pm 2$. The solution can be written as

$$\frac{\partial Q}{\partial \tau}(x) = \sqrt{\frac{3}{10\pi}} \frac{I_{2,2} + I_{2,-2}}{4} = \frac{1}{2} \sqrt{\frac{3}{10\pi}} \text{Re}[I_{2,2}(x)], \quad (1.39)$$

and

$$\frac{\partial U}{\partial \tau}(x) = \sqrt{\frac{3}{10\pi}} \frac{I_{2,-2} + I_{2,2}}{4i} = -\frac{1}{2} \sqrt{\frac{3}{10\pi}} \text{Im}[I_{2,2}(x)]. \quad (1.40)$$

The multipoles of the intensity can be obtained directly from eq. 1.38 and the relevant ones up to the octupole are

$$\begin{aligned} I_{0,0}(x) &= \sqrt{4\pi} 2 \frac{(k_B T_0)^3}{(hc)^2} \frac{x^3}{e^x - 1} = \sqrt{4\pi} 2 \frac{(k T_0)^3}{(hc)^2} F_0(x) \\ I_{2,2}(x) &= a_{2,2} 2 \frac{(k_B T_0)^3}{(hc)^2} \frac{e^x x^4}{(e^x - 1)^2} = a_{2,2} 2 \frac{(k T_0)^3}{(hc)^2} F_1(x) \\ I_{3,2}(x) &= a_{3,2} 2 \frac{(k_B T_0)^3}{(hc)^2} \frac{e^x x^4}{(e^x - 1)^2} = a_{3,2} 2 \frac{(k T_0)^3}{(hc)^2} F_1(x), \end{aligned} \quad (1.41)$$

where we have defined the functions $F_0(x) = x^3/(e^x - 1)$ and $F_1(x) = (e^x x^4)/(e^x - 1)^2$. We have also used here the fact that $I_{l,m}^* = (-1)^m I_{l,-m}$. Then we obtain the Stokes parameters Q and U as follows:

$$\frac{\partial Q}{\partial \tau}(x) = \frac{1}{2} \sqrt{\frac{3}{10\pi}} 2 \frac{(k_B T_0)^3}{(hc)^2} \text{Re}[a_{2,2}] F_1(x), \quad (1.42)$$

and

$$\frac{\partial U}{\partial \tau}(x) = -\frac{1}{2} \sqrt{\frac{3}{10\pi}} 2 \frac{(k_B T_0)^3}{(hc)^2} \text{Im}[a_{2,2}] F_1(x). \quad (1.43)$$

The Stokes parameters can be obtained in terms of the optical depth of the electron distribution in the single scattering approximation by just multiplying by τ as follows

$$Q(x) = \frac{\tau}{2} \sqrt{\frac{3}{10\pi}} 2 \frac{(k_B T_0)^3}{(hc)^2} \text{Re}[a_{2,2}] F_1(x), \quad (1.44)$$

and

$$U(x) = -\frac{\tau}{2} \sqrt{\frac{3}{10\pi}} 2 \frac{(k_B T_0)^3}{(hc)^2} \text{Im}[a_{2,2}] F_1(x). \quad (1.45)$$

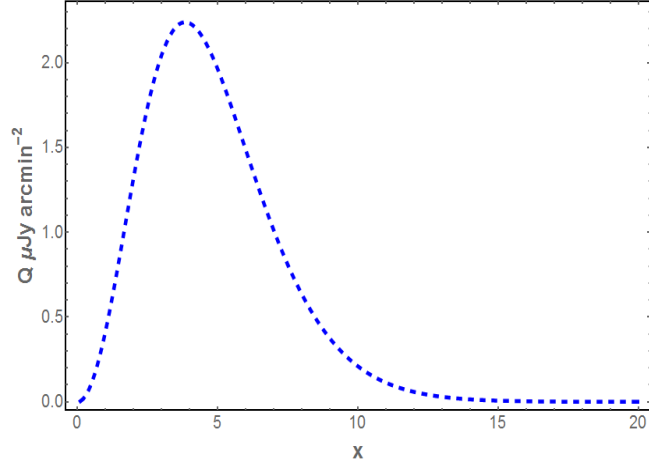


Figure 1.11: The Stokes parameter Q computed in the non-relativistic approach for a value $|a_{2,2}| = 1.3 \times 10^{-5}$ and $\tau = 0.01$.

The basis used to describe the Stokes parameters can always be rotated in such a way that $Re[a_{2,2}] = |a_{2,2}|$ and $Re[a_{3,2}] = |a_{3,2}|$. Hence we speak only of Q as U will be zero using such a basis (we will keep using this basis in chapter 4). The values of $|a_{l,m}|$ are related to the coefficients C_l of the angular power spectrum of the CMB temperature anisotropy (Ade et al., 2014a, 2016b, 2016d) as follows

$$C_l = \frac{1}{2l+1} \sum_{m=-l}^l \langle |a_{l,m}|^2 \rangle. \quad (1.46)$$

Assuming that $|a_{l,-2}|^2 \approx |a_{l,-1}|^2 \approx |a_{l,0}|^2 \approx |a_{l,1}|^2 \approx |a_{l,2}|^2$, the values of $|a_{2,2}|$ and $|a_{3,2}|$ are then obtained as

$$|a_{2,2}| \approx \sqrt{C_2} \quad (1.47)$$

$$|a_{3,2}| \approx \sqrt{C_3}. \quad (1.48)$$

We obtained values of $|a_{2,2}| = 1.3 \times 10^{-5}$ and $|a_{3,2}| = 8.7 \times 10^{-6}$. We show in Fig. 1.11 the spectrum of the Stokes parameter Q for the CMB quadrupole computed using eq. 1.44. We finally define the degree of polarization as

$$\Pi = \sqrt{Q^2 + U^2}/I. \quad (1.49)$$

It can be clearly seen that in this non-relativistic approach, the Stokes parameters are directly proportional to the quadrupole of the CMB at the location of the electron, which makes the SZE polarization of great use for cosmological application.

1.4.2 Relevance of the SZE polarization

Cosmological applications of the SZE polarization induced by the anisotropy of the CMB have been envisaged. Cosmic variance poses a serious issue for the measurement of the CMB quadrupole from only our location. On the other hand, the SZE polarization allows the quadrupole at a cosmic structure location to be measured and if this is carried out for several cosmic structures, the cosmic variance can be reduced (Kamionkowski & Loeb 1997, Portsmouth 2004, Yasini & Pierpaoli 2016). Additionally, this will also allow the reconstruction of local CMB temperature anisotropies (Liu et al. 2016). Measuring the quadrupole at a cosmic structure location is meaningful as it will reveal the level of anisotropy in the CMB seen by the structure at that particular location. Eventually, this will allow the homogeneity assumption of the Universe to be tested observationally (Maartens 2011). Since we can only measure down the past light cone and not on spatial surfaces intersecting that light cone, homogeneity cannot be measured or tested directly. However, one can link it to isotropy by using the Copernican principle (CP), i.e. there is no special position in the Universe, and test whether the principle still holds at other locations in the cosmos. Furthermore, SZE polarization data for a large sample of clusters spanning over a wide redshift interval would provide statistical inference of the integrated Sachs-Wolfe (ISW) effect (Sachs & Wolfe 1967) and the latter's contribution to the r.m.s quadrupole can be determined. The ISW effect is strongly dependent on the background cosmology, therefore, SZE polarization can be used as a probe of dark energy (Berera & Gordon 2001).

Furthermore, in addition to the quadrupole, it has been demonstrated that under certain circumstances, higher order multipoles of the CMB can also contribute to the SZE polarization (Challinor et al. 2000, Yasini & Pierpaoli 2016). This means that the other multipoles of the CMB at the cluster location are also accessible through the SZE polarization. As a matter of fact, it has been demonstrated that for region to follow a FLRW geometry, the vanishing of the CMB dipole, quadrupole and octupole is a sufficient condition (Ellis et al. 1983, Maartens 2011).

For a rich galaxy cluster with optical depth, $\tau \approx 0.02$, the polarization signal is expected to be $\simeq 0.1\mu\text{K}$ in the Rayleigh-Jeans frequencies and lies below the detection limit of current observational instruments (Sazonov & Sunyaev 1999, Lavaux et al. 2004, Yasini & Pierpaoli 2016). However, an r.m.s value of the quadrupole can still be retrieved if the signal is searched in large number of cosmic structures.

In addition to the polarization induced from the anisotropy of the CMB, SZE polarization can also be produced as a result of the other physical mechanisms (Sazonov & Sunyaev 1999, Lavaux et al. 2004, Yasini & Pierpaoli 2016). The transverse velocity component of a cosmic structure will produce a kinetic SZE polarization which is of the order of $(V_c/c)^2\tau$, where V_c is the peculiar velocity of the cosmic structure with respect to the CMB (Sazonov & Sunyaev

1999, Lavaux et al. 2004, Yasini & Pierpaoli 2016). Another source of polarization is that of multiple scatterings of the CMB within the cluster and is of the order of τ^2 (Sazonov & Sunyaev 1999, Lavaux et al. 2004). These secondary effects will be neglected in this present work, but will be discussed wherever necessary.

1.5 Objectives of this Thesis

In the next three chapters, we will look at some new cosmological applications of the SZE. In fact, we will demonstrate that the SZE can be used as a probe of cosmological radio backgrounds, allowing new information to be derived regarding the cosmos.

Chapter 2 presents the use of the SZE, computed in a fully relativistic manner, as a probe for the epoch of reionization. This is possible because any distortion produced in the CMB during this primordial epoch will be reflected in the SZE spectrum as well. We compute the SZE-21cm (SZE associated with 21-cm background) and analyse the spectrum for four different background models. We discuss the advantage of the SZE-21cm over traditional ways of observing the 21-cm background. In addition to that, we also look at the possibility of its measurement with the SKA telescope.

Secondly, in chapter 3, we look at the possibility of a Non-Planckian (NP) effect induced in the CMB spectrum due to a non-zero value of the plasma frequency around the recombination epoch. By an extensive analysis of the current available CMB data, we investigate this possibility by placing upper limits on the value of the plasma frequency allowed by the set of data. Furthermore, we investigate the impact of a non-zero plasma frequency on two other observables; the SZE effect and the cosmological 21-cm background.

In Chapter 4, we look at the SZE polarization computed in the full relativistic regime and compute the Stokes parameters in a way that can incorporate any generic electron distribution and also combination of electron populations. We show the polarization spectrum for thermal and non-thermal electron populations and we provide an extensive discussion on their spectra. Then, we apply our techniques to the Bullet cluster for which the SZE measurements are available and investigate the possibility of its detection over a wide range of frequencies with currently and upcoming instruments such as the SKA, CORE++, ALMA and *Millimetron*. We also discuss sources of contaminations such as velocity effects, multiple scattering and the E-mode polarization of the CMB.

Finally in Chapter 5, we will summarize and discuss our results together with some suggestions regarding future works.

Chapter 2

The EoR and the SZE-21cm

At redshift $z = 1100$ (the Recombination Epoch), the temperature of the Universe was low enough for protons and electrons to combine to form hydrogen and the ionization fraction of the Universe decreased significantly. By the end of recombination, the baryonic matter content of the Universe was mainly in the form of hydrogen atoms and some helium. The Universe proceeded towards the dark ages (DA) ($z \approx 1400$ to 20), which is a time period before the formation of any early cosmic structures such as stars and galaxies (Peebles1993). The transition from a homogeneous Universe towards one composed of collapsed structures occurred during this period of time. Following the DA marks the epoch of reionization (EoR), during which the intergalactic medium became ionized again. This happened through the gravitational collapse of the hydrogen gas, hence forming the earliest stars, and through this process the release of electromagnetic radiation ionized the intergalactic medium. Studying the DA and EoR is vital for the understanding of the evolution of the Universe (see, e.g., Barkana & Loeb 2001, Loeb & Barkana 2001, Bromm & Larson 2004, Ciardi & Ferrara 2005, Choudhury & Ferrara 2006, Furlanetto et al. 2006, Morales & Wyithe 2010).

2.1 The Cosmological 21-cm background

The theoretical picture of how the Universe evolved through the DA down to the EoR is well established within the Λ CDM model but is not well tested observationally (Zaroubi 2013). There are actually two observational strategies to constrain these epochs. The first one is to search for individual galaxies around redshift $z \approx 10$ and higher. This would require very sensitive multifrequency observations and efforts are underway to achieve this, with telescopes working in different frequency ranges such as GMT, TMT, E-ELT, JWST and ALMA (see Pritchard & Loeb 2012). Although these instruments will be able to observe an individual galaxy at $z > 10$, only the brightest ones will be seen.

The second strategy is to focus on the signals coming from the neutral hydrogen atoms

that are ubiquitous in the Universe, accounting for $\approx 75\%$ of all atomic species in the intergalactic medium (see e.g., Loeb & Zaldarriaga 2004, Cooray 2004; Bharadwaj & Ali 2004; Carilli et al. 2004, Furlanetto & Briggs 2004, Furlanetto et al. 2006, Pritchard & Loeb 2010, Pritchard & Loeb 2012, Liu et al. 2013). These signals are emitted at wavelength 21 cm (1420 MHz) due to the hyperfine splitting of energy levels ($\Delta E = 5.9 \times 10^{-6}$ eV) in hydrogen atoms through the interaction of magnetic moments between the proton and the electron and is redshift dependent (the observed frequency, $\nu = 1420/(1+z)$ MHz). The background created by these emissions, is called the cosmological 21-cm background and its measurement would act as a tracer of hydrogen atoms at different redshifts, giving us a direct clue on the possible physical processes during the DA and the EoR.

2.2 Physics of the 21-cm radiation

For redshift $z \gtrsim 6$, a primary source of background for measurement of the cosmological 21-cm is the CMB. The brightness temperature of an object is related to its spectral emission $I(\nu)$ as follows (Rybicki & Lightman 1979),

$$T(\nu) = I(\nu) \frac{c^2}{2k_B \nu^2}. \quad (2.1)$$

For the CMB, $T(\nu)$ is constant in the Rayleigh-Jeans frequency band.

The 21-cm emission will appear as a spectral distortion to the CMB background and the contrast is denoted $\delta T(\nu)$. The observed differential brightness, $\delta T(\nu)$, can be calculated against the CMB background as follows

$$\delta T(\nu) = 9x_{\text{HI}}(1+\delta)(1+z)^{1/2} \left(\frac{T_{\text{S}} - T_{\text{CMB}}(z)}{T_{\text{S}}} \right) \text{ mK} \quad (2.2)$$

where x_{HI} is the ionization fraction of hydrogen, δ is the local overdensity, $T_{\text{CMB}}(z)$ is the CMB temperature and T_{S} is the spin temperature, both at redshift z (Furlanetto et al. 2006). The variation of the CMB temperature with redshift is given by $T_{\text{CMB}}(z) = T_0(1+z)$ K, where T_0 is the CMB temperature at $z = 0$, while the spin temperature T_{S} will depend on three physical processes. These processes are: 1) the absorption/emission of 21-cm photon from/to the CMB background; 2) collision with hydrogen atoms and electrons; and 3) the scattering of Ly- α photons (see Barkana & Loeb 2005b, Furlanetto 2006), which are photons emitted by the first galaxies. A Ly-alpha photon is emitted when the electron of hydrogen transit from the $n = 2$ orbital to the $n = 1$ orbital (where n is the principal quantum number). Therefore the cosmological 21-cm signal relies on the behaviour of the spin temperature T_{S} during the evolution of the Universe (Furlanetto 2006, Pritchard & loeb 2012). The predicted 21-cm radiation from the DA down to the EoR is shown in Fig 2.1.

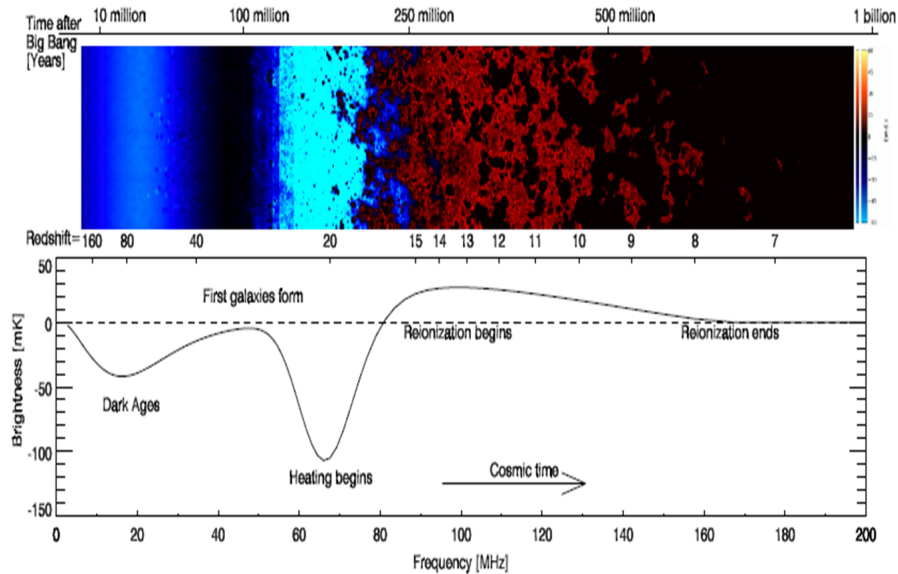


Figure 2.1: The cosmological 21-cm brightness signal emitted by hydrogen starting from the DA ($z \approx 200$) down to the reionization ($z \approx 6$) (Furlanetto 2006, Pritchard & Loeb 2012).

2.3 Measurement of the 21-cm background

Using the CMB as background, the 21-cm emission of hydrogen gas will appear as a faint diffuse background across the whole sky and can be studied similar to the way CMB anisotropies are studied. However there are still some observational challenges that will be faced by future observations of these signals. Firstly, the 21-cm radiation is faint, of the order of tens of mK (Pritchard & Loeb 2012) and until now, only upper-limits have been obtained (see e.g., Paciga et al. 2013, Dillon et al. 2014, Parsons et al. 2014). Secondly, in the relevant frequency range, $30 < \nu < 200$ MHz, where the 21-cm is expected is vulnerable to galactic and extragalactic foregrounds together with various experimental systematics and biases (see e.g., de Oliveira-Costa et al. 2008). Therefore knowledge of the foregrounds and precise calibrations would be crucial in separating the relevant signals from the irrelevant ones.

Several methods have been envisaged to overcome these limitations. One method is to extract the mean 21-cm signal through redshift-anisotropies by studying its fluctuations (Barkana & Loeb 2005a). This is possible with the next generation of instruments such as SKA (McQuinn et al. 2006). A second method is to use the contrast between the bubbles of ionized plasmas (ionized regions) present during the EoR and the 21-cm signal to measure the mean amount of neutral gas (see Furlanetto et al. 2006, Datta et al. 2007).

In this work, we look at an alternative way of measuring the 21-cm emission, by using the SZE produced in large scale cosmic structures. Since the 21-cm emission appears as a distortion to the CMB and in addition to the fact that the SZE is an interaction in which

the CMB photons are involved, the 21-cm will eventually be present in the SZE spectrum as well. Consequently, this means that one can use cosmic structures in our local Universe to probe the DA and the EoR, a method which we denote the SZE-21cm.

2.4 The SZE of the 21-cm

A preliminary result of the SZE-21 cm has been produced in a previous work (Cooray 2006). However, it is noticed that many cosmological and astrophysical aspects have not been accounted for in the calculation and if one wants to use the SZE-21 cm as a probe, it is important to address these aspects and refine the calculation. The aspects which the previous work did not address are:

i) the cosmological 21-cm background model used to describe the DA and the EoR was unphysical due to the presence of many artificial discontinuities, e.g. $\nu \approx 70$, the spectral feature of the model is not well resolved, with a lot of numerical discontinuities (Cooray 2006). The description of the EoR through this model is unphysical, producing substantial 21-cm emission down to redshift $z \approx 2$ ($\nu \approx 300$ MHz);

ii) Only one model of the 21-cm background is used in the calculation of the SZE-21cm. The spectral feature of the 21-cm background can be altered by certain physical processes that could occur during the DA and EoR and one of these physical processes is heating through dark matter annihilation. This has a cosmological implication since the energy release via the annihilation process would be absorbed by the intergalactic medium, hence will have an implication on the thermal and ionization history of the Universe.

iii) The SZE-21cm spectrum was calculated in the non-relativistic limit, which makes the result applicable only to low temperature plasmas. Since many high temperature galaxy clusters have been observed, non-relativistic approximations are inappropriate. In addition to that, they considered only thermal electrons when actually non-thermal electrons are also present in galaxy clusters (e.g. radio halos) and in lobes of radio galaxies. Therefore, it is important to use a full relativistic formalism which can also incorporate electron distributions other than just thermal electron distributions in calculating the SZE-21cm.

iv) Although the SZE-21cm was calculated, but there is no comparison of the signal with the sensitivities of relevant telescopes such as the SKA.

In this work we address these missing aspects by first, using a set of models that contain physical effects that are realistic and also include additional mechanisms such as heating from dark matter annihilation (Valdes et al. 2013, Evoli et al. 2014). Secondly, we perform the calculation of the SZE-21cm using a full relativistic approach which is also valid for any distribution of electrons. Furthermore, we also compare our results with the sensitivity of the SKA instrument.

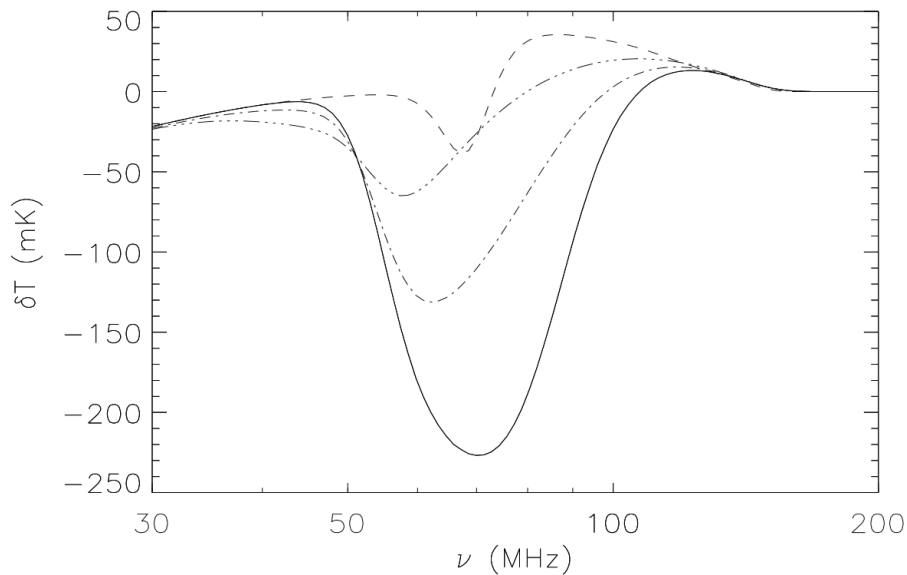


Figure 2.2: The frequency dependence of the cosmological 21-cm brightness signal relative to the CMB, δT , calculated using the 21cmFAST code for four models: a fiducial model without dark matter (solid line, benchmark model), an extreme model without dark matter (dashed line) and two fiducial models with dark matter with $M_{\min} = 10^{-3}M_{\odot}$ (dot-dashed line) and $M_{\min} = 10^{-6}M_{\odot}$ (three dot-dashed line), where M_{\min} is the mass of the smallest DM halo (Colafrancesco et al. 2016b, Evoli priv.comm).

2.5 The 21-cm background models

In order to compute the SZE-21cm spectrum, we consider four different models to represent the physical processes occurring during the EoR to describe the 21-cm background and whose spectral brightness temperature change, $\delta T(\nu)$, has been calculated using the 21cmFAST code (Mesinger et al. 2011). In Fig 2.2, we show the four different models that we consider here for the calculation of the SZE-21cm.

The first model (solid line) is a fiducial model without dark matter in which standard assumptions on the properties of the heating by cosmic structures are used. However, this model neglects collisional effect of the gas that can be observed at $\nu < 30$ and cannot be observed with a ground based telescope such as SKA. The Ly- α radiation field presented at redshift $z \approx 30 - 20$ together with the effects of UV ionization and heating due to X-ray photons at redshifts $z \approx 20 - 6$ (Chen & Miralda-Escude 2004) are taken into account in this model. This first model will be referred to as the benchmark model to discuss certain relevant features of the SZE-21cm.

The second model that we consider, is also one where dark matter is neglected but extreme values for the heating caused by cosmic structures are assumed. In this case, the

coupling between the spin temperature of the intergalactic medium and the Ly- α photons is damped resulting in a deep brightness decrease in the frequency interval, $\nu \approx 50\text{-}70$ MHz, and an eventual increase at higher frequencies ($\nu > 70$ MHz).

Lastly, we consider two models which, in addition to standard physical processes, also involve dark matter annihilation as a source of heating. Dark matter halos with small mass produce the strongest effects, and therefore we consider two minimum halo masses of $10^{-3} M_\odot$ and $10^{-6} M_\odot$. Regarding the nature of dark matter here, we assume a WIMP with mass 10 GeV with annihilation channel e^+/e^- and cross-section $\langle \sigma V \rangle = 10^{-26} \text{ cm}^3/\text{s}$.

2.6 Derivation of the SZE-21cm

The SZE-21cm can easily be computed given that the SZE is an interaction between the photons of the CMB and that of the electrons of cosmic structures. Therefore any energy-injecting process that occurs during the EoR or the DA, will modify the CMB spectrum and subsequently will also modify the SZE. Therefore we denote the modified CMB radiation by $I_{0,\text{mod}}(\nu)$ which can be written as

$$I_{0,\text{mod}}(\nu) = I_0(\nu) + \delta I(\nu) \quad (2.3)$$

where $\delta I(\nu)$ is the perturbation of the CMB radiation due to processes that occur during the EoR and the DA. This is related to $\delta T(\nu)$ by $\delta T(\nu) = \delta I(\nu)c^2/2k_B\nu^2$.

The SZE-21cm at first order in τ , denoted as $\Delta I_{\text{mod}}(\nu)$, can be written using eq 1.22 as follows

$$\Delta I_{\text{mod}}(\nu) = \tau \left[\int ds P_1(s) I_{0,\text{mod}}(\nu e^{-s}) - I_{0,\text{mod}}(\nu) \right]. \quad (2.4)$$

This equation can then be transformed into temperature brightness, ΔT_{mod} , by the relation, $\Delta T_{\text{mod}}(\nu) = \Delta I_{\text{mod}}(\nu)c^2/2k_B\nu^2$. Hence eq 2.4 can be written in terms of brightness temperature as follows,

$$\Delta T_{\text{mod}}(\nu) = \tau \left[\int ds P_1(s) e^{-2s} T_{0,\text{mod}}(\nu e^{-s}) - T_{0,\text{mod}}(\nu) \right]. \quad (2.5)$$

We denote in this particular chapter the standard SZE as $\Delta I_{\text{st}}(\nu)$ or $\Delta T_{\text{st}}(\nu)$ in order to avoid confusion. Using the relation $T_{0,\text{mod}}(\nu) = T_0 + \delta T(\nu)$, one can express eq.2.5 in terms of T_0 and $\delta T(\nu)$ as follows

$$\Delta T_{\text{mod}}(\nu) = \tau T_0 \left[\int ds P_1(s) e^{-2s} - 1 \right] + \tau \left[\int ds P_1(s) e^{-2s} \delta T(\nu e^{-s}) - \delta T(\nu) \right]. \quad (2.6)$$

Although eq 2.4 and eq 2.6 are essentially the same, however, the second one is more interesting for a couple of reasons. Firstly it is already in the units of brightness temperature and more importantly, it shows that the SZE-21cm is a standard SZE ($\Delta T_{\text{st}}(\nu) = \tau T_0 [\int ds P_1(s) e^{-2s} - 1]$) plus an additional component, $\tau [\int ds P_1(s) e^{-2s} \delta T(\nu e^{-s}) - \delta T(\nu)]$, corresponding to the modified portion of the CMB.

2.6.1 The SZE-21 cm spectrum

We show in Fig 2.3 the SZE-21cm calculated for a galaxy cluster with intracluster temperature of 7 keV and optical depth 5×10^{-3} using the benchmark model (solid line in Fig 2.2). Displayed also on the same figure is the standard SZE for the same cluster parameters. It is clearly seen from the plot, that in the absence of $\delta T(\nu)$ in the input spectrum, then the SZE-21cm is essentially the standard SZE.

A spectral feature associated with the SZE-21cm is that in some frequency intervals, it is stronger or weaker than the standard SZE. It is noticed that the curvature of the input spectrum $\delta T(\nu)$ plays a determining factor to this behaviour. In the frequency intervals, $\nu < 55$ MHz and $90 < \nu < 140$ MHz, the input spectrum has a negative curvature and the SZE-21cm is less than the standard one ($\Delta T_{\text{mod}} < \Delta T_{\text{st}}$). On the other hand, in the frequency intervals where the curvature of the input spectrum is positive, $55 < \nu < 90$ MHz and $\nu > 140$ MHz, the SZE-21 cm is greater than the standard one ($\Delta T_{\text{mod}} > \Delta T_{\text{st}}$). An explanation of this spectral feature associated with the SZE-21cm is that IC scattering produces a frequency shift of the photons involved, which consequently makes the amplitude of the SZE at a certain frequency depends on the distribution of photons at that frequency (e.g. the redistribution function $P_1(s)$). At the frequency where the curvature of the input spectrum is negative, a smaller number of photons are present around that frequency with respect to the case of the standard CMB spectrum (where the spectral curvature, in brightness temperature units, is zero), and as a result of that, the SZE-21cm is smaller than the standard one. On the other hand, where the curvature is positive a larger number of photons is present and the SZE-21cm is higher than the standard one.

We also find that the minimum point in the input radiation spectrum ($\nu \approx 70$ MHz) corresponds to a maximum point in the SZE-21cm; this is due to the fact that a minimum point in the input spectrum means a smaller number of photons with respect to the standard CMB: as a consequence, when subtracting the input spectrum to calculate the SZE-21cm, the resulting emission is stronger than for the standard SZE. The opposite behaviour is observed at the frequencies where the input radiation spectrum has its maximum points ($\nu \approx 45$ and 120 MHz), that are close to the minimum points of the SZE-21cm; in this case, the correspondence is less precise (the minimum points of the SZE-21cm do not occur exactly at the maximum points of the input radiation spectrum) with respect to the previous case because the maximum points in the input spectrum are less sharp than the minimum one, and the convolution of photons with those at surrounding frequencies produces a slight shift in the frequency of the minimum points in the SZE-21cm (whereas in previous case of a minimum in the input radiation spectrum the convolution does not produce a shift in the frequency of the maximum points of the SZE-21cm).

Next, we focus on the SZE-21 cm spectrum produced in two specific cases. The first

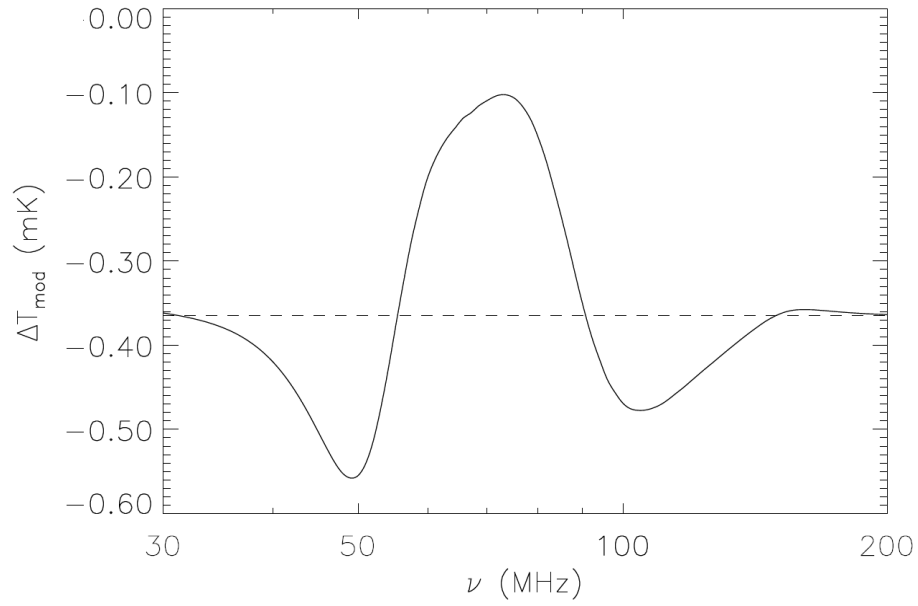


Figure 2.3: The SZE-21cm (solid line) calculated using the benchmark model (solid line in Fig 2.2) assuming an intracluster temperature of 7 keV and optical depth $\tau = 5 \times 10^{-3}$. The dashed line shows the standard SZE effect in the absence of the 21-cm perturbations (Colafrancesco et al. 2016b).

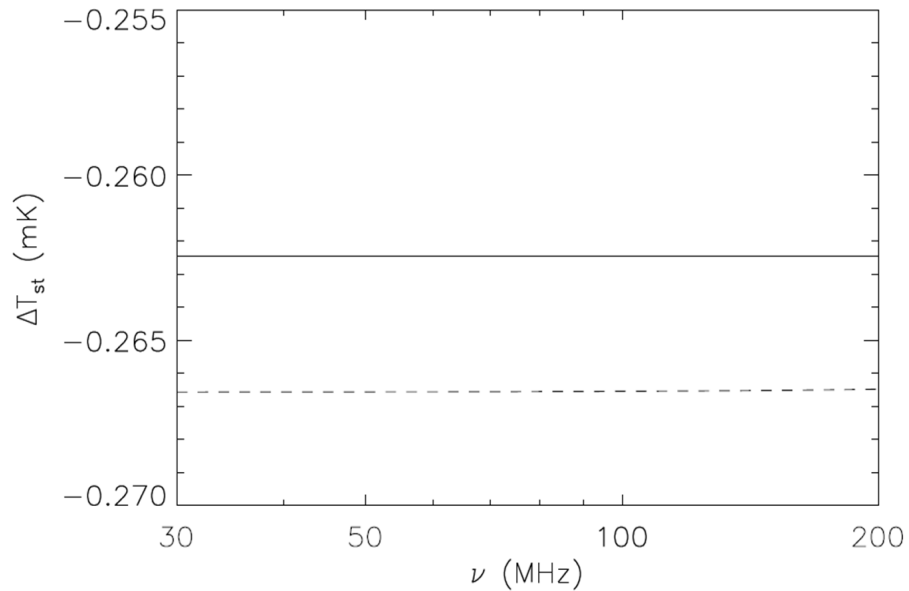


Figure 2.4: The standard SZE with no perturbation from the 21-cm for the case of a thermal electron gas of temperature 5 keV and optical depth $\tau = 5 \times 10^{-3}$ (solid line) and for the case of a non-thermal gas following a power-law distribution with minimum momentum $p_1 = 10$, $\alpha = 3.5$ and $\tau = 1 \times 10^{-4}$ (dashed line) (Colafrancesco et al. 2016b).

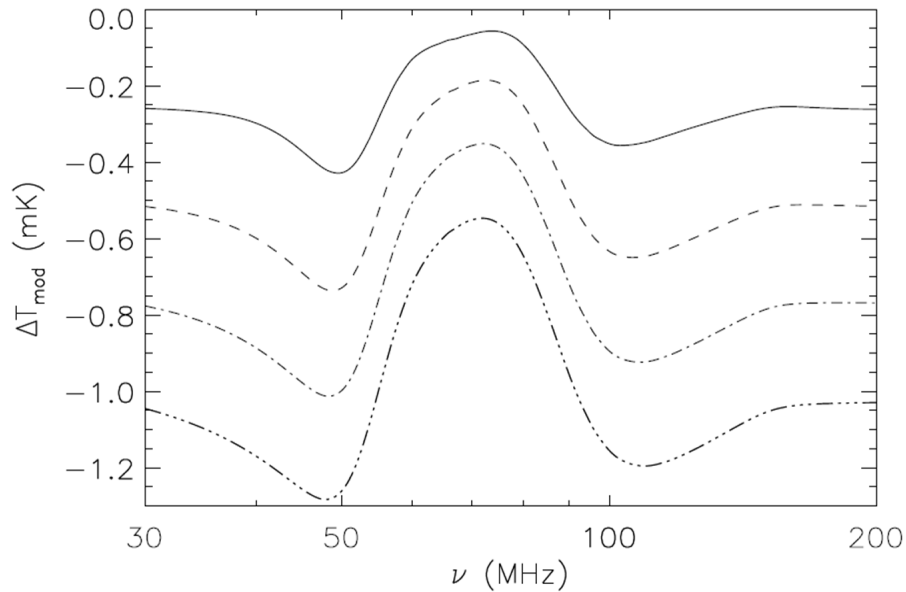


Figure 2.5: The SZE-21cm in the case of a thermal electron distribution illustrated for four different temperatures: 5 (solid), 10 (dashed), 15 (dot-dashed) and 20 (dash three dots) keV. A constant value of the optical depth, $\tau = 5 \times 10^{-3}$, is adopted (Colafrancesco et al. 2016b).

one is the SZE-21cm produced by the thermal electrons present in the atmosphere of galaxy clusters, and the second one is from non-thermal electrons that are present in cosmic structures where non-thermal activities are taking place, e.g. galaxy clusters with radio-halos and lobes of radio-galaxies.

2.6.2 Spectral Analysis

To start our discussion on the SZE-21cm produced in cosmic structures, we present, for the sake of clarity, the standard SZE whose input radiation spectrum is that of the usual CMB. This is shown in Fig 2.4 in units of brightness temperature mK, which illustrates the standard SZE (solid line) in the case of a thermal electron distribution of temperature 5 keV and optical depth $\tau = 5 \times 10^{-3}$. We also show the standard SZE for the case of a non-thermal electron distribution with optical depth $\tau = 1 \times 10^{-4}$ (dashed line), that follows a power-law shape with minimum momentum $p_1 = 10$ and spectral index $\alpha = 3.5$. As expected, in both cases, the SZE is constant in the frequency interval $30 < \nu < 200$ MHz, which falls in the Rayleigh-Jeans limit of the electromagnetic spectrum.

In Fig 2.5, we show the SZE-21cm for four different temperatures (5, 10, 15, 20 keV) of a thermal electron distribution with optical depth $\tau = 5 \times 10^{-3}$. The spectral shape of the SZE-21cm is dependent on the temperature of the plasma producing the IC scattering and the amplitude increases with temperature. This is in fact expected, since for the standard

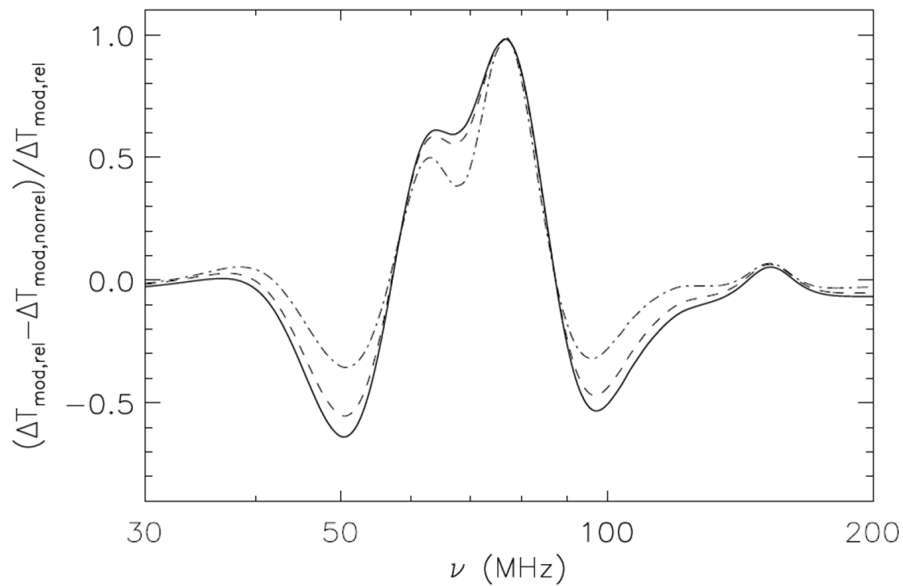


Figure 2.6: The fractional error between the relativistic and the non-relativistic approach plotted against frequency for thermal plasmas present in galaxy clusters with temperatures, 20 (solid line), 15 (dashed line) and 7 (dot-dashed line) keV (Colafrancesco et al. 2016b).

SZE, the spectral shape and the amplitude depend on the temperature, hence the SZE-21cm will also have a spectrum whose spectral feature and amplitude will be sensitive to temperature of the plasma.

To investigate the impact of relativistic effects on the SZE-21cm, we plot the fractional error produced when using the non-relativistic approach (as in Cooray 2006) over the correct relativistic one. We show our result for temperatures: 20 (solid line), 15 (dashed line) and 7 keV (dot-dashed line) in Fig 2.6. This shows that the fractional error is non-zero over almost the entire frequency interval. It is noticed that the local maxima of the percentage error is located at frequencies ($\nu \approx 50, 60, 77, 95$ MHz) where maxima and minima of the input spectrum occurs. This correspondence between the second derivative of the input spectrum and the fractional error is detailed in the Appendix. This is related, as discussed for the shape of the SZE-21cm, to the fact that the SZE is produced by a convolution of the input photon spectrum with photons at surrounding frequencies. The non-relativistic calculation (Birkinshaw 1999) considers a shape of the function $P_K(s)$ (see eq 1.27) which is narrower than the one in the relativistically correct calculation, $P_1(s)$ (see eq 1.24). Therefore, when the curvature (positive or negative) of the input radiation spectrum is maximum, the error produced by convolving the input spectrum with a function $P(s)$ narrower than the correct one is larger, because it implies to lose the contribution from the photons from more distant frequencies. As a consequence, the more the input spectrum is different from a straight line, the larger is the error produced by using the non-relativistic calculation. In the Appendix

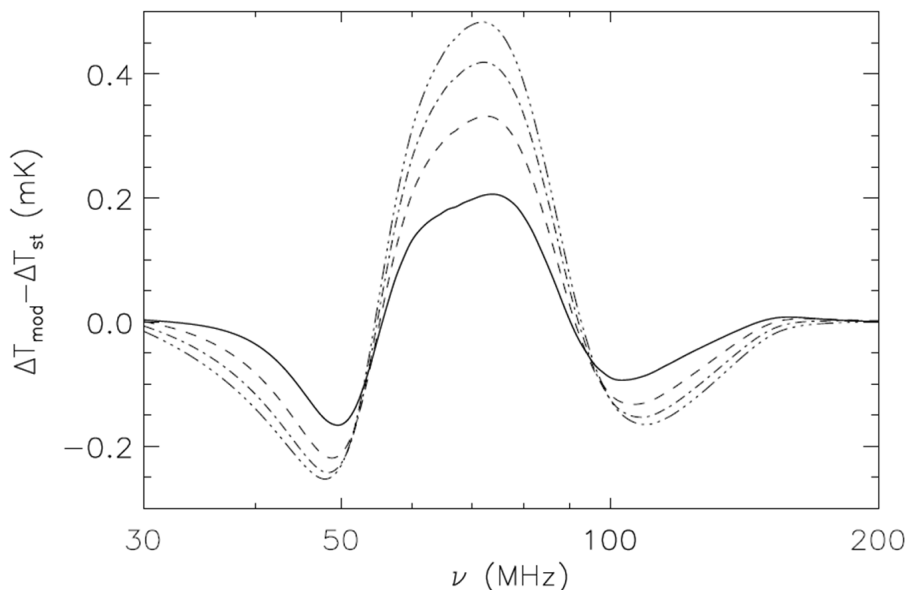


Figure 2.7: The difference, $\Delta T_{mod} - \Delta T_{st}$, between the SZE-21cm and standard SZE for galaxy clusters of temperatures 5 (solid), 10 (dashed), 15 (dot-dashed) and 20 (dash-three dots). The optical depth used is 5×10^{-3} (Colafrancesco et al. 2016b).

we expand these considerations by discussing also the other three input models considered for the input radiation spectrum.

For the case of a cluster with a temperature of 20 keV, the percentage difference reaches its local maxima/minima values of the order of $\approx 65\%$, $\approx 60\%$, $\approx 100\%$ and $\approx 50\%$ at frequencies $\nu \approx 50, 60, 77, 95$ MHz, respectively. Therefore, relativistic effects introduce substantial modifications to the SZE-21cm spectrum in comparison to its non-relativistic counterpart. For the other temperatures, the percentage error is smaller, but still of the order of at least 30% at the previous frequencies, and at ≈ 77 MHz the percentage error is $\approx 100\%$ independent of the cluster temperature. For this reason, it is very important to account for relativistic effects when computing the SZE-21cm, otherwise the correct shape of the spectrum will not be obtained.

Additionally, we compute the difference between the SZE-21cm and the standard SZE, $\Delta T_{mod} - \Delta T_{st}$ and the result is shown in Fig 2.7 for galaxy clusters hosting thermal plasmas of temperatures, 5 (solid), 10 (dashed), 15 (dot-dashed) and 20 (dash- three dots) keV. We notice that the main spectral differences occur around $\nu \approx 50$ MHz and in the interval $60 < \nu < 80$ MHz which reflects the Ly- α spin coupling, and also in the interval $100 < \nu < 150$ MHz which reflects the the UV ionization occurring during the EoR.

Furthermore, we compute the SZE-21cm for the case of non-thermal electrons that reside in galaxy clusters hosting radio-halos/relics and in the lobes of radio-galaxies. To do so, we use a single power-law distribution for various values of the minimum momentum p_1 and

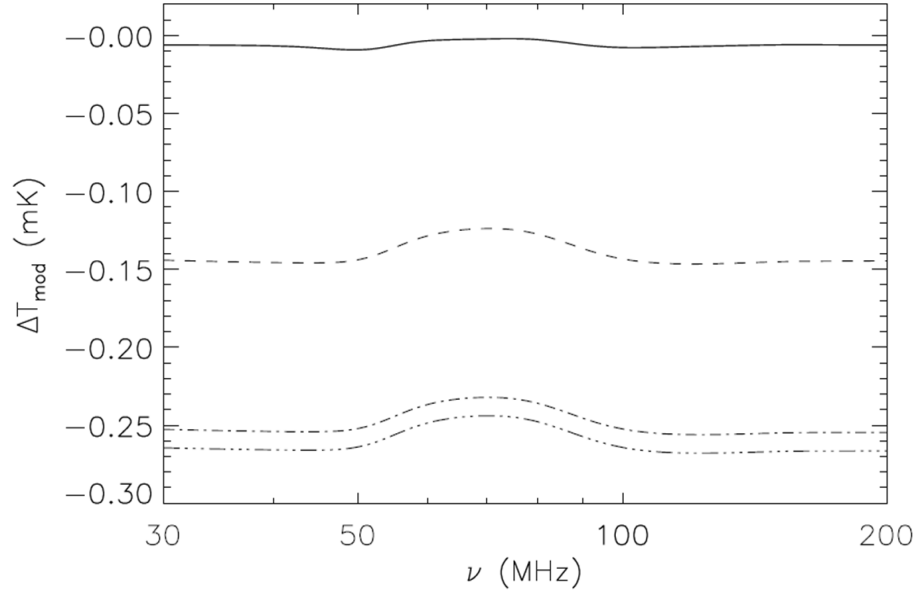


Figure 2.8: The SZE-21cm computed in the case of non-thermal electrons following a single power-law for values of the minimum momentum $p_1 = 0.1$ (solid line), 1 (dashed), 5 (dot-dashed), 10 (dash-three dots) and spectral index $\alpha = 3.5$. A value of $\tau = 1 \times 10^{-4}$ has been used (Colafrancesco et al. 2016b).

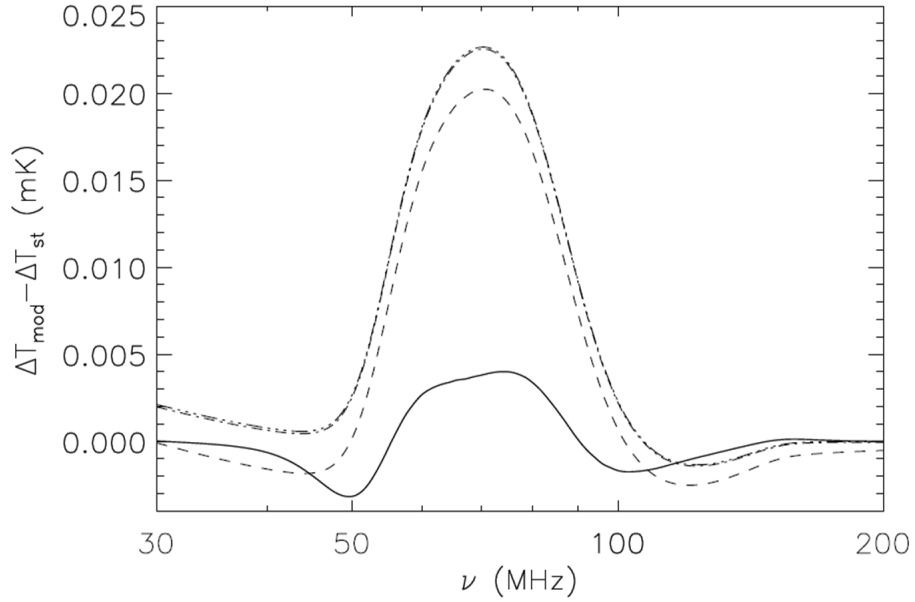


Figure 2.9: The difference between the SZE-21cm and the standard SZE, computed in the case of non-thermal electrons following a single power-law for values of the minimum momentum $p_1 = 0.1$ (solid line), 1 (dashed), 5 (dot-dashed), 10 (dash-three dots) and spectral index $\alpha = 3.5$. A value of $\tau = 1 \times 10^{-4}$ has been adopted (Colafrancesco et al. 2016b).

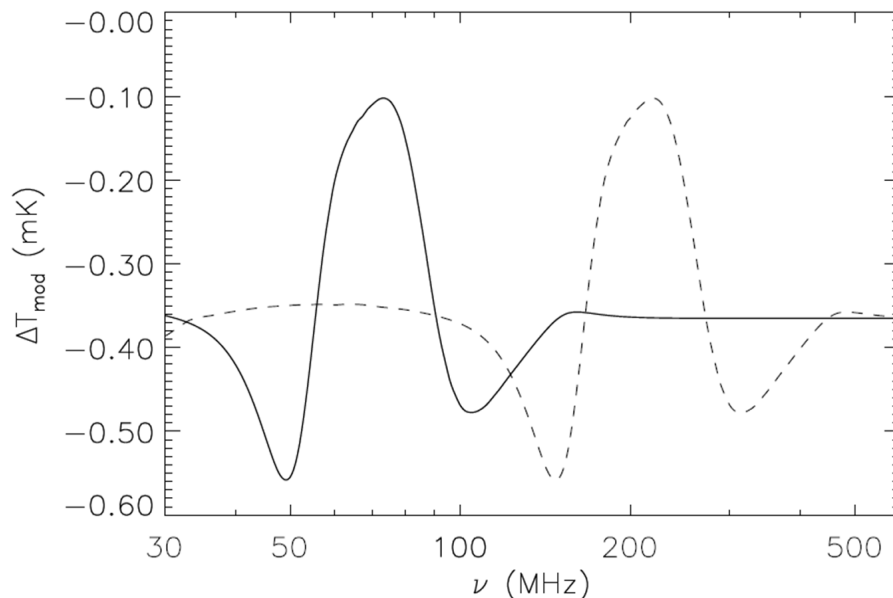


Figure 2.10: We show the SZE-21cm for a thermal plasma of temperature 7 keV and optical depth $\tau = 5 \times 10^{-3}$ in the standard benchmark model and for the case in which the background 21-cm is shifted by a factor of 3 in the frequency domain (Colafrancesco et al. 2016b).

constant spectral index, $\alpha = 3.5$ to describe the electrons. Fig 2.8 shows, for a constant value of $\tau = 1 \times 10^{-4}$, the result for $p_1 = 0.1$ (solid line), 1 (dashed), 5 (dot-dashed), 10 (dash-three dots). The amplitude of the non-thermal SZE-21cm is considerably small compared to the thermal one and this is particularly because the optical depth of non-thermal electrons is small ($\approx 10^{-5} - 10^{-4}$) compared to thermal ones ($\approx 10^{-3} - 10^{-2}$). However, notice that the amplitude increases with increasing values of p_1 . We also show the difference between the SZE-21cm and the standard SZE in this case, and the main differences occur in the same frequency intervals as in the thermal case. The result is shown in Fig 2.9 and again, the amplitudes are small compared to thermal ones because the optical depth of non-thermal electrons are small.

As a check, we also look at the SZE-21cm spectrum when the 21-cm background radiation is shifted in redshift (which will result in a shift in the observed frequency). This means that we are looking at the possibility that the redshifts of the various mechanisms in operation during the DA and the EoR (e.g. collisions, Ly- α interactions, UV ionization) can be different from the ones assumed in the benchmark model. As an illustrative example, we assume that the background 21-cm is shifted in the frequency domain by a global factor of 3 (which is equivalent to a shift in the redshift domain). We show our result in Fig 2.10 for the case of a thermal electron distribution of temperature 7 keV and optical depth $\tau = 5 \times 10^{-3}$. Thus, from the frequency at which the different effects in the SZE-21cm are observed, it is

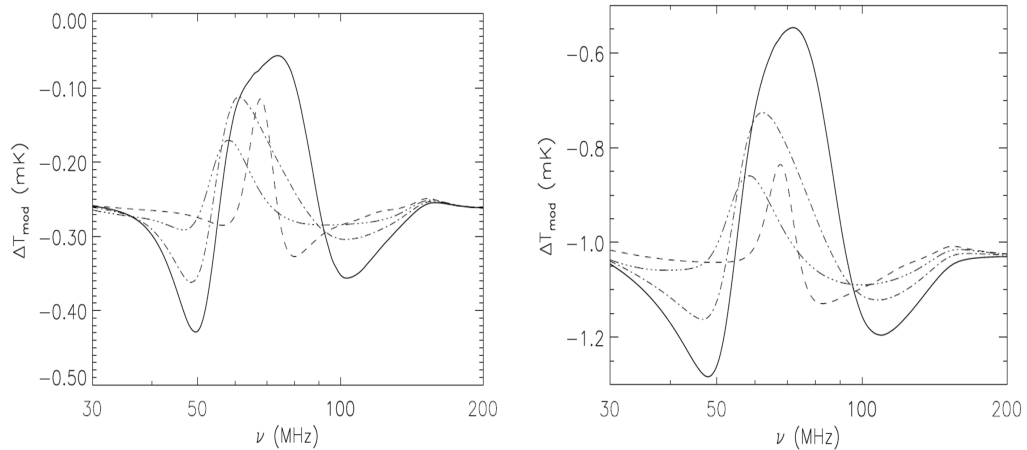


Figure 2.11: We show the SZE-21cm for a thermal electron distribution of temperature 5 (left) and 20 keV (right) for each model as the background radiation; fiducial model without dark matter (solid), extreme model without dark matter (dashed line), two fiducial models with dark matter with $M_{min} = 10^{-3} M_{\odot}$ (dot-dashed line) and $M_{min} = 10^{-6} M_{\odot}$ (three dot-dashed line). A constant optical depth value of 5×10^{-3} is used (Colafrancesco et al. 2016b).

possible to derive the redshift ($\nu = 1420/(1+z)$ MHz) at which these effects took place, and in principle determine the full cosmic history of the DA and EoR.

Finally we compute the SZE-21cm spectrum for the other three models and the results are shown in Fig 2.11 for a thermal electron distribution of temperature 5 and 20 keV. Additionally, we repeat the computation for the non-thermal case with spectral index $\alpha = 3.5$ for minimum momentum $p_1 = 0.1$ and $p_1 = 10$. We show the results in Fig 2.12. As we can see, while the spectral shape of the non-thermal SZE-21 cm is very similar to the thermal one for $p_1 = 0.1$, for high values of p_1 the main difference is the damping of the features produced by the Ly- α spin coupling effect at ≈ 60 and 100 MHz. The effect of considering a higher heating rate, both from usual astrophysical sources and from DM, is to increase the temperature of the IGM, to which the spin temperature is linked by the Ly- α coupling, and as a result the peak in the SZE-21cm in the 60-80 MHz frequency range is damped, with different spectral shapes depending on the dark matter properties.

2.7 Discussion

Using a full relativistic approach in calculating the SZE-21cm shows us the following important properties:

i) The non-relativistic approach produces substantial errors over almost the entire frequency interval over which the signal is expected. This is clearly shown in Fig 2.6 which

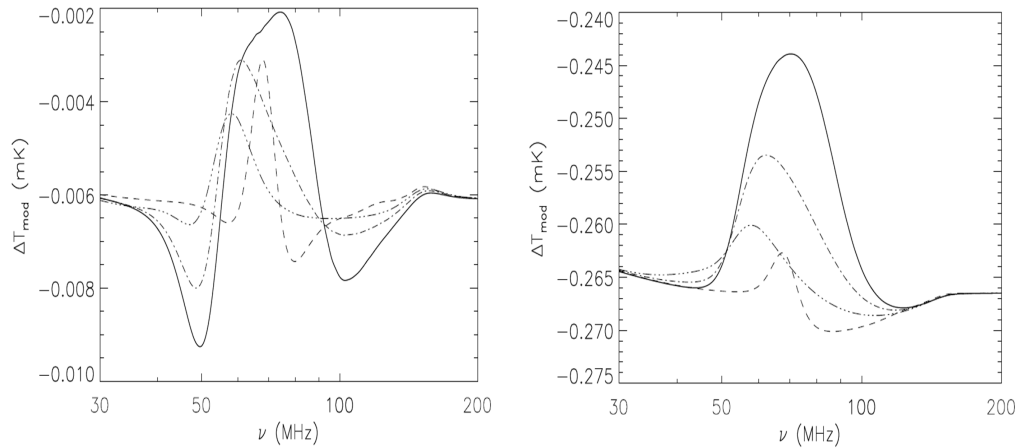


Figure 2.12: We show the SZE-21cm for non-thermal electron distributions of minimum momentum $p_1 = 0.1$ (left) and $p_1 = 10$ (right) for each model as the background radiation; fiducial model without dark matter (solid), extreme model without dark matter (dashed line), two fiducial models with dark matter with $M_{min} = 10^{-3} M_{\odot}$ (dot-dashed line) and $M_{min} = 10^{-6} M_{\odot}$ (three dot-dashed line). A constant optical depth value of 1×10^{-4} and spectral index $\alpha = 3.5$ are used (Colafrancesco et al. 2016b).

shows that relativistic effects are consequential if one wants to use the SZE-21cm to probe the DA and the EoR.

ii) Our approach allows us to calculate the SZE-21cm for any general electron distribution and we have shown our results for the case of thermal and non-thermal electrons. The amplitude of the SZE-21cm increases with temperature in the thermal case and the minimum momentum p_1 in the non-thermal case. The non-thermal SZE-21cm will allow the use of SZE to probe the DA and EoR using galaxy clusters hosting radio-halos/relics and also the lobes of radio-galaxies. Using radio-galaxies together with galaxy clusters will extend the sample of cosmic structures in which the SZE-21cm is being searched.

iii) The spectral feature of the SZE-21cm would allow the possibility of deriving important information on physical mechanisms presented during the DA and EoR. It will also allow to put constraints on the nature of dark matter due to the fact that dark matter annihilation have an impact on the background 21-cm spectrum as shown in Fig 2.2. This is subsequently present in the SZE-21cm spectra shown in Fig 2.11 and Fig 2.12.

iv) Finally we also saw that the SZE-21cm spectrum is sensitive to the electron distribution involved in the comptonization process. This means SZE-21cm can also be used to constrain the properties of electron populations that are hosted by atmosphere of cosmic structures at very low frequencies. This will be complementary to the use of high frequency SZE measurements to derive information on non-thermal properties of cosmic structures (Colafrancesco et al. 2011).

2.7.1 Differential analysis techniques and foreground contamination

Measurements of SZE-21cm can be carried out using radio interferometers by differential observations towards and away from galaxy clusters or other cosmic structures hosting diffuse thermal and non-thermal plasmas. The direct establishment of the 21-cm background by measuring the total intensity of the sky will require an exact calibration using an external source and the measurement will suffer from galactic foregrounds which are uniform over angular scales larger than a cluster, such as the galactic synchrotron background at low frequencies. Being a differential measurement, the SZE-21cm will not have these complications. In addition, the SZE-21cm benefits from its redshift independence, which would allow measurements to be carried out up to high redshifts, hence reducing contamination from radio emissions coming from point or diffuse sources. This will allow the signal to be searched in a large number of sources, hence increasing the precision of the measurement.

The resulting modification to the 21-cm spectrum due to the thermal SZE-21cm is expected at the level of a few tenths mK brightness temperature relative to the CMB. Therefore, such a small modification is challenging to detect, but for upcoming radio interferometers (like the SKA), the specific spectral signatures would allow a relatively clean detection. In addition, multi-object SZE-21cm observations could be facilitated by the fact that the instantaneous field-of-view of upcoming interferometers is expected to be more than 100 square degrees and one expects to detect simultaneously hundreds or more cosmic structures in such wide fields.

The SZE-21cm is an effective tool in establishing the global features of the 21-cm spectrum produced during the DA and the EoR. Additionally, cluster population studies, e.g., cluster counts and redshift distribution, can also be carried out using the SZE-21cm which can be used as cosmological probes. To achieve these goals would require observational techniques which would allow the study of a large number of objects and also those at high redshifts.

Although differential measurements would avoid contamination from galactic foregrounds and background emissions on angular scales bigger than typical galaxies or lobes of radio-galaxies, synchrotron emission within the cosmic structure could be a source of contamination. However this contamination varies with luminosity distance as D_L^{-2} , which means that it will be less of a problem for structures at high redshift, given that the SZE-21cm is redshift-independent. For cosmic structures that are nearby, the radio emission from the structure will be much higher than the SZE-21cm signal. Therefore we show in Fig 2.13, for the case of the Coma cluster with redshift $z_{\text{Coma}} = 0.02$, the synchrotron emission compare with the SZE-21cm for a thermal electron distributions of temperature 5 and 20 keV. We also show on the same figure the synchrotron emission for a Coma-like cluster situated at

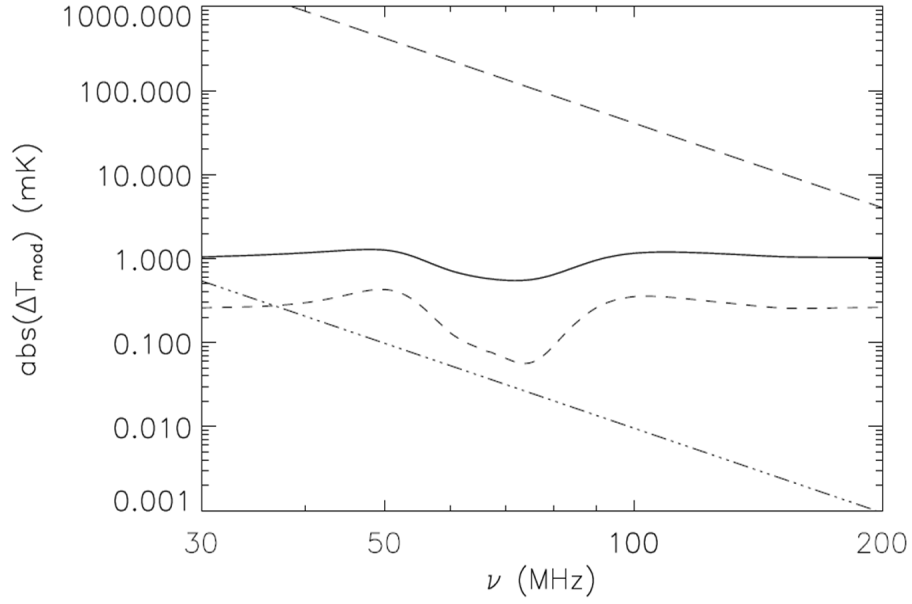


Figure 2.13: The SZE-21cm for thermal plasmas at 5 (short dashed line) and 20 (solid line) keV compared to the synchrotron emission for the Coma cluster with redshift $z_{\text{Coma}} = 0.02$ (Long dashed line) and for a Coma-like cluster at redshift $z = 1$ (dashed-three dots) (Colafrancesco et al. 2016b).

redshift $z = 1$.

2.7.2 Detectability with the SKA

In this section we investigate the possibility of measuring the SZE-21cm with sensitivity of the SKA instrument (Dewdney et al. 2012).

We first investigate the loss of signal due to the finite extent of the interferometer. To this aim, we calculate the SZE-21cm flux for a typical cluster hosting an isothermal gas whose electron density follows that of a β -profile as in eq 1.14. The optical depth at an angular distance from the center will be given by eq 1.17. We then assume $\tau_0 = 5 \times 10^{-3}$, $\beta = 0.75$, $\theta_c = 300$ arcseconds and calculate the flux up to $\theta_{\text{max}} = 10 \theta_c$.

At 110 MHz, the reference spatial resolution of SKA1-low which corresponds to a minimum baseline of 50 km is $\theta_{\text{min}} = 11$ arcseconds. The SZE-21cm to first order in optical depth τ is proportional to the product of the spectral part and the optical depth which allows us to estimate the lack of sensitivity on angular scales less than θ_{min} . This is given by the loss of flux within the angular range $\theta < \theta_{\text{min}}$ and is given by the ratio

$$\frac{\int_0^{\theta_{\text{min}}} 2\pi\theta\tau(\theta)d\theta}{\int_0^{\theta_{\text{max}}} 2\pi\theta\tau(\theta)d\theta} \approx 1.1 \times 10^{-4}. \quad (2.7)$$

In Fig 2.14, we show the standard SZE surface brightness profile at 110 MHz for a cluster at temperatures 20, 15, 10, 5 keV. Within a radius of 20 arcmin from the center of the galaxy

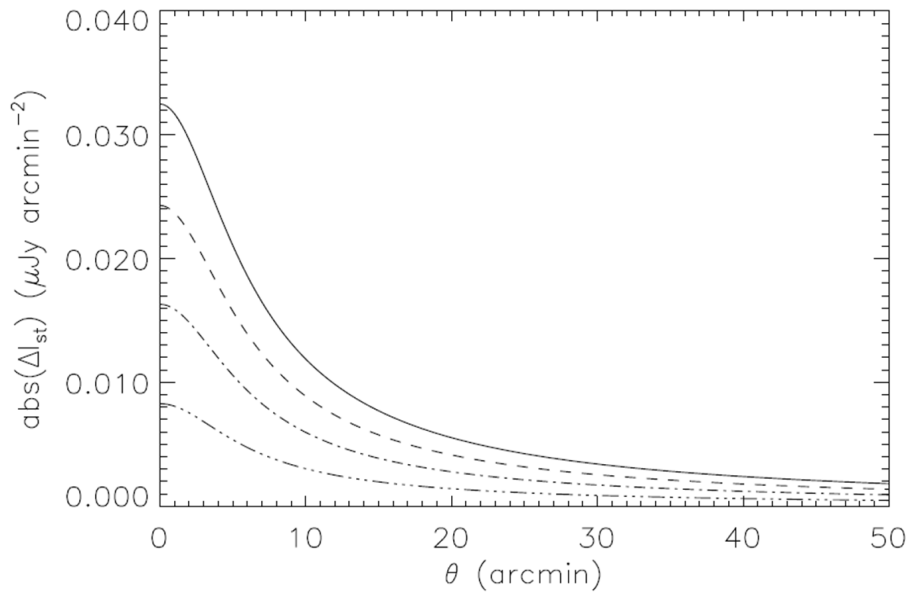


Figure 2.14: The surface brightness of the standard SZE calculated for a galaxy cluster at temperatures: 20 (solid line), 15 (dashed), 10 (dot-dashed) and 5 (three dots-dashed) keV assuming a value of $\tau_0 = 5 \times 10^{-3}$, $\theta_c = 300$ arcsec, $\beta = 0.75$ and $\theta_{\max} = 10\theta_c$ (Colafrancesco et al. 2016b).

cluster, the SZE signal would be around $\approx 10 \mu\text{Jy}$ and this is way above the loss of signal due to the finite baseline configuration of SKA1 which would be around 10 nJy.

To study the detectability of the SZE-21 cm signal, we compare the flux calculated for the SZE-21cm and the one calculated for standard SZE with the sensitivities of SKA-50%, SKA1, and SKA2 for 100 kHz bandwidth, 1000 hrs of integration, 2 polarizations, no taper, no weight. We show the results in Fig 2.15, 2.16, 2.17 and 2.18 for the different radiation background models we use in this work.

In Fig 2.15, for 1000 hours of integration time of a single cluster, we see that SKA-50 % will detect the SZE-21cm at frequencies > 80 MHz for clusters with high temperatures (20 keV) and for low temperature clusters at frequencies > 100 MHz. In the case of SKA-1 with 1000 hrs of integration, the SZE-21cm can be measured for frequencies > 75 MHz and > 90 MHz for high and low temperature clusters. Finally for the case of SKA-2, the signal can be measured as from 50 MHz for high temperatures and 80 MHz for low temperatures. This shows that the SKA will definitely be able to detect the SZE-21cm, hence shedding light on the DA and the EoR.

Measurements of the difference between the SZE-21cm and the standard SZE is a bit more challenging since the signal is only of a few μJy . Therefore measurements have to be done very precisely and in a strategic way by focusing on frequencies where the signal is at maximum, e.g ≈ 75 MHz at low frequencies and at higher frequencies, ≈ 115 MHz.

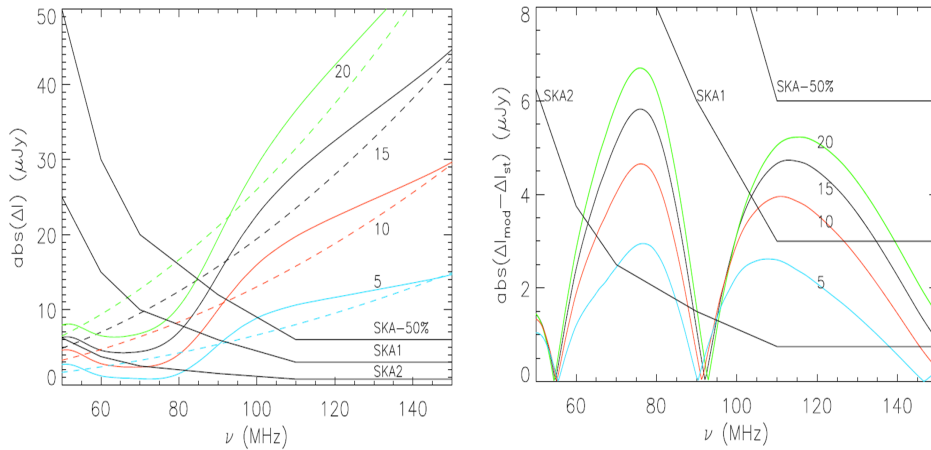


Figure 2.15: Left panel: The SZE-21cm (solid lines), ΔI_{mod} , and the standard SZE (dashed lines), ΔI_{st} , fluxes in μJy units. Right Panel: The absolute difference, $\Delta I_{\text{mod}} - \Delta I_{\text{st}}$, fluxes in the units of μJy . In both panels we are using the benchmark model, which is the one without extreme heating and in the absence of dark matter. The results are for thermal plasmas of temperature, 5 (cyan), 10 (red), 15 (black), 20 (green) keV computed for $\tau_0 = 5 \times 10^{-3}$, $\theta_c = 300$ arcsec, $\beta = 0.75$, $\theta_{\text{max}} = 10\theta_c$ (Colafrancesco et al. 2016b).

SKA-50 % at 1000 hrs of integration cannot measure this signal but for SKA-1, due to its high sensitivity at higher frequencies (around 110 MHz and above), measurement is possible for high temperature clusters (greater than 10 KeV). Although the signal is around only few μJy , the chance of detection can be enhanced if clusters are selected appropriately by focusing on those with high optical depths and temperatures. For the case of SKA-2, the signal can be measured for 1000 hrs of integration, right from ≈ 60 MHz for clusters with temperatures > 15 keV and at > 65 MHz for temperatures > 10 keV.

Regarding the other background models, at 1000 hrs of integration, SKA-1 and SKA-50% are not sensitive enough to detect the difference between the SZE-21cm and the standard SZE. On the other hand SKA-2 has a bigger chance of detecting the signal for these models. For the extreme model without dark matter, SKA-2 can detect the difference between the SZE-21cm and the standard SZE at frequencies ≈ 85 -110 MHz and at frequencies > 145 MHz for clusters with temperature $\gtrsim 10$ keV. For the dark matter model with $M_{\text{min}} = 10^{-3} M_{\odot}$, the signal can be detected in 75-80 MHz (for 20 keV) and 95-145 MHz (for temperatures greater than 5 keV) frequency intervals. For the one with $M_{\text{min}} = 10^{-6} M_{\odot}$, detection is possible at frequencies $\gtrsim 150$ MHz (for temperatures greater than 10 keV).

The SZE-21cm relies on the properties of the ICM; however, information regarding this can be obtained from standard SZE measurements at high frequencies ($\gtrsim 200$ MHz) or X-ray measurements (Arnaud et al. 2010). At high frequencies, the SZE of galaxy clusters are unperturbed by the 21-cm signal and therefore parameters such as optical depth and tem-

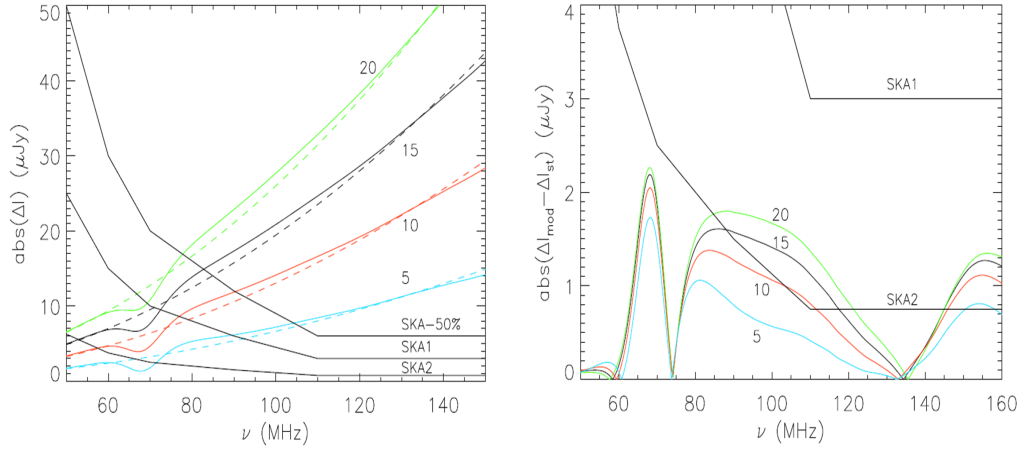


Figure 2.16: Same as Fig 2.15 but for the model without dark matter but with extreme heating (Colafrancesco et al. 2016b).

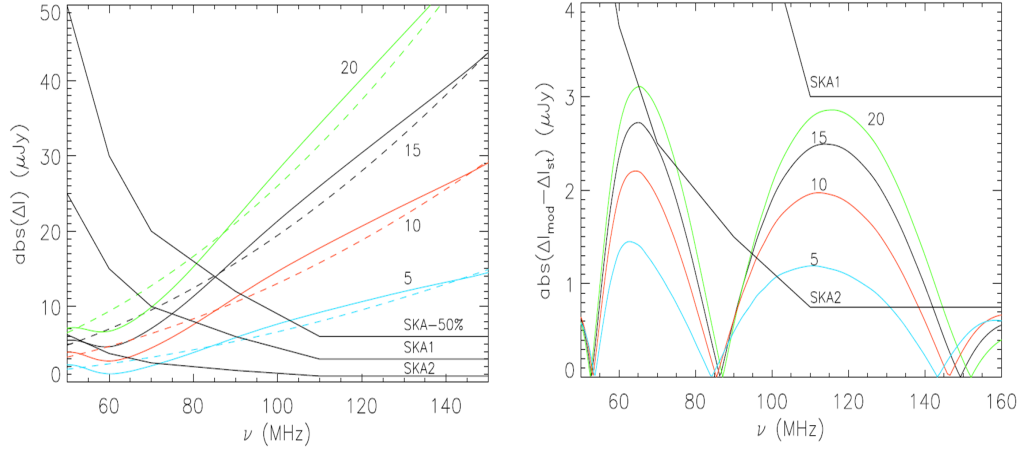


Figure 2.17: Same as Fig 2.15 but for the model with dark matter for $M_{min} = 10^{-3} M_{\odot}$ (Colafrancesco et al. 2016b).

perature can be derived. These parameters of the ICM from these measurements can then be used in deriving the SZE-21cm. Precise derivation of the optical depth and temperature is important since the SZE-21cm is sensitive to both parameters.

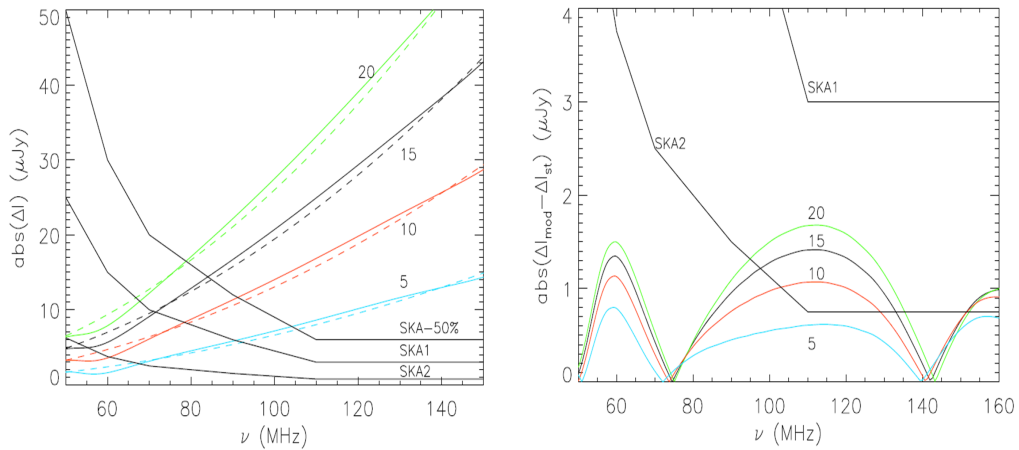


Figure 2.18: Same as Fig 2.15 but for the model with dark matter for $M_{min} = 10^{-6} M_{\odot}$ (Colafrancesco et al. 2016b).

2.8 Conclusion

We have been able to derive and use a full relativistic approach which can also incorporate any electron distribution to describe the SZE-21cm. Our results show that accounting for relativistic effects is mandatory for describing the SZE-21cm, in particular for clusters at high temperatures and also for cosmic structures (galaxy clusters with radio-halos and radio-galaxies) in which non-thermal activities are taking place. We have been able to use 21-cm models that have realistic physical processes. Extreme heating mechanisms as well as the presence of dark matter annihilation, and the spectral features of the SZE-21cm associated with each one of them have been highlighted and discussed. This has shown that SZE-21cm is definitely an effective tool in our arsenal for probing the Universe around the DA and the EoR together with the potential in setting constraints on the nature of dark matter and its impact in the early Universe.

The SZE-21cm is a weak signal on the order of μJy , however, with good observational and theoretical strategies, the measurement is possible with the SKA. A good line of attack would be to search for the signal in cosmic structures with high temperatures and optical depth in order to maximize the signal. In addition to that, selecting appropriately the frequency intervals over which the signal is expected to be high would also optimize the chance of detection, e.g. within 90 and 120 MHz. We have seen that SKA-1 is good enough in terms of observational sensitivities to set constraints on the benchmark model at 1000 hrs of integration. For the other models, only SKA-2 will be able to differentiate between the SZE-21cm and the standard SZE, hence constraining extreme conditions and the role of dark matter during the DA and EoR.

We have also addressed the possible contaminations that SZE-21cm measurements in

cosmic structures can suffer from. Within the angular scale of the cosmic structure, synchrotron emission from radio sources can contaminate the wanted signal. However these radio emission signals decrease with luminosity distance as $1/D_L^2$ and the SZE-21cm is redshift independent. Therefore searching for SZE-21cm in high redshift objects can alleviate this problem hence providing cleaner measurements.

Detection of SZE-21cm signal from non-thermal sources is very challenging due the fact that it is a factor of 100 fainter than the thermal one. However, the different spectral features can allow, in principle, a detection of this signal and hence an estimate of non-thermal cluster properties independently of measurements in other spectral bands. We note here that it is possible to strategize the search of this signal in objects where the non-thermal components are dominant, such as in the case of radio galaxy lobes. In this case, objects with more energetic electrons (i.e. with harder radio spectra), large optical depth (for which a good indication could be a strong radio luminosity) and high redshift are preferable.

The redshift-independent properties of the SZE-21cm would allow the signal to be searched in a large number of cosmic structures spanning over large cosmological distances. Statistical studies aimed at maximizing the detection can be performed to detect the 21-cm background which would allow us to understand the evolution of the cosmos during the DA down to the EoR and also the role of dark matter and its properties.

Chapter 3

Non-Planckian effects

The Planck spectrum of blackbody (BB) radiation is the spectral energy shape of photons that are in thermodynamic equilibrium with matter. Such a spectrum is possible if interaction between the photons and matter are small enough to avoid substantial absorption and irreversible attenuation of electromagnetic radiation (Landau & Lifshitz 1980). The CMB satisfies this requirement and shows the spectral shape of a Planck distribution when it decoupled from matter at the recombination epoch ($z_{\text{rec}} \approx 1400$). This is expected theoretically and has been verified by observations that the spectrum of the CMB is very close to the shape of a Planck BB distribution (Fixen et al. 1996).

For non-ionized media, such as e.g. neutral gases, the dispersion relation for electromagnetic radiation is given by

$$\omega = ck, \quad (3.1)$$

where k is the wavenumber and ω is the angular frequency of the photon. On the other hand for media that are ionized, such as e.g. an ionized plasma, the dispersion relation is modified and is given by (Triger & Khomkin 2010)

$$\omega^2 = c^2k^2 + \Omega_p^2 \quad (3.2)$$

where $\Omega_p = 2\pi\nu_p$ is the angular plasma frequency associated with a plasma frequency given by, $\nu_p = \sum_{i=1}^N n_i e^2 / (4\pi m_i \epsilon)$, where ϵ is the permittivity of free space and the sum is carried out over all charged species. This dispersion relation takes into account the coupling between the electromagnetic radiation and the collective behaviour of the plasma (Kittel 1986). Consequently, there are no photons with frequencies less than ν_p in the final distribution of photons. The absence of photons at frequencies less than the plasma frequency, x_p (which is written in terms of dimensionless frequency $x_p = h\nu_p / k_B T_0$) will alter the spectral shape of the final equilibrium radiation spectrum. Therefore, for systems with the presence of ionized matter, the equilibrium spectrum will no longer be the usual Planckian spectrum, but a modified one in which the non-zero value of the plasma frequency is taken into account.

A general form of photon distribution subjected to NP effects related to the non-zero value of the plasma frequency has been derived for astrophysical systems such as the CMB (Triger & Khomkin 2010) and the atmosphere of γ -ray bursts (Medvedev 1999). The relation, $\nu_p = \sum_{i=1}^N n_i e^2 / (4\pi m_i \epsilon)$, implies that the number density of charged particles in the plasma determines the plasma frequency. Consequently, NP effects associated with plasma frequency will also depend on this number density.

The dependence of the plasma frequency on the number density of charged particles implies that cosmological recombination history can be used, in principle, to calculate the plasma frequency. Based on that, a simple calculation of the plasma frequency at the recombination epoch using a number density of 300 electrons/cm³ yields a value ≈ 0.2 MHz (Triger & Khomkin 2010). This implies that for frequencies < 0.2 MHz, the intensity of the CMB would be zero. However, additional effects can impact this value and make it larger. The production of electrons and positrons via dark matter annihilation will introduce perturbations on the ionization fraction (Chen & Kamionkowski 2004, Dvorkin et al. 2013, Galli et al. 2009, Huetsi et al. 2009, Padmanabhan & Finkbeiner 2005). It has been demonstrated that the ionization fraction can increase by an order of magnitude leading to a plasma frequency of ≈ 1.5 MHz (Dvorkin et al. 2013). Another source of perturbation of the ionization fraction would be from hadronic collisions (Dermer 1986), which will also produce electrons and positrons and hence increase the number density of charged particles, consequently increasing the plasma frequency. The variation of the plasma frequency with redshift is given by $\nu_p \propto (1+z)^{3/2}$, which means that plasma effects create spectral distortions to the CMB well before the recombination epoch.

Other than spectral modifications related to the non-zero value of the plasma frequency, the CMB spectrum is also vulnerable to other sources of distortions such as the μ and y type distortions that are related to the frequency dependent chemical potential and Compton scattering respectively (Chluba & Sunyaev 2012). In addition that, small residual spectral distortion other than from the μ and y -type can be produced in the early Universe, such as Silk damping of small scale perturbations, the cooling of photons by electrons and baryons, the decay and annihilation of relic particles, primordial magnetic fields and evaporating primordial black holes (see e.g. Chluba & Sunyaev 2012, Chluba 2014). The plasma frequency would be another possible source of spectral distortions that could modify the CMB spectrum.

Spectral distortions associated to the μ and y type is expected at low redshift ($z < 10^6$) due to the fact that the three mechanisms responsible for thermalization in the early Universe become inefficient (see e.g. Procopio & Burigana 2009, Chluba 2014, Tashiro 2014). These three mechanisms are Compton scattering, double Compton scattering and bremsstrahlung. These physical processes were very efficient at redshift $z > 10^6$ and any other sources of

spectral distortions (see e.g. Chluba 2014) were erased by them. However for distortions created by the plasma frequency, the time scale of these processes exceeds the plasma time-scale, hence still allowing the possibility for the CMB spectrum to be vulnerable to plasma effects. The time scales, $t_{\text{comp}} = 1.23 \times 10^{29}/(1+z)^4$ s, $t_{\text{double}} = 1.34 \times 10^{40}[x^3/(e^x - 1)]/(1+z)^5$ s and $t_{\text{free}} = 8.59 \times 10^{26}[x^3/(e^x - 1)]/(1+z)^{2.5}$ s (Tashiro 2014), are larger than the plasma time scale defined by $t_p = 1/\nu_p$ (Padmanabhan 2000). As an example, at redshift $z = 1100$ and for a plasma frequency of 0.2 MHz which corresponds to $x_p = 2.5 \times 10^{-9}$, one obtains the values of $t_{\text{comp}} = 3.2 \times 10^{16}$ s, $t_{\text{double}} = 1.5 \times 10^7$ s, $t_{\text{free}} = 72$ s and $t_p = 6.4 \times 10^{-6}$ s; at $z = 10^6$ and a plasma frequency of 3 GHz corresponding to $x_p = 6.64 \times 10^{-8}$, we obtain $t_{\text{comp}} = 1.2 \times 10^5$ s, $t_{\text{double}} = 5.9 \times 10^{-5}$ s, $t_{\text{free}} = 3.8 \times 10^{-5}$ s and $t_p = 3.4 \times 10^{-10}$ s. Therefore these processes will eliminate effects due to other sources of spectral distortions and the eventual CMB spectrum will be a blackbody radiation spectrum modified by the plasma frequency. Measuring this spectrum will allow one to derive results regarding the plasma frequency.

3.1 Observables

So far, only theoretical arguments (Triger & Khomkin 2010) have been put forward regarding spectral modifications associated with plasma effects on the CMB and no observational strategies have been proposed. Taking into considerations that the time scale of plasma effects is smaller than thermalization processes as well as the possibility that the plasma frequency could be altered by some possible mechanisms occurring around the recombination epoch, it is desirable to devise some possible observational strategies. Therefore we look at the various observables that allow one to constrain possible NP effects on the CMB resulting from a non-zero plasma frequency around the recombination epoch.

In this section we look at the different CMB related observables through which NP effects can manifest. The first observable is CMB measurements, and to derive spectral constraints on NP effects, we use current observational data of the CMB, both at low and high frequencies, to investigate whether the uncertainties in the data can allow the possibility of a modified CMB spectrum with non-zero plasma frequency. The CMB spectrum is very well constrained at high frequencies by observations carried out by *COBE-FIRAS* instrument (Fixen et al. 1996), however, at low frequencies (Howell & Shakeshaft 1967, Sironi et al. 1990, 1991), below 1 GHz, uncertainties in measurements are large and this where the NP effects are expected.

Since NP effects will manifest themselves on the CMB, they will also be present in any observables that involve the CMB, such as the SZE and the cosmological 21-cm background. Therefore we also study the imprint of NP effects on the spectra of these observables.

3.2 Spectral modification of the CMB spectrum

The Planck spectrum is the spectral distribution of a photon gas that is in thermal equilibrium with neutral matter at temperature T . This is given, in terms of a-dimensional frequency x , in eq 1.23. In the case of the CMB, $T = T_0 = 2.725 \pm 0.001$ K. On the other hand, for matter that is ionized such as e.g. a plasma, with electron plasma frequency of x_p , photons are suppressed at frequencies below x_p and therefore the equilibrium distribution will be altered. Taking into consideration this effect, a generalized Planck distribution (Triger & Khomkin 2010) can be written as follows

$$\tilde{I}_0(x; x_p) = 2 \frac{(k_B T)^3}{(hc)^2} \frac{x^2}{e^x - 1} \sqrt{x^2 - x_p^2} H(x - x_p), \quad (3.3)$$

where $H(x - x_p)$ is the Heaviside step function (with values 1 for $x > x_p$ and 0 for $x \leq x_p$). The step-function $H(x - x_p)$ takes into account the fact that photons are suppressed at frequencies below x_p . The first noticeable feature of this distribution in comparison to the usual Planck one, is the existence of a cut-off frequency at the $x = x_p$ and below which, the intensity is zero. Large contrasts between the two spectra can be seen for $x_p > 1$, however, appreciable differences can still be seen for $x_p < 1$, in particular at low frequencies around $x = x_p$.

In order to carry out the investigation of NP effects associated with plasma frequency, we use CMB measurements carried out by *COBE-FIRAS* at high frequencies and those obtained in the range ≈ 1.3 -50 GHz by other experiments. We fit the CMB data with the generalized Planck spectrum of eq 3.3 and minimize the χ^2 with respect to the parameter x_p . The CMB temperature is kept fixed to the measured value of *COBE-FIRAS* although it can be treated as a free parameter. This is reasonable given that the measurements of the CMB spectrum from which the temperature is derived in the *COBE-FIRAS* mission has been performed at high frequencies, where NP effects can be neglected. We found that the $\chi^2 = 1$ for a value of $x_p = 0$ which implies that the standard Planck spectrum is the best fit curve to the data. However, measurement uncertainties at low frequencies allow us to set upper limits on the value of x_p which are $x_p \lesssim (3.63, 6.10, 7.36) \times 10^{-3}$ for 1σ , 2σ and 3σ confidence level (c.l.), corresponding to frequencies of 206, 346 and 418 MHz, respectively. The results obtained are shown in Fig 3.1 where the NP effect is shown over the entire frequency interval, indicating that at 3σ , it is not possible to distinguish between the standard Planck spectrum and the generalized one.

We show in Fig 3.2, zooming around the low frequencies, $\nu < 1$ GHz, the CMB spectrum together with measurement uncertainties and also the modified CMB spectrum for upper-limits on x_p at 1σ , 2σ and 3σ . The result shows that the intensity of the CMB goes to zero below ≈ 206 MHz, i.e. for the value of $x_p = 3.63 \times 10^{-3}$ at 1σ c.l., or below ≈ 418 MHz, i.e. for the value of $x_p = 7.36 \times 10^{-3}$ at 3σ c.l. Another noticeable feature that one actually sees

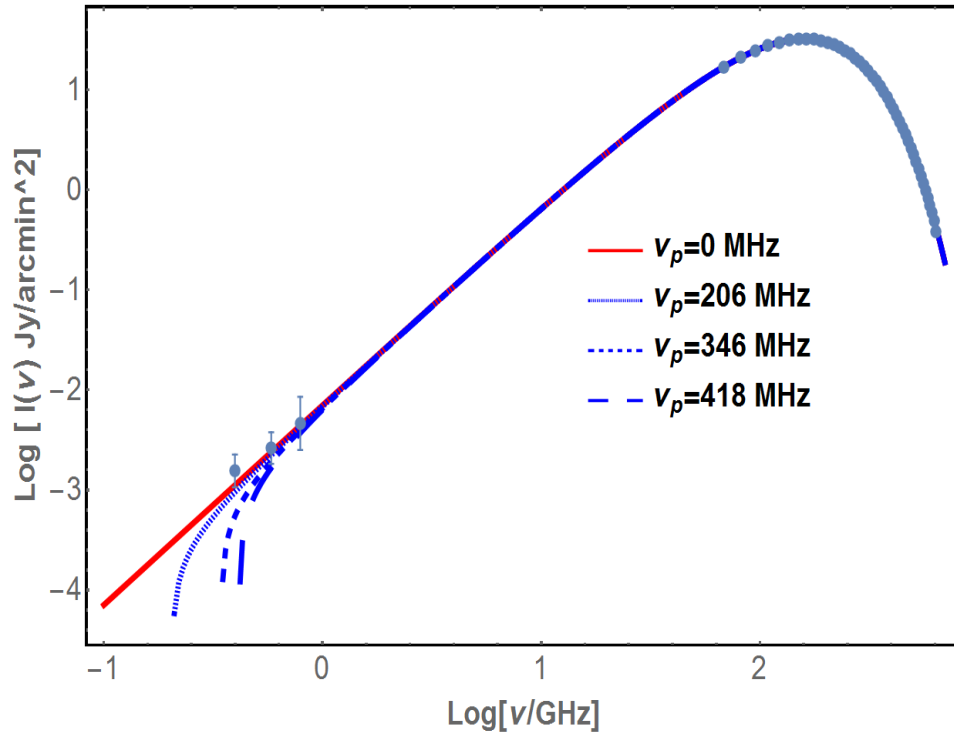


Figure 3.1: The non-Planckian spectral distribution of the CMB for different values of the plasma frequency ν_p as derived from the fit to the data. The experimental data are shown for both low (Howell & Shakeshaft 1967, Sironi et al. 1990, 1991) and high frequencies (Fixen et al. 1996). Other data in the range $\sim 1.3 - 50$ GHz obtained from ground-based, balloon-borne and from the *COBE-DR* experiment (see http://asd.gsfc.nasa.gov/archive/arcade/cmb_spectrum.html) are not shown here but they lie almost exactly along the curves of the CMB spectrum shown in the plot.

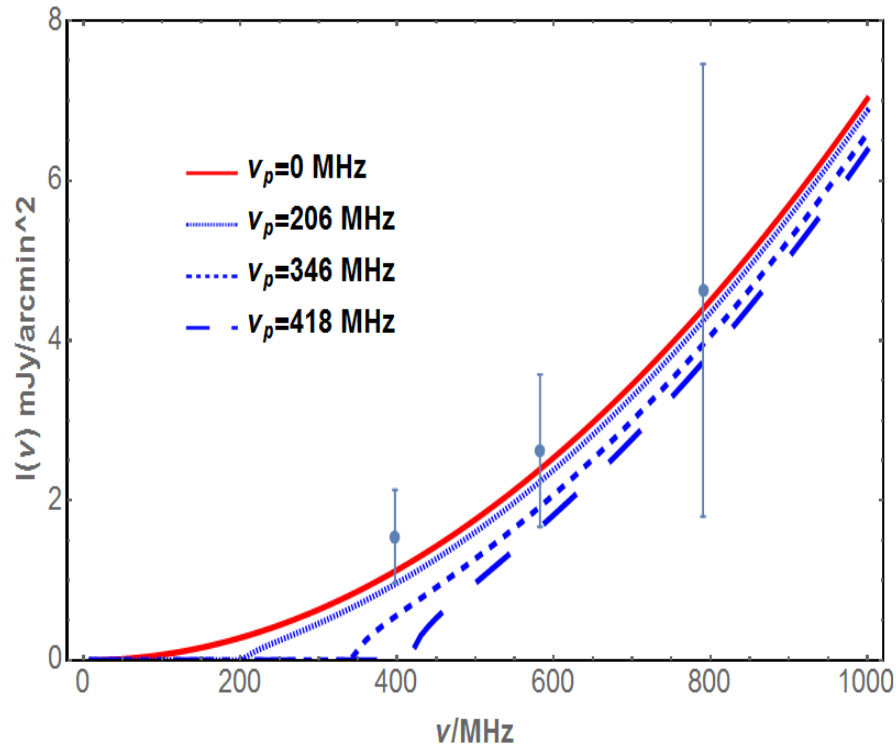


Figure 3.2: The non-Planckian effects due to a finite value of the plasma frequency ν_p on the CMB spectrum at $\nu < 1 \text{ GHz}$ for different values of the upper limit on ν_p as obtained from the fit to the CMB spectrum data (Colafrancesco et al. 2015a). Experimental data are from Howell & Shakeshaft 1967, Sironi et al. 1990, 1991.

in the modified CMB spectrum is that for increasing values of x_p , the spectrum decreases and the corresponding frequency at which the maximum occurs increases (see Fig 3.3). The amplitude of the CMB intensity variation due to NP effects is of order of \approx mJy/arcmin² at low- ν while it is of order of \approx 0.1 mJy/arcmin² at high- ν . Therefore, the best frequency region to look experimentally for these effects is at low radio frequencies, $\nu < 1000$ GHz. Our result presented here demonstrate that low frequency CMB measurements (< 1000 GHz) would allow constraints to be put on spectral modifications of the CMB spectrum associated with plasma effects around the recombination epoch. For future upcoming low-frequency instruments such as SKA (Dewdney et al. 2012) and HERA (Backer et al. 2010), low frequency measurements could be a good observational strategy to search for NP effects on the CMB spectrum.

Although we have demonstrated that CMB measurements, in particular at low frequencies, can be used as a direct probe of the possible NP effects, there are many considerations that have to be taken into account. Measurements at low frequencies are very challenging and susceptible to various experimental and systematic biases. In addition to that, galactic radio foregrounds (de Oliveira-Costa et al. 2008) would pose a nuisance to the measurement and therefore have to be subtracted carefully. Although the SKA will have very good observational capacities, the foreground contamination and the component separation of the such a diffuse signal will still be present. In regard to these issues, it is wise to explore other observables that are dependent on the CMB to explore the existence of NP effects. Therefore the next observable that we explore is the SZE. This observable is directly related to the CMB, which consequently means that any NP distortions present in the CMB will also be reflected in the SZE.

3.3 The SZE_{NP}

In order to calculate the SZE for the case of a NP distribution, we use eq 3.3 as the input spectrum in eq 1.22. This is very similar to the calculation of the SZE-21cm in Chapter 2, whereby the input spectrum was that of a modified CMB due to processes involved around the EoR. Therefore to compute the SZE for a modified CMB due to NP effects associated with a non-zero plasma frequency, we insert the generalized Planck distribution (eq. 3.3) as the input radiation into eq. 1.22, which is done as follows:

$$\Delta\tilde{I}(x; x_p) = \tau \left[\int ds P_1(s) \tilde{I}_0(xe^{-s}; x_p) - \tilde{I}_0(x; x_p) \right]. \quad (3.4)$$

where $\tilde{I}_0(x; x_p)$ is generalized Planck distribution (eq. 3.3).

We compute the modified SZE effect (SZE_{NP}) for the case of a thermal electron gas of optical depth $\tau = 10^{-3}$ for different temperatures: 5, 10, 15, 20 keV. We show the result in Fig 3.4 for the different upper limit values of x_p derived from the CMB spectrum.

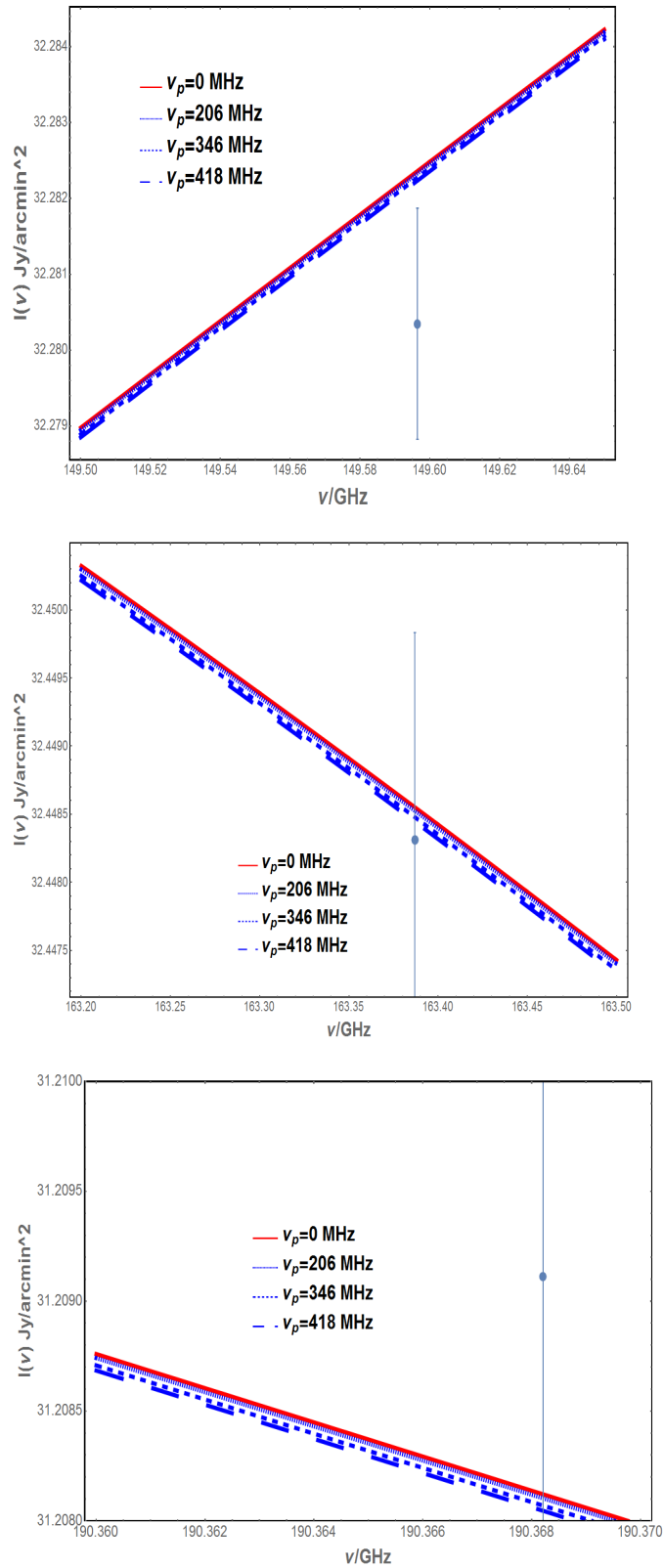


Figure 3.3: The effect of a non-Planckian distribution on the CMB spectrum in frequency range 143 GHz to 191 GHz is shown for different values of the plasma frequency x_p (Colafrancesco et al. 2015a). Experimental data are from *COBE-FIRAS* (Fixen et al. 1996).

The first spectral feature that is noticed in the SZE_{NP} is a peak that occurs exactly at the plasma frequency x_p and is independent of cluster temperature. This provides us with a direct observational probe to measure the plasma effect imprinted on the CMB around recombination by making use of local galaxy clusters. The SZE_{NP} opens a door that give us access to the physics of the early Universe using the local one.

The amplitude of the peak increases with increasing temperature and density of the electron gas. The spectral shape of the thermal SZE_{NP} is very peculiar and it is peaked in a quite narrow frequency range of the order of $\Delta\nu \approx 20$ MHz for $kT = 5$ keV and $\Delta\nu \approx 50$ MHz for $kT = 20$ keV, reflecting the relativistic effects of the electron distribution in the photon re-distribution function $P_1(s)$. At frequencies larger than 1 GHz, the SZE_{NP} becomes close to the standard Planckian one, i.e. the standard SZE calculated using the usual CMB Planck spectrum.

In addition to a thermal gas, we also look at the spectral shape of the SZE_{NP} when the electrons involved in the IC scattering process are of non-thermal origins, which typically happens in galaxy clusters hosting radio-halos and radio galaxies (see e.g. Ensslin & Kaiser 2000, Colafrancesco et al. 2003). Hence, for completeness, we compute the SZE_{NP} for the case of a single power law distribution of electrons with spectral index $\alpha = 2.5$ for different minimum momentum p_1 and the result is shown in Fig 3.5. In the non-thermal case, the peak of the SZE_{NP} decreases with increasing value of p_1 because the high-energy electrons tend to scatter the photons to high frequencies. However, just like in the thermal case, the peak occurs at corresponding value of x_p , independent of the electron distribution parameter p_1 . The width of the SZE_{NP} spectrum (see Fig.3.5) is larger due to the enhanced impact of the relativistic effects of the high-E electron population and its shape reflects therefore the different nature of the scattering plasma. Possible observations of the SZE_{NP} can therefore address the question of the intrinsic nature of the plasma in the target cosmic structure (e.g., galaxy clusters vs. radio galaxies).

In order to address the issue of detectability, we calculate the SZE_{NP} spectrum integrated over an area of 5 arcmin radius using parameters of the Bullet cluster, $kT_e = 15$ keV. Fig 3.6 shows the difference between the SZE spectrum $\Delta\tilde{I}$ and ΔI compared to the sensitivity of the SKA1 and SKA50% for 1000 hrs of observations and to the eVLA sensitivity for 12 hrs of observation. We found that the values for the plasma frequency $\nu_p = 206, 346$ and 418 MHz at 1, 2 and 3 σ C.I, derived from the analysis of the CMB spectrum, can be detected with both SKA-LOW and SKA-MID band1 (350-1050 MHz).

3.4 Modification to the 21-cm background

The frequency interval over which NP effects are expected coincides with the one over which the cosmological 21-cm background (see e.g. Pritchard & Loeb 2012) is expected. In regard

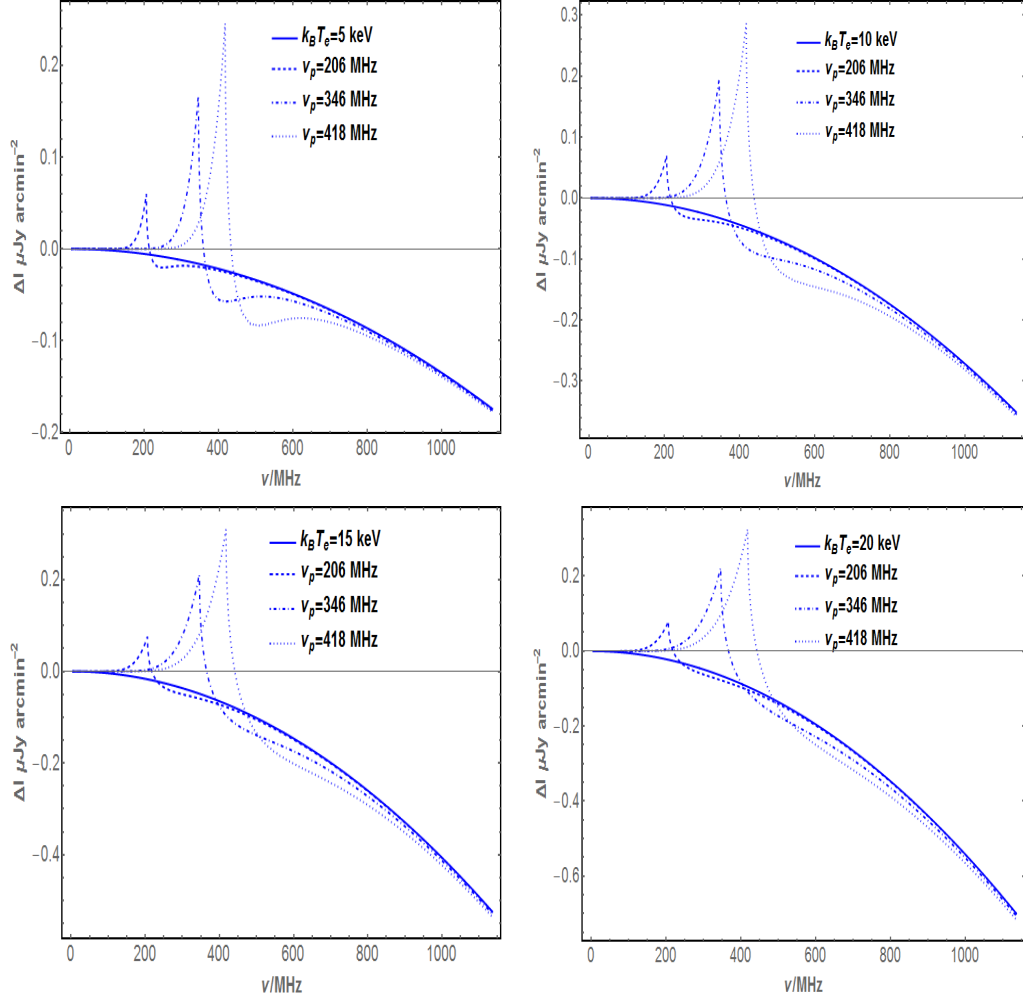


Figure 3.4: The thermal SZ effect spectral distortions computed for galaxy clusters with increasing plasma temperature (see various panels) for a standard Planck distribution (solid line) and including the effect of non-Planckian distribution of photons for the values of the plasma frequency x_p derived at 1σ , 2σ and 3σ level. The cluster plasma optical depth is fixed to the value $\tau = 0.001$ (Colafrancesco et al. 2015a).

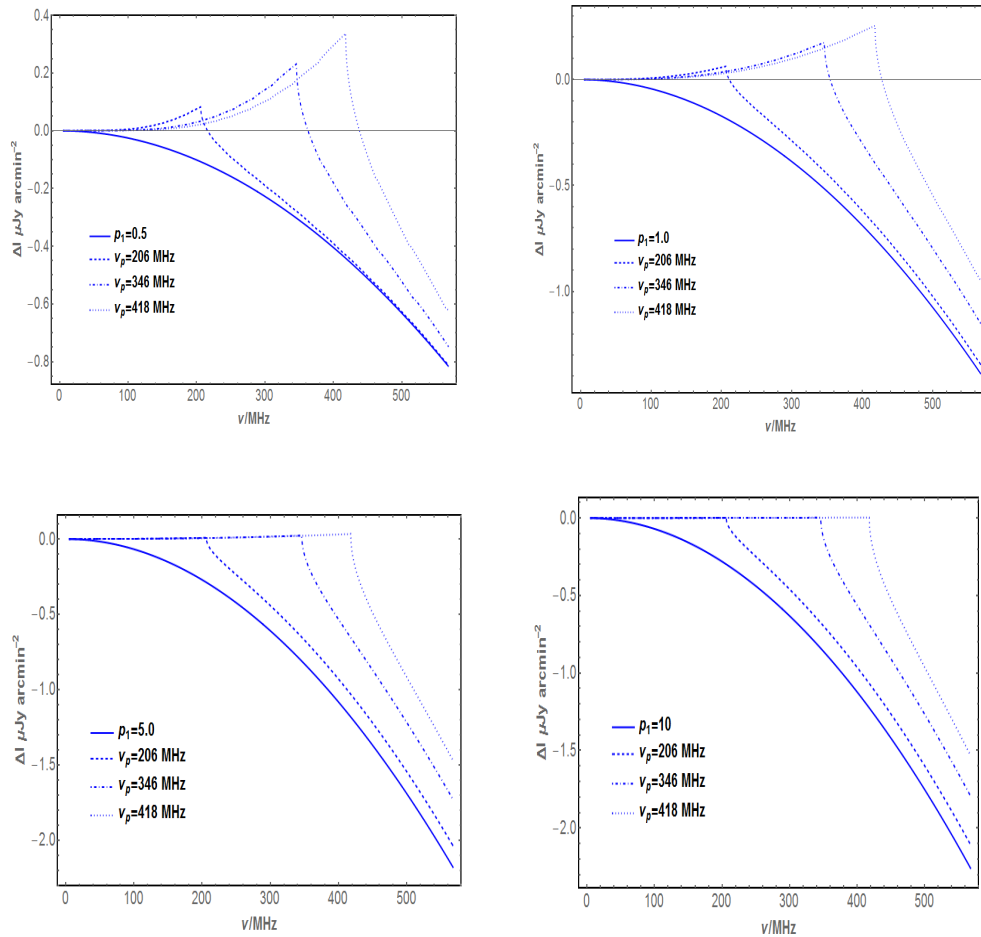


Figure 3.5: The non-thermal SZE spectral distortion for the case of non-thermal plasmas with increasing electron minimum momentum p_1 (see various panels) for a usual Planck distribution (solid line) of photons and the effect of non-Planckian distribution at 1σ , 2σ and 3σ level computed in the case of a single power law for different minimum momentum p_1 . We use here an optical depth of $\tau = 0.001$ (Colafrancesco et al. 2015a).

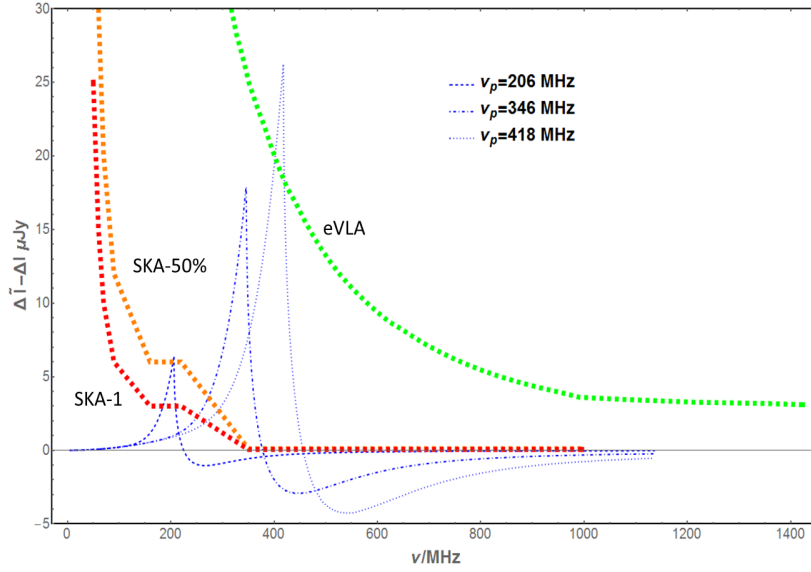


Figure 3.6: The difference between the SZE_{NP} and the Planck SZE for a Bullet-like cluster with temperature of 15 keV (see Markevitch et al. 2002) subtending an angle of $5'$ to its R_{500} . An optical depth of $\tau = 0.001$ is assumed. The SKA1 (red) and SKA-50% (orange) sensitivity is calculated for 1000 hrs integration while the eVLA sensitivity (green) is calculated for 12 hrs integration (Colafrancesco et al. 2015a).

to this, it becomes desirable to analyze the NP effect related to the plasma frequency on the spectral shape of the cosmological 21-cm background. To make this investigation, we perform our spectral analysis in terms of brightness temperature $\delta T(\nu)$, which is given by eq 2.1.

For a Planck spectrum, the 21-cm emission appears as a perturbation on the CMB which therefore we can write as

$$\delta T(\nu) = T_{21}(\nu) - T_0(\nu), \quad (3.5)$$

where T_{21} is the brightness temperature associated with the 21-cm background and T_0 is that of the CMB. A generalization of the previous relation which takes into account NP effects is given by

$$\delta \tilde{T}(\nu; \nu_p) = \tilde{T}_{21}(\nu; \nu_p) - \tilde{T}_0(\nu; \nu_p). \quad (3.6)$$

The plasma frequency x_p is fixed and therefore two frequency regimes are distinguished

i) $\nu < \nu_p$: in this case $\tilde{T}_0 = 0$, and therefore $\delta \tilde{T} = \tilde{T}_{21}$. If we assume that $\tilde{T}_{21} \approx T_{21}$, i.e. the 21-cm background is not sensibly changed by the NP spectral distortion, as is expected because the main physical processes affecting the 21-cm background depend on the global temperature of the system which is not heavily affected by a distortion at small frequencies, then we can write:

$$\delta \tilde{T} = \delta T + T_0, \quad (3.7)$$

so the frequency change of the brightness temperature is the same as in the Planckian case, but its amplitude is shifted by a value T_0 (that in the RJ region has a constant value equal to the CMB temperature);

ii) $\nu > \nu_p$: in this case we can write the NP modified spectrum in the RJ region as:

$$\tilde{I}_0 \propto x \sqrt{x^2 - x_p^2} = x^2 \sqrt{1 - \frac{x_p^2}{x^2}}, \quad (3.8)$$

and the corresponding brightness temperature is:

$$\tilde{T}_0 = T_0 \sqrt{1 - \frac{x_p^2}{x^2}}. \quad (3.9)$$

By assuming again $\tilde{T}_{21} \approx T_{21}$, the change in the temperature brightness is given by:

$$\delta\tilde{T} = \delta T + T_0 - \tilde{T}_0 = \delta T + T_0 \left(1 - \sqrt{1 - \frac{x_p^2}{x^2}} \right). \quad (3.10)$$

In Fig 3.7, we show the spectrum of $\delta\tilde{T}$ for different values of the plasma frequency ν_p from 0.2 to 100 MHz by assuming the standard benchmark model (see Cooray 2006). For $\nu < \nu_p$, the change of $\delta\tilde{T}$ is the same as δT obtained using the usual Planck spectrum, but its amplitude is increased by the value T_0 ; for $\nu > \nu_p$ the quantity $\delta\tilde{T}$ decreases very rapidly with increasing frequency, and for $\nu \gg \nu_p$ it then becomes equal to the standard value δT for the usual Planck spectrum. Fig 3.7 shows that even for small NP effects, $\nu_p < 206$ MHz, the spectral feature of the cosmological 21-cm background is altered. However, the physical processes taking place during these epochs will remain unaltered in the presence of NP effects on the CMB, but these effects have to be taken into account when recovering the history of the Universe during the DA and the EoR. Surprisingly, the 21-cm brightness temperature is increased for a CMB background modified by NP effects compared to the unmodified one. Consequently, this makes it relatively easier to detect the 21-cm emission, which allows the possibility to set constraints on both NP effects and on processes occurring during the EoR and the DA. Available limits from the PAPER experiment (Parsons et al. 2014) in the 100–200 MHz provide limits only on the average temperature brightness of $\langle T_b \rangle < 275$ and 291 mK for values of the ionization fraction $x_i = 0.5$ and $x_i = 0.75$ of the ionization power spectra respectively, which cannot be unfortunately directly compared to the predictions for the quantity δT used here. The next generation SKA and HERA low-frequency interferometers will have the possibility to improve the knowledge of the brightness temperature contrast δT down to levels of ~ 3 mK (~ 0.3 mK) with SKA-1 (SKA-2) at 3σ c.l. in about 1000 hrs at 150 MHz (Kopmans 2010) and possibly cover a wider frequency range, thus allowing us to set much stronger limits on ν_p from the spectrum of $\delta T(\nu)$.

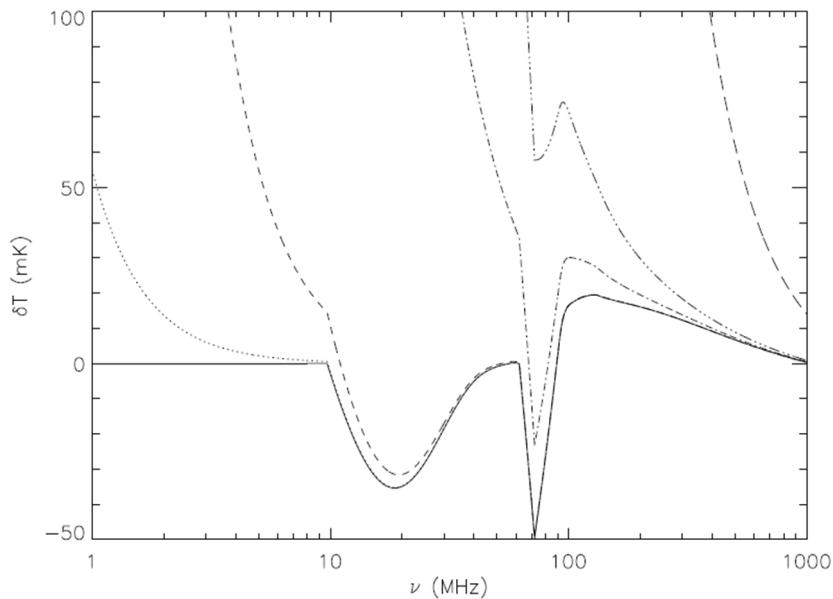


Figure 3.7: The change in brightness temperature $\delta\tilde{T}$ for $\nu_p = 0$ (solid line), $\nu_p = 0.2$ (dotted), 1 (dashed), 10 (dot-dashed), 20 (three dots-dashed) and 100 MHz (long dashed) as a function of the frequency (Colafrancesco et al. 2015a).

3.5 Discussions and conclusions

We have been able to perform a deep analysis of the influence of NP effects associated with a non-zero plasma frequency on cosmological radio backgrounds and we have been able to show the possible strategies that can be followed in order to put observational constraints on the effect. Upper limits of ν_p were derived from current available CMB measurements and the spectral impact of a non-zero plasma frequency has been demonstrated on three different observables: the CMB spectrum, the SZE and the cosmological 21-cm background.

The presence of NP effects will result in an intensity cut-off on the CMB spectrum at $\nu < 400$ MHz. Using current CMB data from *COBE-FIRAS* together with lower frequency measurements, we have been able to set upper limits on the plasma frequency $\nu_p = 206, 346$ and 418 MHz at 1, 2, 3 σ c.l., respectively. The difference between the pure Planck spectrum and the one modified by NP effects at low frequencies is of the order of mJy/arcmin² and this difference becomes less prominent at higher frequencies ($\nu \approx 150$ GHz) where it is of the order of 0.1 mJy/arcmin². These results indicate that the experimental route to probe NP effects in the early universe is to observe the cosmological radio background at very low frequencies.

In addition to that, we have also computed the spectrum of the SZE modified by NP effects, which demonstrates that in the presence of such effects, the spectrum of the SZE is altered and shows interesting features at low frequencies < 1 GHz. The spectrum of

SZE_{NP} has a peak that occurs at the plasma frequency which is independent of cluster parameters such as temperature, optical depth, minimum momentum p_1 and spectral index α . Therefore the SZE_{NP} provides us with a direct and unambiguous way of determining the plasma frequency by using large scale structures of the local Universe, which opens a new window for the exploration of plasma effects in the early universe. We have shown that the SKA-LOW and SKA-MID have the potential to observe such a signal integrating over the central regions ($\approx 5'$ radius) of high-temperature ($k_B T \sim 15$ keV) clusters.

Observing the SZE_{NP} also benefits from its differential nature thus being less affected by the large impact of large-scale foreground emission that is one of the main systematic biases that limits the study of the intensity spectrum of the cosmological background radiation. The SZE_{NP} has also the appealing property that we can study the presence of NP effects in the early universe by looking at very local cosmic structures for which the structural parameters are known with high accuracy. Finally, we mention that studies of NP effects through the SZE_{NP} can be done by intensive observations of only one galaxy cluster, or with a stacked spectrum of a few well known clusters, thus avoiding the need for large statistical studies of source populations or wide area surveys.

Finally, we have shown that future low-frequency observations of the cosmological 21-cm brightness temperature spectral change have the possibility to set global constraints on NP effects by constraining the spectral variations of $\delta\tilde{T}$ induced by the plasma frequency value at the epoch of recombination.

We discussed, in this context, that even moderate limits on the average brightness temperature of the 21-cm background obtained with SKA precursors, like e.g. the PAPER experiment, are able to start limiting the possible values of ν_p in its high-frequency domain (of order of 100 to a few hundreds MHz).

In conclusion, we have demonstrated that the study of the low-frequency cosmological radio background has a strong and unique potential for probing the physics of the early universe. This demonstration aligns such the idea of proving NP effects with previous studies of the photon decay effects in the early universe and on the study of the DA and EoR through the SZE-21cm, and indicates that this area of investigation of the fundamental physics of the universe will receive a boost with the next generation high-sensitivity radio telescopes like the SKA.

Chapter 4

Relativistic SZE polarization in cosmic structures

Great experimental opportunities are foreseen with upcoming instruments such as the SKA (Carilli 2008, Dewney 2012), which will be in operation in the frequency range 0.03 GHz up to 40 GHz and whose sensitivities are around nK level, the ground-based ALMA experiment (Carilli 2008), the space-borne *Millimetron* experiment (Rudnitskiy 2015), operating in the millimeter frequency range of 84-720 GHz and 100-1900 GHz respectively and the CORE++ space-borne survey experiment ¹; the combination of these experiments will provide a multifrequency spectral approach for detecting the SZE polarization signal. Given the coming experimental opportunities, it has become relevant to study the SZE polarization in depth, analyzing the possible astrophysical and cosmological aspects and their exploitation in the light of the achievable experimental sensitivities.

From a theoretical perspective, the calculation of SZE polarization in most previous works (Sazonov & Sunyaev 1999, Lavaux et al. 2004, Hall & Challinor 2014, Yasini & Pierpaoli 2016, Liu et al. 2016) have relied heavily on non-relativistic approximations and therefore, the results are only valid for thermal electrons of low temperature. Since observations of clusters have revealed that the temperature ICM of these structures can be up to ≈ 14 keV on average (up to 20 keV in some cluster regions) (Gomez et al. 2004, Reichert et al 2011, Wik et al. 2014), the results of these previous works are incomplete and give an incorrect spectral feature of the polarization spectrum of the SZE.

Furthermore, the detection of non-thermal emission (like, e.g., radio-halos) from galaxy clusters (Ferrari et al. 2008, Feretti 2012) and lobes of radio-galaxies also motivates for a full relativistic study of polarization in IC scattering processes. It is widely accepted that this non-thermal emission originates from a relativistic population of electrons spiraling around

¹[http://www.core-mission.org/documents/CoreProposal Final.pdf](http://www.core-mission.org/documents/CoreProposal%20Final.pdf)

magnetic field lines (Govoni & Ferretti 2004). These non-thermal electrons also contribute to the Comptonization of the CMB and hence an SZE polarization is also expected from them. Interestingly, one wants to know whether the SZE polarization is coming from the thermal or the non-thermal electrons and evaluate the non-thermal effect in comparison with the thermal one. The SZE spectrum in intensity produced by non-thermal electrons (shown in chapter 1) has been shown to extend from low to high frequencies (see e.g. Colafrancesco et al 2003, 2013), ≈ 1000 GHz. Evidently, it can be anticipated that the spectrum of the polarized component will also extend over a wide range of frequencies. Hence, this consequently presents an opportunity to search for the SZE polarization at frequencies 100 GHz up to 1000 GHz.

Matters become more complicated given that, occasionally, the non-thermal emission regions of galaxy clusters coincide with the X-ray emitting counterparts (Colafrancesco et al. 2003, 2011, Marchegiani & Colafrancesco 2015). In addition, it is also possible to have two or more thermal electron distributions, with different optical depth and temperature, co-existing together. In chapter 1, we have demonstrated how to compute the SZE intensity spectrum for a general combination of various electron populations. Application of this technique to the Bullet cluster have shown that the fit to the SZE data over a wide frequency range is better described by a combination of electron populations (Colafrancesco et al. 2011).

Although there are previous derivations of the SZE in a full relativistic way, they have been done for thermal electron distributions only and the solutions are presented as an expansion in terms of the temperature parameter, $\theta_e = kT_e/m_e c^2 \ll 1$ (Itoh et al. 1998, Challinor et al. 2000). Therefore, the restriction to thermal electrons is somehow incomplete and cannot be applied to general electron populations. A more complete treatment is needed which can describe any general electron population that is found in cosmic systems, and in particular the non-thermal ones that are present in the atmosphere of galaxy clusters and lobes/jets of radio-galaxies.

As mentioned previously, other multipoles of the CMB can induce polarization in addition to the quadrupole. By restricting to the non-relativistic limit, it has been shown that, for moving clusters (non-zero peculiar velocities), kinematic effects will induce dipole and octupole contributions to the SZE polarization (Yasini & Pierpaoli 2016). For non-moving clusters, the result shows that only the quadrupole contributes, which is expected when relativistic effects are absent. On the other hand, it has been shown that relativistic effects can be induce polarization in the SZE from higher order CMB multipoles (e.g. octupole) even if the cosmic structure is not moving with respect to the CMB frame (Challinor et al. 2000). However, the results are again restricted only to thermal electrons and are written in expanding terms of θ_e .

In this present work, we demonstrate explicitly, for non-moving structures, that when relativistic effects are accounted for, the SZE polarization shows contributions from the higher order multipoles of the CMB and that our results are applicable to any distribution of electrons, whether thermal or non-thermal.

To describe relativistic polarization in SZE, several authors (Itoh et al. 1998, Hansen & Lilje 1999, Challinor et al. 2000, Hall & Challinor 2014) have approached the problem using the Stokes parameters directly, by specifying a set of basis for each photon direction. Since SZE involves Comptonization, this method becomes very tedious and cumbersome (Portsmouth & Bertschinger 2004a). In this present work, we have opted for a simpler approach (Portsmouth & Bertschinger 2004a, 2004b) to describe polarization in SZE. It is actually based on an extension of a covariant formalism (Nozawa & Kohyama 2009, Nozawa et al. 2009) for computing the SZE by solving the relativistic Boltzmann equation, but this time written to accommodate polarization. This method allows the Stokes parameters to be transformed easily between frames of references and also allow the result to be written in a more elegant way (similar to Ensslin & Kaiser 2000, Colafrancesco et al. 2003, Nozawa & Kohyama 2009, Nozawa et al. 2009) and valid for any distribution of electrons. The anisotropy of the CMB is easily taken into account, thus allowing us to compute the contribution of the multipoles of the CMB in SZE polarization. Additionally, no extensive comparison with sensitivities of current or future instruments has been made so far while this is a relevant issue for the observability of this effect.

In this present work we compute the SZE polarization by solving the relativistic polarized Boltzmann equation (Portsmouth & Bertschinger 2004a, 2004b, Emritte et al. 2016) in the Thomson's limit. We extract the Stokes parameters and compute their spectrum for the quadrupole and the octupole of the CMB in the case of both thermal and non-thermal population of electrons. This approach also allows us to compute the polarization signal arising from a general combination of various electron populations. In order to assess the detectability of the signal, we also compute the expected signals for a real cluster like the Bullet cluster and compare it with the sensitivity of various instruments operating in different frequency bands.

4.1 The polarized Boltzmann equation

From now onwards we use the unit convention $c = 1$ and $\hbar = 1$ except where otherwise specified.

Without accounting for polarization, the Compton scattering process of a photon and an electron, $\gamma(\vec{p}_1) + e^-(\vec{q}_1) \rightarrow \gamma(\vec{p}_2) + e^-(\vec{q}_2)$, can be described in a full relativistic way through the covariant Boltzmann equation. In a given lab-frame, $V_L^\mu = [1, 0, 0, 0]$, this equation is given (Itoh et al. 1998, Nozawa et al. 2009) by:

$$\frac{df(\vec{p}_1)}{dt} = 2 \int d^3q_1 d^3q_2 d^3p_2 W \left[f(\vec{p}_2) g_e(\vec{q}_2) - f(\vec{p}_1) g_e(\vec{q}_1) \right], \quad (4.1)$$

where the functions f and g_e are general functions describing the momentum distribution of the photons and electrons respectively, and W is written as

$$W = \frac{3\sigma_T}{32\pi} m_e^2 \frac{X}{E_1 E_2 p_1 p_2} \delta^4(p_1^\mu + q_1^\mu - p_2^\mu - q_2^\mu) \quad (4.2)$$

$$X = m_e^2 \left(\frac{1}{k_2} - \frac{1}{k_1} \right)^2 + 2m_e \left(\frac{1}{k_1} - \frac{1}{k_2} \right) + \frac{1}{2} \left(\frac{k_1}{k_2} + \frac{k_2}{k_1} \right), \quad (4.3)$$

and k_1 and k_2 are defined as follows:

$$k_1 = -p_1^\mu V_{2\mu} \quad (4.4)$$

$$k_2 = -p_2^\mu V_{2\mu}. \quad (4.5)$$

The quantity $V_{2\mu}$ is the four-velocity of the electron after collision. In the rest-frame V_L , \vec{p}_1 and \vec{p}_2 represent the momentum of the photon before and after collision and \vec{q}_1 and \vec{q}_2 represent the momentum of the electron before and after collision, respectively. The 4-vectors in the delta function are represented as $p_1^\mu = (p_1, \vec{p}_1)$, $q_1^\mu = (E_1, \vec{q}_1)$, $p_2^\mu = (p_2, \vec{p}_2)$ and $q_2^\mu = (E_2, \vec{q}_2)$. The quantity k_i represents the magnitude of the momentum of the photon with 4-momentum p_i^μ in the rest frame of V_2 where $i = 1, 2$. The derivative d/dt is

$$\frac{d}{dt} = \frac{1}{p_1} p_1^\alpha \partial_\alpha. \quad (4.6)$$

For convenient reasons, the Boltzmann equation are often broken into two terms, i.e. "scattering in" and "scattering out" of the momentum element d^3p_1 , which can be written as follows:

$$\frac{df}{dt} = \left(\frac{df}{dt} \right)_{\text{in}} - \left(\frac{df}{dt} \right)_{\text{out}}. \quad (4.7)$$

The first term in this equation describes the rate of scattering of photons with momentum \vec{p}_2 off electrons with momentum \vec{q}_2 into d^3p_1 around \vec{p}_1 , while the second term represents the rate of scattering of photons with momentum \vec{p}_1 off electrons \vec{q}_1 into d^3p_2 around \vec{p}_2 . We should also point out that this equation neglects stimulated emission as well as Pauli blocking but is still valid outside the Thomson's regime where quantum effects are not negligible. Eq 4.1 neglects Fermi blocking and stimulated emission which is justified since the temperatures of the plasmas in cosmic structures are much less than the electron mass energy, $kT_e \ll m_e c^2$.

For polarization description in Compton scattering process, one uses the relativistic polarized Boltzmann equation which is a tensor generalization of eq. 4.1, where the cross-section and the distribution functions become tensor quantities (see Portsmouth & Bertschinger

2004a, 2004b). Neglecting Fermi blocking and stimulated emission, the equation (see Portsmouth & Bertschinger 2004a, 2004b) be written as follows:

$$\begin{aligned}
 p_1 \frac{df^{\mu\nu}}{dt}(p_1^m, V_L^m) &= m_e^2 \sigma_T \int \frac{d^3 q_1}{E_1} \frac{d^3 q_2}{E_2} \frac{d^3 p_2}{p_2} \delta^4(p_1^\mu + q_1^\mu - p_2^\mu - q_2^\mu) \\
 &\times P_{\alpha\beta}^{\mu\nu}(p_1^m, V_L^m) \left[\Phi_{\rho\sigma}^{\alpha\beta}(p_1^m, p_2^m, V_2^m) f^{\rho\sigma}(p_2^m, V_L^m) g_e(\vec{q}_2) \right. \\
 &\left. - \phi^{\alpha\beta}(p_1^m, V_L^m) g_{\gamma\delta} \Phi_{\rho,\sigma}^{\gamma\delta}(p_2^m, p_1^m, V_1^m) f^{\rho\sigma}(p_1^m, V_L^m) g_e(\vec{q}_1) \right], \tag{4.8}
 \end{aligned}$$

where $g_{\gamma\delta} = (-1, 1, 1, 1)$ is the metric tensor. Eq 4.8 is valid even outside the Thomson regime. In the lab frame, $V_L^\mu = [1, 0, 0, 0]$, an observer sees the velocity of the electrons to be V_1^m (before collision) and V_2^m (after collision). The polarization tensor for photons with momentum p_1^μ for this observer is denoted by $f^{\mu\nu}(p_1^m, V_L^m)$. The quantities V_1^m and V_2^m denote the 4-velocity of the electron before and after collision whose momentum is q_1^m and q_2^m , respectively, whereas p_1^m and p_2^m represent that of the photon before and after the interaction.

We clarify that writing the distribution function $f^{\mu\nu}(p^m, V^m)$ does not mean that f is a function of V^m , but is only a notation used to denote that f is the distribution function of the observer traveling with velocity V^m ; it also does not mean that we are evaluating $f^{\mu\nu}$ in his rest-frame. If one wants to obtain the distribution function in the rest-frame of the observer, one has to Lorentz-transform to the V frame in order to do so. So the function $f^{\mu\nu}(p^m, V^m) \rightarrow f^{\mu\nu}(p^0, \vec{p}, V^m) \rightarrow f^{\mu\nu}(\vec{p}, V^m)$ can be also written as $f^{\mu\nu}(\vec{p}, V^m)$. Also for the scalar function the following relationship $f(p^\mu) \rightarrow f(p^0, \vec{p}) \rightarrow f(\vec{p})$ holds. The reason why we can write it in terms of only 3-vectors is because $p^0 = |p|$ for the photon but it is also true for massive particles because $p^0 = \sqrt{p^2 + m^2}$. Eq. 4.8 can also be used to calculate the SZE polarization resulting from kinematic effects as well as from multiple scatterings effects. These two cases will be treated specifically in a forthcoming work.

The cross-section here becomes a tensor, as we mentioned previously, and is written as follows

$$\begin{aligned}
 \Phi_{mn}^{\mu\nu}[p_1^m, p_2^m, V_2^m] &\rightarrow \text{is the scattering cross-section for } (p_2^m, V_2^m) \rightarrow p_1^m \\
 \Phi_{mn}^{\mu\nu}[p_2^m, p_1^m, V_1^m] &\rightarrow \text{is the scattering cross-section for } (p_1^m, V_1^m) \rightarrow p_2^m. \tag{4.9}
 \end{aligned}$$

The term $\Phi_{mn}^{\mu\nu}$ is an analogue of X for the polarized case and is constructed out of projection tensors (Portsmouth & Bertschinger 2004a, 2004b). The tensor $\phi^{\mu\nu}$ represents the normalized polarization tensor written as $f^{\mu\nu}/f$. Finally we have $P_{\alpha\beta}^{\mu\nu}$ which is constructed out of the projection tensors as follows:

$$P_{\alpha\beta}^{\mu\nu}(p^m, V^m) = P_\alpha^\mu(p^m, V^m) P_\beta^\nu(p^m, V^m). \tag{4.10}$$

These terms $P_{\alpha\beta}^{\mu\nu}(p_1^m, V_L^m)$ are projection tensors and project the terms in the right hand side of the polarized Boltzmann equation into the plane perpendicular to the photon with momentum p_1^m and 4-velocity of the observer V_L^m . In the rest frame of the observer V_L^m the projection tensor has only spatial components (see an illustrative example in Portsmouth & Bertschinger 2004a, 2004b).

The cross-section term is written in terms of the projection tensors in the Thomson approximation as

$$\Phi_{\gamma\delta}^{\mu\nu}(p_2^m, p_1^m, V_1^m) = \frac{3}{8\pi} P_{\alpha\beta}^{\mu\nu}(p_2^m, V_1^m) P_{\gamma\delta}^{\alpha\beta}(p_1^m, V_1^m). \quad (4.11)$$

The $\delta^4(p_1^\mu + q_1^\mu - p_2^\mu - q_2^\mu)$ can be integrated out by using the following relation:

$$\frac{d^3 q_1}{E_1} = d^4 q_1^\mu \delta\left[\frac{1}{2}(q_1^\mu q_{1\mu} + m_e^2)\right]. \quad (4.12)$$

We also write the electron distribution function as $g_e(\vec{q}) = n_e f_e(\vec{q})$ where n_e is the electron number density. We can also use the definition of optical depth, $d\tau_e = n_e \sigma_T dt$, to get rid of the Thomson total cross-section.

The conservation of four-momentum equation is written as

$$q_1^m = q_2^m + p_2^m - p_1^m. \quad (4.13)$$

This acts as a constraint on q_1^m , and the delta function in eq. 4.12 can be simplified to

$$\delta\left[\frac{1}{2}(q_1^m q_{1m} + m_e^2)\right] = \delta[m_e(k_1 - (k_2 + R_{12}))]. \quad (4.14)$$

We have also introduced a new variable, $R_{12} = p_1^\mu p_{2\mu}/m_e$, which will be very useful for our following calculations.

Using all these simplifications we can now cast the Boltzmann polarized equation as follows

$$\begin{aligned} p_1 \frac{\partial}{\partial \tau} f^{\mu\nu}(p_1^m, V_L^m) &= m_e^2 \int \frac{d^3 q_2}{E_2} \frac{d^3 p_2}{p_2} \delta[m_e(k_1 - (k_2 + R_{12}))] \\ &\quad \times P_{\alpha\beta}^{\mu\nu}(p_1^m, V_L^m) \left[\Phi_{\rho\sigma}^{\alpha\beta}(p_1^m, p_2^m, V_2^m) f^{\rho\sigma}(p_2^m, V_L^m) f_e(\vec{q}_2) \right. \\ &\quad \left. - \phi^{\alpha\beta}(p_1^m, V_L^m) g_{\gamma\delta} \Phi_{\rho\sigma}^{\gamma\delta}(p_2^m, p_1^m, V_1^m) f^{\rho\sigma}(p_1^m, V_L^m) f_e(\vec{q}_1) \right]. \end{aligned} \quad (4.15)$$

4.1.1 The distribution function in the Thomson approximation

Starting from eq. 4.15, we will derive the Stokes parameters of the scattered CMB radiation by an electron gas. In order to reach this goal, we will rely on three important assumptions which are completely valid to describe the interaction between photons and electrons producing the SZE. These assumptions are:

1) Single Scattering approximation: this means that we assume that each photon is scattered once by the electrons. This is valid in the optically thin regime for the study of galaxy clusters (e.g $\tau \approx 0.01$) and radio-galaxies (e.g $\tau \approx 1 \times 10^{-4}$).

2) Thomson cross-section: this assumption means that energy transfers and quantum effects are neglected, and in this way the scattering in the electron rest-frame can easily be described by Thomson scattering, which in turn simplifies the cross-section term. This is valid because the CMB photons are mostly found in the low frequency range of the electromagnetic spectrum, meaning that they are less energetic than the electrons residing in the cosmic structures we are interested in. This approximation is valid for electrons with Lorentz factor less than $\gamma \sim 10^7$ (see, e.g. Fargion & Salis 1998, Birkinshaw 1999).

3) Unpolarized incident CMB: what we mean by this assumption is that before scattering the CMB is completely unpolarized; even though this is not completely true, for most of our calculations it is a quite reasonable simplification because the degree of polarization of the CMB before collision is very small (Hu 2003, Kovac et al. 2002, Page et al. 2007).

Under these assumptions, the polarized Boltzman equation can be simplified extensively. In addition to these assumptions we also make a small change in our notation, mainly $q_2 \rightarrow q_e$ and also $V_2 \rightarrow V_e$.

For single scattering between CMB photons and electrons, the equation becomes

$$\begin{aligned}
 p_1 \frac{\partial}{\partial \tau} f^{\mu\nu}(p_1^m, V_L^m) &= m_e \int \frac{d^3 q_e}{\gamma_e} \frac{d^3 p_2}{p_2} \delta[m_e(k_1 - (k_2 + R_{12}))] \\
 &\times P_{\alpha\beta}^{\mu\nu}(p_1^m, V_L^m) \left[\Phi_{\rho\sigma}^{\alpha\beta}(p_1^m, p_2^m, V_e^m) f^{\rho\sigma}(p_2^m, V_L^m) f_e(\vec{q}_e) \right. \\
 &\left. - \phi^{\alpha\beta}(p_1^m, V_L^m) g_{\gamma\delta} \Phi_{\rho\sigma}^{\gamma\delta}(p_2^m, p_1^m, V_1^m) f^{\rho\sigma}(p_1^m, V_L^m) f_e(\vec{q}_1) \right].
 \end{aligned} \tag{4.16}$$

Now we make use of our second assumption, i.e. the Thomson limit,

$$\begin{aligned}
 \gamma_e \alpha_2 &\ll 1 \\
 \alpha_2 &= \frac{p_2}{m_e}.
 \end{aligned} \tag{4.17}$$

We also use the cross-section that we introduced in the previous section written as

$$\Phi_{\gamma\delta}^{\mu\nu}(p_k^m, p_i^m, V_i^m) = \frac{3}{8\pi} P_{\alpha\beta}^{\mu\nu}(p_k^m, V_i^m) P_{\gamma\delta}^{\alpha\beta}(p_i^m, V_i^m). \tag{4.18}$$

Note that the projection tensors which project the distribution function perpendicular to V_i^m and p_i^m (where $k, i = 1, 2$) are included in this cross-section term. Then we define the

following useful variables

$$\begin{aligned}
 n_{12} &= \frac{k_1}{p_1} = \gamma_e (1 - \vec{\beta}_e \cdot \hat{n}_1) \\
 n_{22} &= \frac{k_2}{p_2} = \gamma_e (1 - \vec{\beta}_e \cdot \hat{n}_2) \\
 r_{12} &= \frac{p_1^\mu p_{1\mu}}{p_1 p_2} = m_e R_{12} = \hat{n}_1 \cdot \hat{n}_2 - 1 \\
 \alpha_j &= \frac{p_j}{m_e}
 \end{aligned} \tag{4.19}$$

where \hat{n}_1 and \hat{n}_2 are unit vectors in the direction of \vec{p}_1 and \vec{p}_2 and $\vec{\beta}_e$ is the electron velocity. The delta function $\delta[m_e(k_1 - (k_2 + R_{12}))]$ can be further simplified by using the Thomson limit as follows:

$$\begin{aligned}
 m_e [k_1 - (k_2 + R_{12})] &= -m_e^2 n_{22} \left[\alpha_2 - \alpha_1 \frac{n_{12}}{n_{22}} \left(1 - \alpha_2 \frac{r_{12}}{n_{12}} \right) \right] \\
 &= -m_e^2 n_{22} \left[\alpha_2 - \alpha_1 \frac{n_{12}}{n_{22}} \left(1 - O(\alpha_2 \gamma_e) \right) \right] \\
 &= -m_e^2 n_{22} \left[\alpha_2 - \alpha_1 \frac{n_{12}}{n_{22}} \right].
 \end{aligned} \tag{4.20}$$

In order to arrive at the previous approximation we made use of the following inequality:

$$\alpha_2 \left| \frac{r_{12}}{n_{12}} \right| \leq \frac{2\alpha_2}{\gamma_e (1 - \beta_e)} = 2\alpha_2 (1 + \beta_e) \gamma_e \leq 4\gamma_e \alpha_2 = O(\gamma_e \alpha_2). \tag{4.21}$$

In the Thomson limit, and in the rest frame of the electrons, the magnitude of the momentum of the photon before and after collision is the same, hence $k_1 \approx k_2$, and therefore the variable p_2 is restricted by the following condition:

$$p_2 = \frac{n_{12}}{n_{22}} p_1. \tag{4.22}$$

Another simplification can be made by noticing that

$$\gamma_1 = \gamma_e [1 + O(\alpha_2 \gamma_e)]. \tag{4.23}$$

This can be achieved by putting $m = 0$ in the equation $q_1^m = q_2^m + p_2^m - p_1^m$. Using $\alpha_1 = (n_{22}/n_{12}) \alpha_2$ we obtain

$$\gamma_1 = \gamma_e + \alpha_2 \left[1 - \frac{n_{22}}{n_{12}} \right]. \tag{4.24}$$

Then one can show that:

$$\begin{aligned}
 \gamma_1 &= \gamma_e \left(1 + \frac{\alpha_2}{\gamma_e} \left(1 - \frac{n_{22}}{n_{12}} \right) \right) \leq \\
 &\leq \gamma_e \left(1 + \frac{\alpha_2}{\gamma_e} \left| 1 - \frac{n_{22}}{n_{12}} \right| \right) = \\
 &= \gamma_e \left[1 + 2\beta_e \alpha_2 (1 + \beta_e) \gamma_e \right] \leq \\
 &\leq \gamma_e \left[1 + 4\alpha_2 \gamma_e \right] = \\
 &= \gamma_e \left[1 + O(\alpha_2 \gamma_e) \right].
 \end{aligned} \tag{4.25}$$

To arrive at the result we use the following inequalities:

$$\begin{aligned}
 \left| \alpha_2 \left(1 - \frac{n_{22}}{n_{12}} \right) \right| &\leq \left| \alpha_2 \left[1 - \frac{1 + \beta_e}{1 - \beta_e} \right] \right| = \\
 &= \alpha_2 \left| \frac{-2\beta_e}{1 - \beta_e} \right| = \\
 &= 2\beta_e \alpha_2 (1 + \beta_e) \gamma_e^2 \leq \\
 &\leq 4\alpha_2 \gamma_e^2.
 \end{aligned} \tag{4.26}$$

From eq. 4.25, the energy of the electrons is unaltered during the Thomson scattering, hence also the distribution function

$$f_e(\vec{q}_1) \approx f_e(\vec{q}_e). \tag{4.27}$$

Using these simplifications we arrive at the following expression:

$$\begin{aligned}
 \frac{\partial}{\partial \tau} f^{\mu\nu}(p_1^m, V_L^m) &= \frac{3}{8\pi} \int \frac{d^3 q_e}{\gamma_e} \int d\Omega_2 \frac{n_{12}}{n_{22}^2} f_e(\vec{q}_e) \\
 &\times \left[J_\alpha^\mu(p_1^m, V_e^m, V_L^m) J_\beta^\nu(p_1^m, V_e^m, V_L^m) f^{\alpha\beta}(p_2^m, V_e^m) \right. \\
 &\left. - \phi^{\mu\nu}(p_1^m, V_L^m) P_{\alpha\beta}(p_2^m, V_1^m) f^{\alpha\beta}(p_1^m, V_1^m) \right],
 \end{aligned} \tag{4.28}$$

with

$$J_\alpha^\mu(p_1^m, V_e^m, V_L^m) = P_\beta^\mu(p_1^m, V_L^m) P_\alpha^\beta(p_1^m, V_e^m). \tag{4.29}$$

Now we make use of the third assumption which is that the CMB is unpolarized prior to the scattering by the electrons. With this assumption one can make the following replacements

$$f^{\mu\nu}(p^m, V^m) = \frac{1}{2} f(p^m) P^{\mu\nu}(p^m, V^m) \tag{4.30}$$

$$\phi^{\mu\nu}(p^m, V^m) = \frac{1}{2} P^{\mu\nu}(p^m, V^m). \tag{4.31}$$

Finally eq. 4.28 can be written as follows:

$$\begin{aligned}
 \frac{\partial}{\partial \tau} f^{\mu\nu}(p_1^m, V_L^m) &= \frac{3}{16\pi} \int \frac{d^3 q_e}{\gamma_e} \int d\Omega_2 \frac{n_{12}}{n_{22}^2} f_e(\vec{q}_e) \\
 &\times \left[\left[P^{\mu\nu}(p_1^m, V_L^m) - L^\mu L^\nu(p_1^m, p_2^m, V_e^m) \right] f(p_2^m) \right. \\
 &\left. - P^{\mu\nu}(p_1^m, V_L^m) \left[1 + \eta_{12} \left(1 + \frac{1}{2} \eta_{12} \right) \right] f(p_1^m) \right],
 \end{aligned} \tag{4.32}$$

where we define

$$\begin{aligned}
 L^\mu(p_1^m, p_2^m, V_e^m) &= \frac{1}{n_{22}} \left[\frac{p_2^\mu}{p_2} - \left(1 + \gamma_e \frac{r_{12}}{n_{12}} \right) \frac{p_1^\mu}{p_1} + \frac{r_{12}}{n_{12}} V_e^\mu \right] \\
 \eta_{12} &= \frac{r_{12}}{n_{12} n_{22}} \\
 L^\mu L_\mu &= -2\eta_{12} \left(1 + \frac{1}{2}\eta_{12} \right). \tag{4.33}
 \end{aligned}$$

In these last equations we recall that p_1^μ or p_2^μ is the momentum in the frame $V_L^\mu = [1, 0, 0, 0]$ and from this position we can write that $p_k = -p_k^\mu V_{L\mu}$. Since we are using $c = 1$ and $h = 1$, then p_1 and ν_1 can be interchanged at will.

4.1.2 Stokes parameters

In this section, we demonstrate here how the Stokes parameters are derived from the tensor $f^{\mu\nu}(p_1^m, V_L^m)$. We first derive the first Stokes parameter I which is given by:

$$\begin{aligned}
 \frac{\partial}{\partial \tau} I(\vec{p}_1) = p_1^3 \frac{d}{d\tau} f_\mu^\mu(\vec{p}_1) &= \frac{3p_1^3}{8\pi} \int \frac{d^3 q_e}{\gamma_e} \int d\Omega_2 \frac{n_{12}}{n_{22}^2} f_e(\vec{q}_e) \\
 &\times \left[1 + \eta_{12} \left(1 + \frac{\eta_{12}}{2} \right) \right] [f(\vec{p}_2) - f(\vec{p}_1)], \tag{4.34}
 \end{aligned}$$

where we have used the notation $f(p^\mu) = f(\vec{p})$ as discussed above, and the fact that $I = p^3 f$ which is the relation between the distribution function of photons to the intensity. In order to determine the other Stokes parameters, namely Q and U , the choice of basis matters here, and depending on how the basis is chosen, will determine the simplicity of the calculation (Portsmouth & Bertschinger 2004a, 2004b).

In our case we choose a system of basis perpendicular to the observed radiation by fixing our Z-axis to be along the direction of the observed radiation. In this way the tensor $f^{\mu\nu}(\vec{p}_1)$ can be written as follows:

$$f^{\mu\nu}(\vec{p}_1) = \frac{1}{2p_1^3} \begin{bmatrix} 0 & 0 & 0 & 0 \\ 0 & I(\vec{p}_1) + Q(\vec{p}_1) & U(\vec{p}_1) + iV(\vec{p}_1) & 0 \\ 0 & U(\vec{p}_1) - iV(\vec{p}_1) & I(\vec{p}_1) - Q(\vec{p}_1) & 0 \\ 0 & 0 & 0 & 0 \end{bmatrix}. \tag{4.35}$$

We then extract the Stokes parameters from this matrix as follows:

$$\frac{d}{d\tau} Q(\nu_1) = \nu_1^3 \frac{d}{d\tau} [f^{11}(\nu_1) - f^{22}(\nu_1)] \tag{4.36}$$

$$\frac{d}{d\tau} U(\nu_1) = \nu_1^3 \frac{d}{d\tau} [f^{12}(\nu_1) + f^{21}(\nu_1)]. \tag{4.37}$$

In this coordinate system, the following variables take the form:

$$p_1^\mu = p_1(1, 0, 0, 1) \quad (4.38)$$

$$r_{12} = \cos \theta_2 - 1 \quad (4.39)$$

$$n_{12} = \gamma_e [1 - \beta_e \cos \theta_e] \quad (4.40)$$

$$n_{22} = \gamma_e \left[1 - \beta_e [\cos \theta_2 \cos \theta_e + \sin \theta_2 \sin \theta_e \cos(\phi_2 - \phi_e)] \right], \quad (4.41)$$

and also

$$V_e^\mu = \gamma_e \left[1, \beta_e \cos \phi_e \sin \theta_e, \beta_e \sin \phi_e \sin \theta_e, \beta_e \cos \theta_e \right] \quad (4.42)$$

$$p_2^\mu = p_2 \left[1, \cos \phi_2 \sin \theta_2, \sin \phi_2 \sin \theta_2, \cos \theta_2 \right]. \quad (4.43)$$

The Stokes parameters Q and U are then written as follows:

$$\begin{aligned} \frac{\partial Q}{\partial \tau}(\nu_1) &= -\frac{3}{16\pi} \int \frac{d^3 q_e}{\gamma_e} \int d\Omega_2 \frac{I(\nu_2, \hat{n}_2)}{n_{12}^4 n_{22}} f_e(\vec{q}_e) \\ &\times [\cos 2\phi_2 \sin^2 \theta_2 n_{12}^2 + 2 \cos(\phi_2 + \phi_e) \sin \theta_2 \sin \theta_e n_{12} r_{12} \gamma_e \beta_e \\ &+ \cos 2\phi_e \sin^2 \theta_e r_{12}^2 \beta_e^2 \gamma_e^2] \end{aligned} \quad (4.44)$$

$$\begin{aligned} \frac{\partial U}{\partial \tau}(\nu_1) &= -\frac{3}{16\pi} \int \frac{d^3 q_e}{\gamma_e} \int d\Omega_2 \frac{I(\nu_2, \hat{n}_2)}{n_{12}^4 n_{22}} f_e(\vec{q}_e) \\ &\times [\sin 2\phi_2 \sin^2 \theta_2 n_{12}^2 + 2 \sin(\phi_2 + \phi_e) \sin \theta_2 \sin \theta_e n_{12} r_{12} \gamma_e \beta_e \\ &+ \sin 2\phi_e \sin^2 \theta_e r_{12}^2 \beta_e^2 \gamma_e^2]. \end{aligned} \quad (4.45)$$

These 5-dimensional integrals can be evaluated by breaking them into five 1-dimensional integrals. We will compute them first for the intensity, and this will demonstrate the consistency of our results with the usual approach of computing the unpolarized SZE spectrum.

4.1.3 The Stokes parameter I

We derive here the Stokes parameter, I , for an isotropic CMB to show the consistency of our approach.

We define the variables, $\mu_e = \cos \theta_e$, $\mu_2 = \cos \theta_2$ and $\phi_0 = \phi_2 - \phi_e$. With these new variables eq. 4.34 takes the following form:

$$\begin{aligned} \frac{\partial f}{\partial \tau}(\nu_1) &= \frac{3}{32\pi^2} \int_0^1 d\beta_e \int_{-1}^1 d\mu_e \int_0^{2\pi} d\phi_e \int_{-1}^1 d\mu_2 \int_0^{2\pi} d\phi_0 \frac{n_{12} f_e(\beta_e)}{\gamma_e n_{22}^2} \\ &\times \left[1 + \eta_{12} \left(1 + \frac{\eta_{12}}{2} \right) \right] [f(\nu_2) - f(\nu_1)]. \end{aligned} \quad (4.46)$$

In order to evaluate the integrals above, we assume that in the lab frame, the electron plasma appears isotropic and hence the distribution function of the electrons becomes independent of direction and can be written in terms of β_e as follows

$$\frac{1}{4\pi} f_e(\beta_e) d\beta_e = f_e(\vec{q}_e) q_e^2 dq_e, \quad (4.47)$$

and use the fact that for a generic function $\Psi(\phi_e, \phi_2 - \phi_e)$,

$$\int_0^{2\pi} \int_0^{2\pi} \Psi(\phi_e, \phi_2 - \phi_e) d\phi_2 d\phi_e = \int_0^{2\pi} \int_0^{2\pi} \Psi(\phi_e, \phi_0) d\phi_0 d\phi_e. \quad (4.48)$$

In order to further simplify eq. 4.46 we also introduce another variable:

$$\chi_0 = \cos \phi_0, \quad (4.49)$$

and if we consider a general function $F(\cos \phi_0, \sin \phi_0)$ which has trigonometric functions as its argument, then we can write

$$\begin{aligned} \int_0^{2\pi} F(\cos \phi_0, \sin \phi_0) d\phi_0 &= \int_{-1}^1 \left[F(\cos \phi_0 \rightarrow \chi_0, \sin \phi_0 \rightarrow \sqrt{1 - \chi_0^2}) \right. \\ &\quad \left. + F(\cos \phi_0 \rightarrow \chi_0, \sin \phi_0 \rightarrow -\sqrt{1 - \chi_0^2}) \right] \frac{d\chi_0}{\sqrt{1 - \chi_0^2}}. \end{aligned} \quad (4.50)$$

By using the simplifications of eq. 4.48 and 4.50 and integrating eq 4.46 over ϕ_e we obtain:

$$\begin{aligned} \frac{\partial f}{\partial \tau}(\nu_1) &= \frac{3}{16\pi} \int_0^1 d\beta_e \int_{-1}^1 d\mu_e \int_{-1}^1 d\mu_2 \int_{-1}^1 d\chi_0 f_e(\beta_e) \\ &\quad \times \frac{2n_{12}^2 n_{22}^2 + 2n_{12} n_{22} (\mu_2 - 1) + (\mu_2 - 1)^2}{n_{12} n_{22}^4 \gamma_e \sqrt{1 - \chi_0^2}} [f(\nu_2) - f(\nu_1)]. \end{aligned} \quad (4.51)$$

At this stage we can perform a check that the Stokes parameter, I , derived from the polarized covariant Boltzmann equation gives the same result as that of the SZE intensity (eq 1.22) by making a transformation into the electron frame (Nozawa & Kohyama 2009) using the following variables:

$$\begin{aligned} \mu_0 &= \frac{\mu_2 - 1}{n_{12} n_{22}} + 1 \\ \mu &= \frac{\gamma_e n_{12} - 1}{n_{12} \gamma_e \beta_e} \\ \mu' &= \frac{\gamma_e n_{22} - 1}{n_{22} \gamma_e \beta_e}. \end{aligned} \quad (4.52)$$

By doing that, we obtain an equation in terms of the new variables of the following form:

$$\begin{aligned} \frac{\partial f}{\partial \tau}(\nu_1) &= \frac{3}{16\pi} \int d\beta_e \int d\mu \int d\mu' \int d\mu_0 [f(\nu_2) - f(\nu_1)] f_e(\beta_e) \\ &\quad \times \frac{1 + \mu_0^2}{\gamma_e^4 (1 - \beta_e \mu)^3 \sqrt{1 - \mu_0^2 - \mu^2 - \mu'^2 + 2\mu_0 \mu \mu'}}, \end{aligned} \quad (4.53)$$

with

$$\begin{aligned} \mu_{0,min} &= \mu\mu' - \sqrt{(1 - \mu^2)(1 - \mu'^2)} \\ \mu_{0,max} &= \mu\mu' + \sqrt{(1 - \mu^2)(1 - \mu'^2)}. \end{aligned} \quad (4.54)$$

The integration over μ_0 can be done easily and then introducing a last variable, which is related to the frequency shift

$$e^s = \frac{1 - \beta_e \mu'}{1 - \beta_e \mu} \quad (4.55)$$

$$s = \ln(\nu_2/\nu_1).$$

Eq. 4.53 can be casted into the usual form as in eq 1.22 as follows

$$\frac{\partial f}{\partial \tau}(\nu_1) = \int_{-\infty}^{\infty} P_1(s) [f(e^s \nu_1) - f(\nu_1)] ds, \quad (4.56)$$

where

$$\begin{aligned} P_1(s) &= \int_{\sinh \frac{|s|}{2}}^1 f_e(p_e) P(s, p_e) dp_e \\ P(s, \beta_e) &= \frac{3 e^s}{32} \int_{\mu_{min}}^{\mu_{max}} \frac{(3 - \mu^2) \beta_e^2 - (1 - 3\mu^2) [1 - e^s (1 - \mu \beta_e)]}{\beta_e^3 \gamma_e^4 (1 - \beta_e \mu)^2} d\mu. \end{aligned} \quad (4.57)$$

The electron distribution function has been written in terms of the electron momentum p_e and the function $P(s, p_e)$ is just the function $P(s, \beta_e)$ with the β_e and γ_e substituted in terms of p_e . This is given by

$$\begin{aligned} \gamma_e &= \sqrt{1 + p_e^2} \\ \beta_e &= \frac{p_e}{\sqrt{1 + p_e^2}}. \end{aligned} \quad (4.58)$$

This demonstrates, comfortably, that our derivation is consistent with the usual computation of the SZE in intensity (same as in eq. 1.22). Now, we can derive the Stokes parameters for the case where the CMB is anisotropic.

4.1.4 Anisotropic incident CMB radiation

The rate of change of the distribution function can be broken down into two terms

$$\frac{\partial f}{\partial \tau}(\nu_1, \hat{z}) = \frac{\partial f}{\partial \tau} \Big|_{\text{in}}(\nu_1, \hat{z}) - \frac{\partial f}{\partial \tau} \Big|_{\text{out}}(\nu_1, \hat{z}). \quad (4.59)$$

The rate of "scattering out" can easily be integrated (right-hand side of eq. 4.51 given the fact that $P_1(s)$ is normalized to one) and the result is:

$$\begin{aligned} \frac{\partial f}{\partial \tau}(\nu_1, \hat{z}) &= \frac{3}{16\pi} \int_0^1 d\beta_e \int_{-1}^1 d\mu_e \int_{-1}^1 d\mu_2 \int_{-1}^1 d\chi_0 f_e(\beta_e) \\ &\times \frac{2n_{12}^2 n_{22}^2 + 2n_{12} n_{22} (\mu_2 - 1) + (\mu_2 - 1)^2}{n_{12} n_{22}^4 \gamma_e \sqrt{1 - \chi_0^2}} f(\nu_1, \hat{z}) \\ &= \int_{-\infty}^{\infty} P_1(s) f(\nu_1, \hat{z}) ds = 1 \end{aligned} \quad (4.60)$$

To determine the "scattering in" we expand the distribution function in a spherical harmonic series as follows:

$$f(\nu_1, \hat{n}) = \sum_{l=0}^{\infty} \sum_{m=-l}^l f_{l,m}(\nu) Y_{l,m}(\cos \theta, \phi) \quad (4.61)$$

$$Y_{l,m}(\cos \theta, \phi) = \sqrt{\frac{2l+1}{4\pi} \frac{(l-1)!}{(l+m)!}} P_l^m(\cos \theta) e^{im\phi}. \quad (4.62)$$

Inserting the expanded distribution function into eq. 4.51 and for the "scattering in" term we obtain:

$$\begin{aligned} \left. \frac{\partial f}{\partial \tau}(\nu_1, \hat{z}) \right|_{\text{in}} &= \frac{3}{32\pi^2} \sum_{l=0}^{\infty} \sum_{m=-l}^l \int d\beta_e d\mu_e d\phi_e \int d\mu_2 d\phi_0 \frac{n_{12} f_e(\beta_e)}{n_{22}^2 \gamma_e} \\ &\times \left[1 + \eta_{12} \left(1 + \frac{\eta_{12}}{2} \right) \right] f_{l,m}(\nu_2) \sqrt{\frac{2l+1}{4\pi}} \\ &\times \frac{(l-m)!}{(l+m)!} P_l^m(\mu_2) e^{im(\phi_0 + \phi_e)} \\ &= \frac{3}{16\pi} \sum_{l=0}^{\infty} \sqrt{\frac{2l+1}{4\pi}} \int d\beta_e d\mu_e \int d\mu_2 d\chi_0 f_e(\beta_e) \\ &\times \frac{2n_{12}^2 n_{22}^2 + 2n_{12} n_{22} (\mu_2 + 1) + (\mu_2 + 1)^2}{n_{12} n_{22}^4 \gamma_e \sqrt{1 - \chi_0^2}} f_{l,0}(\nu_2) P_l^0(\mu_2). \end{aligned} \quad (4.63)$$

The integration over ϕ_e eliminates all the terms in $m \neq 0$. One can adopt an approach similar to the previous one by using the variables introduced in eq. 4.53, but we will use another set of variables introduced as follows:

$$\begin{aligned} s &= \ln \left(\frac{n_{12}}{n_{22}} \right) \\ t &= \ln (n_{12} n_{22}) \\ \mu_0 &= \frac{\mu_2 - 1}{n_{12} n_{22}} + 1. \end{aligned} \quad (4.64)$$

Substituting these variables into eq. 4.63 and subtracting the "scattering out" term (see eq. 4.60), we obtain a set of equations similar to eq. 4.56

$$\begin{aligned} \frac{\partial f}{\partial \tau}(\nu_1, \hat{z}) &= \sum_{l=0}^{l=\infty} \int_{-\infty}^{\infty} P_{l,0}(s) f_{l,0}(e^s \nu_1) ds - f(\nu_1, \hat{z}) \\ P_{l,0}(s) &= \int_{\sinh \frac{|s|}{2}}^1 f_e(p_e) P_{l,0}(s, p_e) dp_e \\ P_{l,0}(s, \beta_e) &= -\frac{3}{64\pi} \sqrt{\frac{2l+1}{\pi}} \frac{e^{\frac{3s}{2}}}{\gamma_e^3 \beta_e^2} \int_{-t_0}^{t_0} e^{\frac{t}{2}} dt \int_{A-B}^{A+B} \frac{1 + \mu_0^2}{\sqrt{B^2 - (A - \mu_0)^2}} \\ &\times P_l^0(e^t(\mu_0 - 1) + 1) d\mu_0, \end{aligned} \quad (4.65)$$

where

$$\begin{aligned}
 t_0 &= |s| - \ln \left(\frac{1 + \beta_e}{1 - \beta_e} \right) \\
 A &= \frac{e^{-t}}{\gamma_e^2 \beta_e^2} \left[1 + \gamma_e^2 e^t - 2\gamma_e e^{\frac{t}{2}} \cosh \frac{s}{2} \right] \\
 B &= 2 \frac{e^{\frac{t}{2}}}{\gamma_e^2 \beta_e^2} \sqrt{\left[\cosh \left(\frac{s-t}{2} \right) - \gamma_e \right] \left[\cosh \left(\frac{s+t}{2} \right) - \gamma_e \right]}.
 \end{aligned} \tag{4.66}$$

The function $P_{l,0}(s, p_e)$ is just the function $P_{l,0}(s, \beta_e)$ with the β_e substituted in terms of p_e as well as γ_e . One can see here that to each value of l one can associate a scattering kernel or a redistribution function $P_{l,0}(s)$. The scattering kernel associated with the monopole term is actually related to the scattering kernel for the isotropic case as follows:

$$P_{0,0}(s) = \frac{1}{\sqrt{4\pi}} P_1(s). \tag{4.67}$$

The scattering kernels for each l value conserve the property written as follows:

$$P_{l,0}(-s) = e^{-3s} P_{l,0}(s). \tag{4.68}$$

The change in the intensity for each value of l can then be computed as follows:

$$\begin{aligned}
 \frac{\partial I}{\partial \tau}(x, \hat{z}) &= \sum_{l=0}^{\infty} \int_{-\infty}^{\infty} P_{l,0}(s) I_{l,0}(e^{-s} x) ds - I(x, \hat{z}) \\
 &= \sum_{l=0}^{\infty} \left[\int_{-\infty}^{\infty} P_{l,0}(s) I_{l,0}(e^{-s} x) ds - \sqrt{\frac{2l+1}{4\pi}} I_{l,0}(x) \right],
 \end{aligned} \tag{4.69}$$

where

$$\begin{aligned}
 I(x, \theta, \phi) &= \sum_{l=0}^{\infty} \sum_{m=-l}^l I_{l,m}(x) Y_{l,m}(\theta, \phi) \\
 &= 2(kT_0)^3 \left[\frac{x^3}{e^x - 1} + \frac{e^x x^4}{(e^x - 1)^2} \sum_{l=2}^{\infty} \sum_{m=-l}^l a_{l,m} Y_{l,m}(\theta, \phi) \right].
 \end{aligned} \tag{4.70}$$

In eq. 4.69 we have used the relation

$$P_l^0(1) = 1. \tag{4.71}$$

We point out here that the function $P_{l,0}(s)$ is the same function obtained in a previous work (Chluba & Dai 2014). Note that eq. 4.69 describes the unpolarized SZE for the case of an anisotropic incident CMB and therefore implies that higher order multipoles can also contribute to the SZE intensity spectral distortion. If one adopts the variables in eq 4.55 instead of 4.65, the function $P_{l,0}(s, p_e)$ shows the same form as derived in the previous work when integrated over μ_0 .

Fig. 4.1 shows the scattering kernel, $P_{l,m}(s)$, for a thermal electron distribution for different temperatures. Our result is the same as the one obtained in Chluba & Dai 2014,

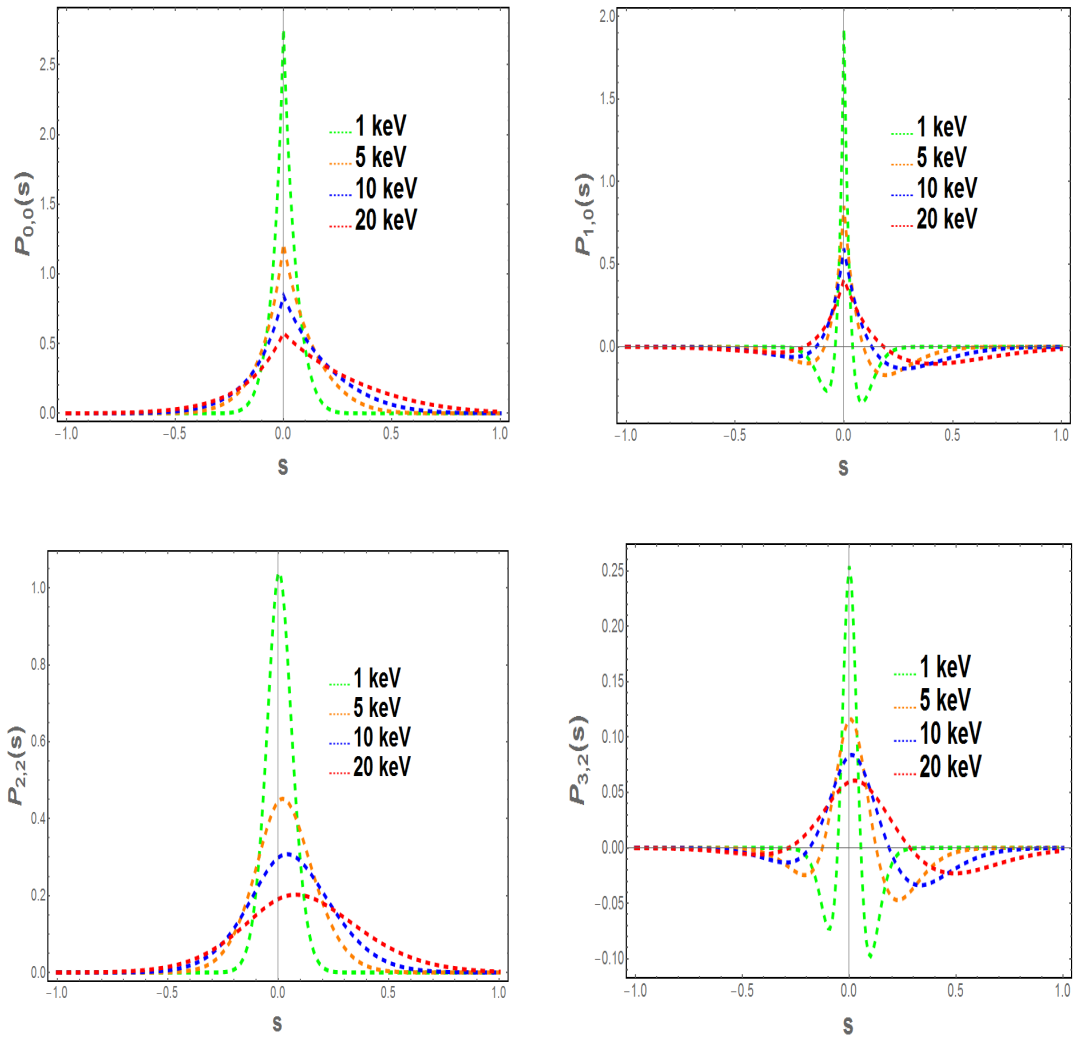


Figure 4.1: The redistribution function $P_{l,m}(s)$, for $l = 0, 1, 2, 3$ and $m = 0, 2$, for thermal electrons at different temperatures as indicated (Emritte et al. 2016).

meaning that our result is consistent with them. In Fig. 4.2 we show the function $P_{l,m}(s)$ for a non-thermal electron distribution for different minimum momentum p_1 following a power law with index $\alpha = 2.5$.

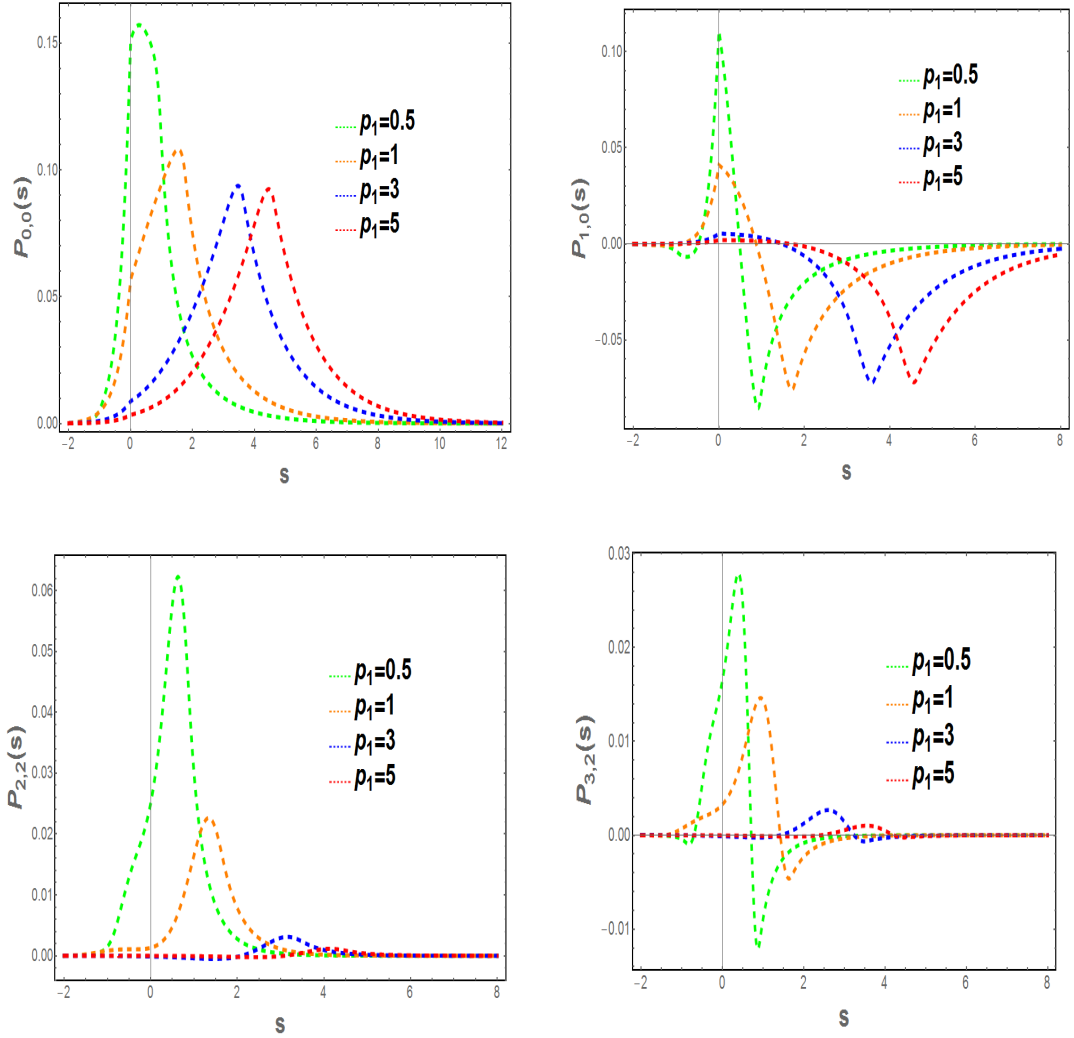


Figure 4.2: The redistribution function $P_{l,m}(s)$, for $l = 0, 1, 2, 3$ and $m = 0, 2$, for a single power law distribution of electrons with spectral index $\alpha = 2.5$ for different minimum momenta p_1 (Emritte et al. 2016).

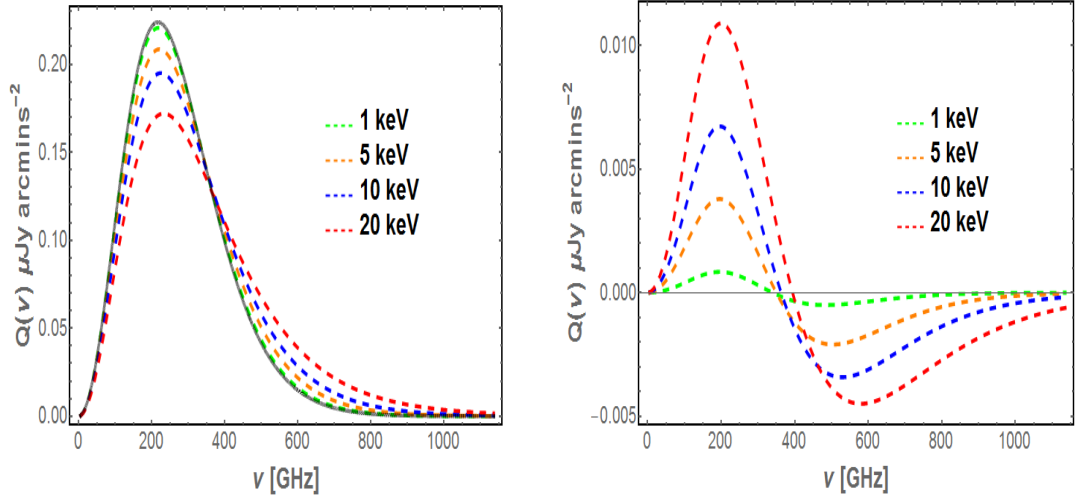


Figure 4.3: The spectrum of the Stokes parameter Q for different temperatures of a thermal electron distribution arising from the quadrupole (left) and octupole (right) of the CMB, assumed here to be $a_{2,2} = 1.3 \times 10^{-5}$ and $a_{3,2} = 8.7 \times 10^{-6}$, respectively. The red curve represents the non-relativistic Q . The optical depth value is $\tau = 0.001$ (Emritte et al. 2016).

4.1.5 CMB multipoles and polarization of the SZE

Now we proceed to derive the Stokes parameters Q and U for an anisotropic incident radiation. The Stokes parameter Q can be written as follows:

$$\begin{aligned} \frac{1}{\nu_1^3} \frac{\partial Q}{\partial \tau}(\nu_1) &= -\frac{3}{64\pi^2} \sum_{l=0}^{\infty} \sum_{m=-l}^l \int d\beta_e d\mu_e d\phi_e \frac{f_e(\beta_e)}{\gamma_e} \int \frac{d\mu_2 d\phi_0}{n_{12} n_{22}^4} \\ &\times [\cos(2\phi_0 + 2\phi_e) \sin^2(\theta_2) n_{12}^2 + 2 \cos(\phi_0 + 2\phi_e) \\ &\times \sin(\theta_2) \sin(\theta_e) n_{12} r_{12} \gamma_e \beta_e + \cos(2\phi_e) \sin^2(\theta_e) r_{12}^2 \beta_e^2 \gamma_e^2] \\ &\times \sqrt{\frac{2l+1}{4\pi} \frac{(l-m)!}{(l+m)!}} e^{im(\phi_0 + \phi_e)} P_l^m(\mu_2) f_{l,m} \left(\frac{n_{12}}{n_{22}} \nu_1 \right). \end{aligned} \quad (4.72)$$

Upon integration with respect to ϕ_e , only the terms with $m = \pm 2$ survive and we make use of the following property of the associated Legendre Polynomials

$$P_l^{-m}(\mu) = (-1)^m \frac{(l-m)!}{(l+m)!} P_l^m(\mu), \quad (4.73)$$

and we also impose the following condition on the photon redistribution function

$$f_{l,m}^*(\nu) = (-1)^m f_{l,-m}(\nu). \quad (4.74)$$

The Stokes parameter Q then is written as follows:

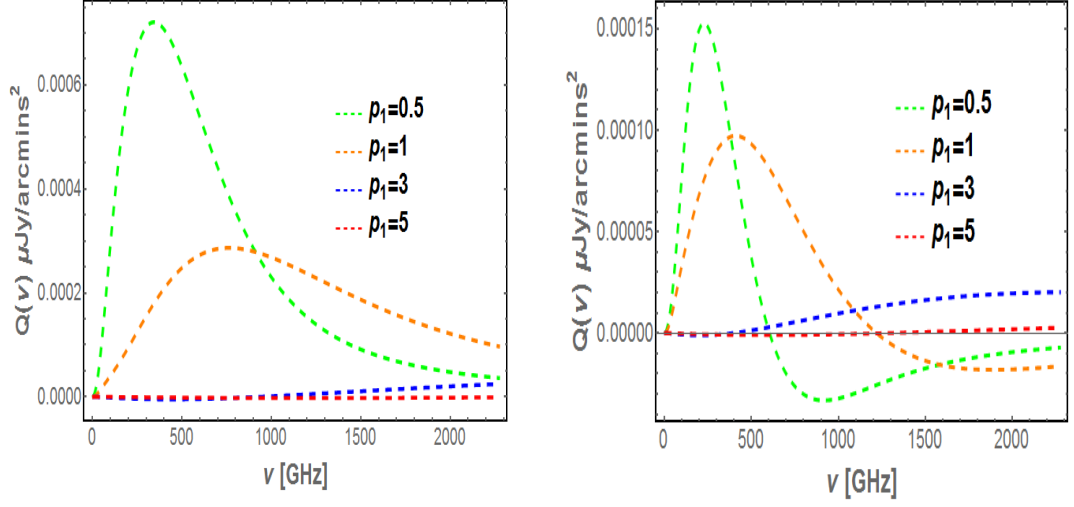


Figure 4.4: The spectrum of the Stokes parameter Q for the quadrupole (left) and octupole (right) in the case of a single power law distribution of electrons of spectral index $\alpha = 2.5$. The quadrupole of the CMB is assumed here to be $a_{2,2} = 1.3 \times 10^{-5}$ and that of the octupole to be $a_{3,2} = 8.7 \times 10^{-6}$. The optical depth value is $\tau = 1 \times 10^{-5}$ (Emritte et al. 2016).

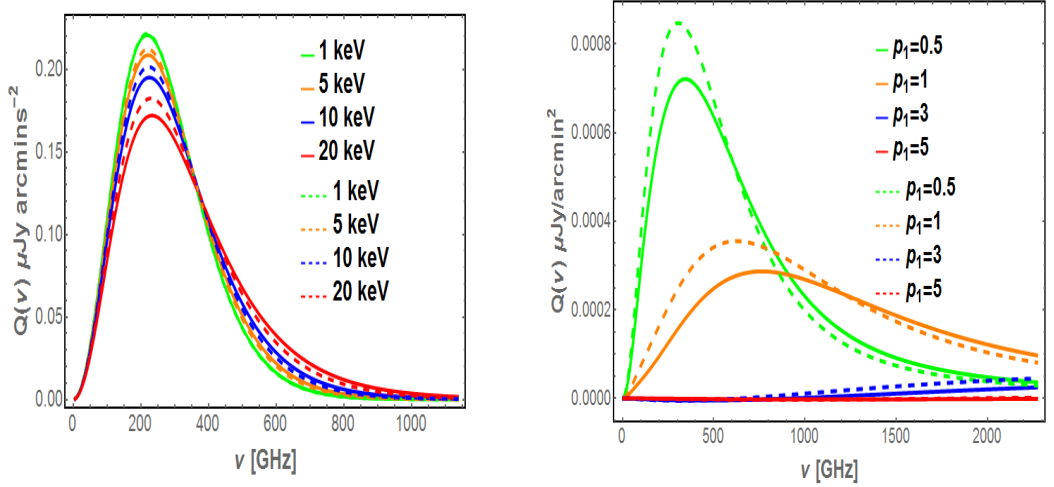


Figure 4.5: The spectrum of the Stokes parameter Q for the superposition of the CMB quadrupole and octupole for a thermal electron distribution (dashed curves in left panel) and for a non-thermal electron distribution (dashed curves in right panel). Optical depth values of 10^{-3} and 10^{-5} have been used for the thermal and non-thermal distributions, respectively. The spectral index of the power-law distribution is $\alpha = 2.5$. The straight curves represent the spectrum of Q where the contribution of only the quadrupole is considered (Emritte et al. 2016).

$$\begin{aligned}
 \frac{1}{\nu_1^3} \frac{\partial Q}{\partial \tau}(\nu_1) &= -\frac{3}{16\pi} \sum_{l=2}^{\infty} \sqrt{\frac{2l+1}{4\pi} \frac{(l-2)!}{(l+2)!}} \int d\beta_e d\mu_e \frac{f_e(\beta_e)}{\gamma_e} \\
 &\times \int \frac{d\mu_2 d\chi_0}{n_{12} n_{22}^4 \sqrt{1-\chi_0^2}} [(1-\mu_2^2)n_{12}^2 + 2n_{12}\beta_e\gamma_e(\mu_2-1)] \\
 &\times \chi_0 \sqrt{(1-\mu_2^2)(1-\mu_e^2) + \beta_e^2\gamma_e^2(\mu_2-1)^2(1-\mu_e^2)(2\chi_0^2-1)} \\
 &\times \text{Re} \left[f_{l,2} \left(\frac{n_{12}}{n_{22}} \nu_1 \right) \right] P_l^2(\mu_2) .
 \end{aligned} \tag{4.75}$$

Similarly the Stokes parameter U can be written like the previous one

$$\begin{aligned}
 \frac{1}{\nu_1^3} \frac{\partial U}{\partial \tau}(\nu_1) &= \frac{3}{16\pi} \sum_{l=2}^{\infty} \sqrt{\frac{2l+1}{4\pi} \frac{(l-2)!}{(l+2)!}} \int d\beta_e d\mu_e \frac{f_e(\beta_e)}{\gamma_e} \int \frac{d\mu_2 d\chi_0}{n_{12} n_{22}^4 \sqrt{1-\chi_0^2}} \\
 &\times [(1-\mu_2^2)n_{12}^2 + 2n_{12}\beta_e\gamma_e(\mu_2-1)\chi_0 \sqrt{(1-\mu_2^2)(1-\mu_e^2)} \\
 &+ \beta_e^2\gamma_e^2(\mu_2-1)^2(1-\mu_e^2)(2\chi_0^2-1)] \\
 &\times \text{Im} \left[f_{l,2} \left(\frac{n_{12}}{n_{22}} \nu_1 \right) \right] P_l^2(\mu_2) .
 \end{aligned} \tag{4.76}$$

These expressions can actually be simplified further into the following equations similar to those used to compute the intensity I

$$\begin{aligned}
 \frac{1}{\nu_1^3} \frac{\partial Q}{\partial \tau}(\nu_1) &= \sum_{l=0}^{\infty} \int_{-\infty}^{\infty} P_{l,2}(s) \text{Re} [f_{l,2}(e^s \nu_1)] ds \\
 \frac{1}{\nu_1^3} \frac{\partial U}{\partial \tau}(\nu_1) &= -\sum_{l=0}^{\infty} \int_{-\infty}^{\infty} P_{l,2}(s) \text{Im} [f_{l,2}(e^s \nu_1)] ds ,
 \end{aligned} \tag{4.77}$$

where

$$\begin{aligned}
 P_{l,2}(s) &= \int_{\sinh(|s|/2)}^{\infty} P_{l,2}(s, p_e) f_e(p_e) dp_e \\
 P_{l,2}(s, \beta_e) &= -\frac{3}{32\pi} \sqrt{\frac{2l+1}{4\pi} \frac{(l-2)!}{(l+2)!}} \frac{e^{\frac{3}{2}s}}{\gamma_e^2 \beta_e^2} \int_{-t_0}^{t_0} e^{\frac{t}{2}} dt \\
 &\times \int_{A-B}^{A+B} d\mu_0 \frac{P_l^2(1+e^t(\mu_0-1))}{\sqrt{B^2-(A-\mu_0)^2}} \frac{\mu_0-1}{2+e^t(\mu_0-1)} \\
 &\times \left[(\mu_0-1) [2 - e^t(\gamma_e^2(\mu_0-1)(1+\beta_e^2) - 2)] \right. \\
 &\left. - 8\gamma_e(\mu_0-1)e^{t/2} \cosh\left(\frac{s}{2}\right) - 4 \cosh s \right] .
 \end{aligned} \tag{4.78}$$

The variables A, B and t are given in eq.4.66. The redistribution kernel $P_{l,2}(s)$ follows a similar kind of relationship to that of $P_{l,0}(s)$ written as follows

$$P_{l,2}(-s) = e^{-3s} P_{l,2}(s) . \tag{4.79}$$

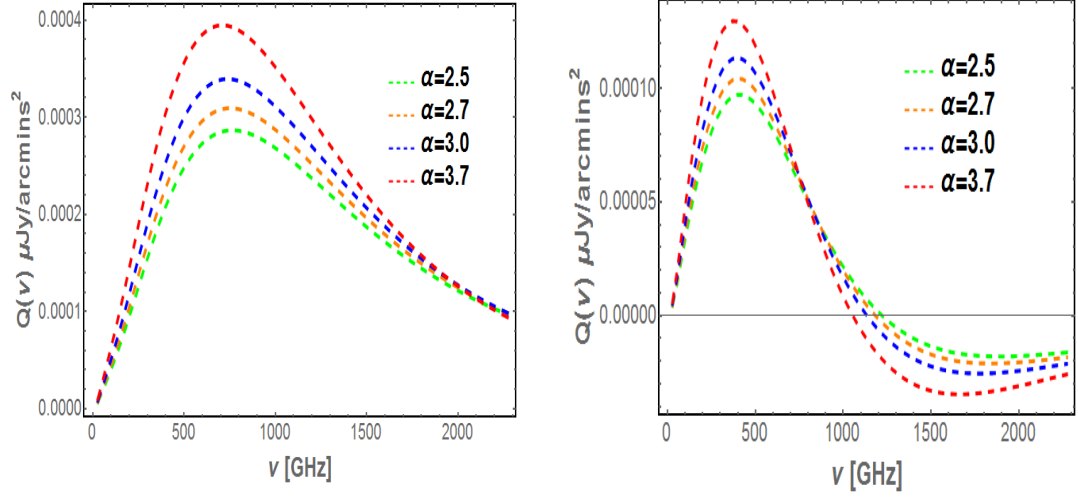


Figure 4.6: The spectrum of the Stokes parameter Q for the CMB quadrupole and octupole computed for different spectral index α of a single power-law distribution of electrons. The values of the minimum momentum and optical depth here are $p_1 = 1$ and 1×10^{-5} , respectively (Emritte et al. 2016).

This allows us to cast the Stokes parameters Q and U in terms of the incident radiation intensity, and for completeness we also include the intensity Stokes parameter I

$$\begin{aligned}
 \frac{\partial I}{\partial \tau}(x, \hat{z}) &= \sum_{l=0}^{\infty} \left[\int_{-\infty}^{\infty} P_{l,0}(s) I_{l,0}(e^{-s}x) ds - \sqrt{\frac{2l+1}{4\pi}} I_{l,0}(x) \right], \\
 \frac{\partial Q}{\partial \tau}(x) &= \sum_{l=2}^{\infty} \int_{-\infty}^{\infty} P_{l,2}(s) \text{Re}[I_{l,2}(e^{-s}x)] ds, \\
 \frac{\partial U}{\partial \tau}(x) &= - \sum_{l=2}^{\infty} \int_{-\infty}^{\infty} P_{l,2}(s) \text{Im}[I_{l,2}(e^{-s}x)] ds.
 \end{aligned} \tag{4.80}$$

Furthermore, eq. 4.80 can also be extended to accommodate a combination of electron populations. This can be done by writing the functions $P_{l,m}(s)$ as follows

$$\begin{aligned}
 P_{l,m}(s) &= \int f_e(p_e) P_{l,m}(s, p_e) dp_e \\
 &= \int C_A f_{e,A}(p_e) P_{l,m}(s, p_e) + C_B f_{e,B}(p_e) P_{l,m}(s, p_e) dp_e \\
 &= C_A P_{l,m,A}(s) + C_B P_{l,m,B}(s),
 \end{aligned} \tag{4.81}$$

where $P_{l,m,A}(s)$ and $P_{l,m,B}(s)$ are the $P_{l,m}(s)$ function for each electron distribution. The

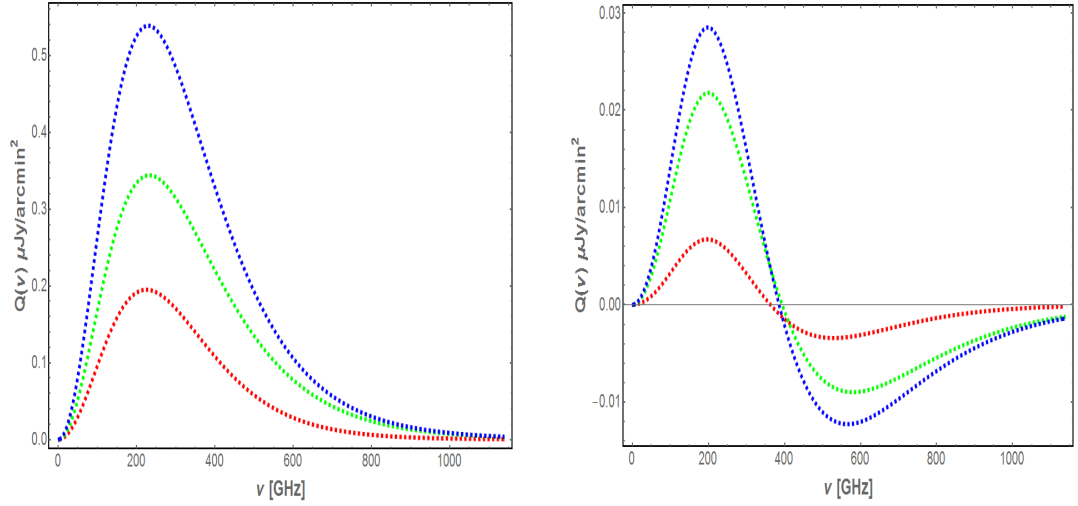


Figure 4.7: The spectrum of the Stokes parameter Q for the quadrupole (left panel) and the octupole (right panel) computed for a combination of two thermal electron populations (blue curves): a thermal electron population with $kT = 10$ keV and $\tau = 0.001$ (red curves) and another thermal electron population with $kT = 20$ keV and $\tau = 0.002$ (green curves) (Emritte et al. 2016).

Stokes parameters can then be written as follows,

$$\begin{aligned}
 \frac{\partial I}{\partial \tau}(x, \hat{z}) &= \frac{\tau_A}{\tau} \sum_{l=0}^{\infty} \int_{-\infty}^{\infty} P_{l,0,A}(s) I_{l,0}(e^{-s}x) ds + \\
 &\quad + \frac{\tau_B}{\tau} \sum_{l=0}^{\infty} \int_{-\infty}^{\infty} P_{l,0,B}(s) I_{l,0}(e^{-s}x) ds - \sqrt{\frac{2l+1}{4\pi}} I(x, \hat{z}), \\
 \frac{\partial Q}{\partial \tau}(x, \hat{z}) &= \frac{\tau_A}{\tau} \sum_{l=0}^{\infty} \int_{-\infty}^{\infty} P_{l,2,A}(s) \text{Re}[I_{l,2}(e^{-s}x)] ds + \\
 &\quad + \frac{\tau_B}{\tau} \sum_{l=0}^{\infty} \int_{-\infty}^{\infty} P_{l,2,B}(s) \text{Re}[I_{l,2}(e^{-s}x)] ds \\
 \frac{\partial U}{\partial \tau}(x, \hat{z}) &= -\frac{\tau_A}{\tau} \sum_{l=0}^{\infty} \int_{-\infty}^{\infty} P_{l,2,A}(s) \text{Im}[I_{l,2}(e^{-s}x)] ds + \\
 &\quad - \frac{\tau_B}{\tau} \sum_{l=0}^{\infty} \int_{-\infty}^{\infty} P_{l,2,B}(s) \text{Im}[I_{l,2}(e^{-s}x)] ds,
 \end{aligned} \tag{4.82}$$

where τ_A and τ_B are the optical depths of electron population A and B, respectively.

4.2 Polarization spectra

The Stokes parameters, Q and U , can be computed using eq. 4.80 up to any value of l ; however in this present work, we restrict ourselves up to $l = 3$, which corresponds to the

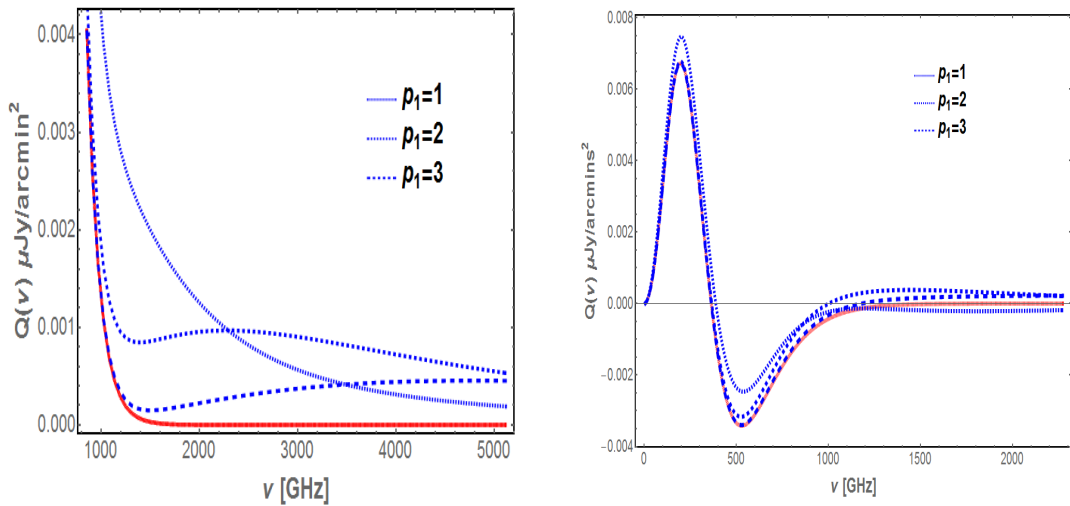


Figure 4.8: The spectrum of the Stokes parameter Q for the CMB quadrupole (left panel) and octupole (right panel) for a thermal electron distribution with $kT = 10$ keV and $\tau = 10^{-3}$ (red curves) combined with a power-law electron distribution, spectral index $\alpha = 2.5$ and $\tau = 10^{-4}$, for different minimum momentum p_1 . The blue curves represent the resulting spectrum for different values of p_1 (Emritte et al. 2016).

octupole. In Fig 4.3, for different temperatures of a thermal plasma hosted by a cosmic structure, we show the Stokes parameters Q arising from the quadrupole (Left) and octupole (Right). It is noticed that, even though our calculation is restricted to non-moving clusters, the octupole is non-zero, and with higher temperature, its contribution becomes more apparent. This result can be contrasted with a previous work (Yasini & Pierpaoli 2016) whereby kinematic effects were the source of the octupole contribution to polarization. Furthermore, the spectral features of the quadrupole and the octupole are distinct. Relativistic effects become more pronounced for hot clusters while for low electron temperatures, $kT < 1$ keV, the relativistic spectrum and the non-relativistic one become nearly identical in the case of the CMB quadrupole. This shows the consistency our derivation.

The peak of the relativistic Q spectrum (see Fig 4.3) for the quadrupole occurs roughly around the same frequency as that of the non-relativistic one, ≈ 216 GHz, but slightly deviating towards higher frequencies as the temperature increases, reaching 230 GHz for 20 keV. Additionally, the peak value of the spectrum is slightly lowered as the temperature is increased, and the difference between a cluster at 20 keV and a cluster at 1 keV being $\approx 0.05 \mu\text{Jy}/\text{arcmin}^2$ at 216 GHz for an optical depth of $\tau = 0.001$.

The Q spectrum amplitude of the octupole is smaller in comparison to the quadrupole component, but increases with temperature. A maximum value of $0.01 \mu\text{Jy}$ occurs at 204 GHz for $kT_e = 20$ keV. A notable spectral feature of the Q spectrum for the octupole is the

existence of a cross-over frequency which is ≈ 340 GHz in the thermal case for $kT = 1$ keV and increases with electron temperature; for a temperature of 20 keV it is found at ≈ 396 GHz. This cross-over frequency implies a change in the polarization state, e.g. changing from vertically polarized to horizontally polarized. In Fig 4.9 (top panel), we demonstrate the variation of the cross-over frequency ν_0 as a function of the temperature of a thermal gas. The cross-over frequency varies with the temperature as $\nu_0 = [335 + 2.84(kT/keV)]$ GHz, hence this relationship provides, in principle, a way to measure the electron temperature. However, sufficient frequency accuracy would be needed to locate the cross-over frequency and also other polarized components that can act as biases need to be accounted for properly and subtracted.

The CMB octupole term contributes to the total polarization spectrum like a perturbation of the main contribution that is given by the CMB quadrupole term. As an illustration of this point, we show in Fig. 4.5 (left panel) the spectrum of the total Stokes parameter Q from the superposition of the CMB quadrupole and octupole for a thermal electron distribution. The presence of the CMB octupole-induced contribution makes the peak of the total Q spectrum higher at the frequency of the maximum of the CMB quadrupole-induced spectrum, reaching values of $0.182 \mu\text{Jy}$ instead of $0.172 \mu\text{Jy}$ for $kT_e = 20$ keV. At frequencies higher than ≈ 371 GHz, the total Q spectrum becomes lower in amplitude w.r.t. the case of the CMB quadrupole-induced contribution due to the negative amplitude of the CMB octupole-induced term in this frequency range. Therefore, the contribution of the CMB octupole term is small but not negligible, and one could consider using the cross-over frequency of the CMB octupole term to measure the cluster electron temperature.

X-ray observations in conjunction with polarized radio measurements can be used to separate the CMB quadrupole and octupole from each other. This can be done by extracting temperature through X-ray observations which can be used to fit the CMB octupole polarization spectrum and therefore, disentangle its contribution from the CMB quadrupole in the total polarization spectrum (see Fig. 4.5). Knowledge of the temperature would allow the cross-over frequency to be found and measuring at that frequency would reveal the quadrupole-induced SZE. Once the CMB quadrupole-induced term is derived, it can be subtracted from the total Q spectrum thus disentangling the CMB octupole-induced term.

Furthermore, we also compute the Q spectrum of the quadrupole and octupole for the case of non-thermal electrons. In Fig 4.4, we display the spectra for different values of the minimum momentum p_1 for the case of a single power law electron distribution with spectral index, $\alpha = 2.5$, which is representative of the observed spectra in radio-halos and radio-galaxies. Because of the lower optical depth of the non-thermal plasma, the amplitude of the spectrum is smaller than in the thermal case, and is sensitive to the value of p_1 . As expected, the non-thermal Q spectrum extends to much higher frequencies depending on

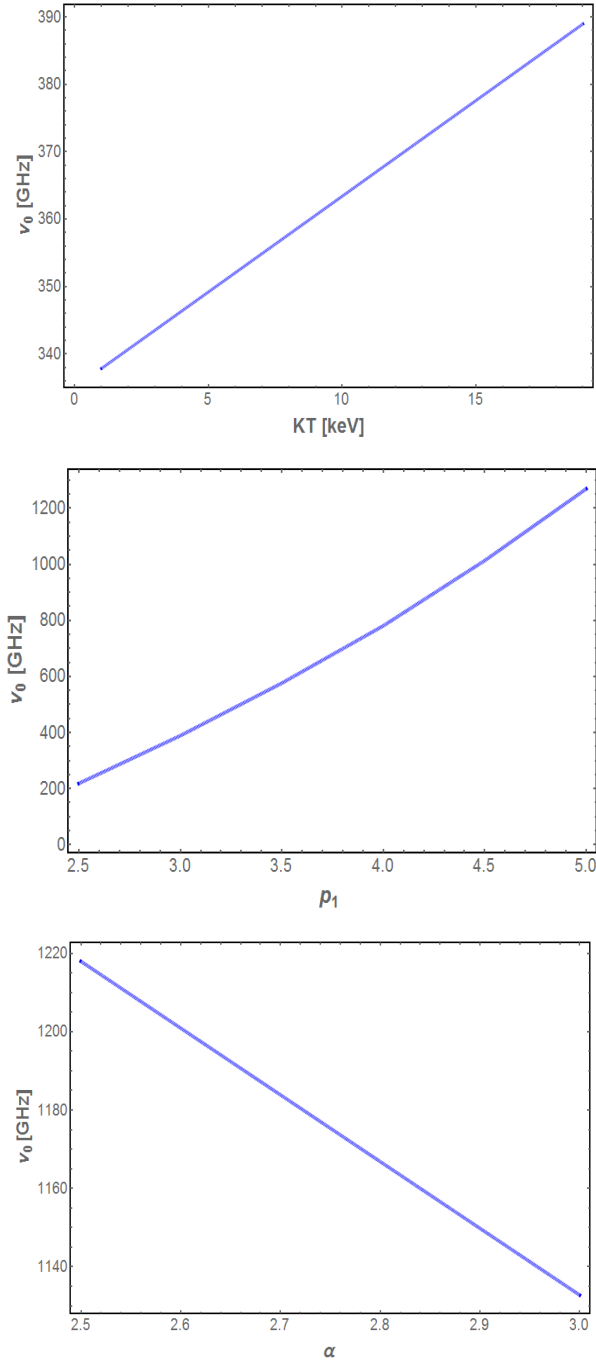


Figure 4.9: The variation of the cross-over frequency ν_0 as a function of the electron temperature (top panel) for the case of a thermal distribution of electrons, of the minimum normalized momentum p_1 for a non-thermal electron distribution (mid panel) for a fixed $\alpha = 2.5$, and of the spectral index α (bottom panel) in the case of a power-law electron distribution for a fixed $p_1 = 1$ (Emritte et al. 2016).

the value of p_1 . Fig 4.6 shows how the spectrum changes with different spectral index α . A softer index leads to higher amplitude of the spectrum.

The non-thermal Q spectrum of the octupole also displays a cross-over frequency which is sensitive to the minimum momentum p_1 and the spectral index α . Fig 4.9 shows the variation of the cross-over frequency with respect to p_1 (mid-panel) for $p_1 > 2.5$ and with α (bottom-panel). Interestingly, two values of the cross-over frequency are seen for p_1 greater than ≈ 2 : in fact, for $p_1 = 3$, the cross-over frequencies are found at 389 GHz and 4000 GHz. We find that the relationship between the cross-over frequency ν_0 and p_1 is not linear but quadratic in p_1 and it can be described by a polynomial $\nu_0 = (-284.3 + 93.4p_1 + 43.4p_1^2)$ GHz in the range $p_1 \approx 2.5 - 5.0$. This relation can be used to derive the value of p_1 if the cross-over frequency is measured with sufficient frequency resolution. We also show in Fig. 4.5 (right panel) the spectrum of the total non-thermal Stokes parameter Q from the superposition of the CMB quadrupole and the octupole contributions to the total Q .

For fixed momentum p_1 , the cross-over frequency of the CMB octupole Q spectrum is sensitive to the spectral index α . A softer index leads to lower values of the cross-over frequency. Fig 4.9 (bottom panel), we illustrate the relationship between the cross-over frequency ν_0 and the spectral index α . A linear relationship is found which can be reproduced by the relation $\nu_0 = (1644 - 170.3\alpha)$ GHz. This can be used to measure α if the value of p_1 is known. The combination of the dependence of the cross-over frequency on p_1 and α can be used to set constraints on spectral parameters of the non-thermal electron distribution.

Using eq. 4.82, we compute the resulting Q spectrum produced by simultaneous IC scattering of CMB photons by two electron populations occupying the same region. In Fig. 4.7, we show the resulting spectrum (blue curve) for a combination of two thermal electron distributions with different temperature and optical depth. The overall spectrum is the superposition of the individual spectra. Another interesting scenario is the production of polarization via IC scattering by a combination of thermal and non-thermal electrons. We show in Fig. 4.8 the resulting spectrum (blue curve) at high frequencies for a thermal electron distribution combined with a non-thermal electron population, for different values of the minimum momentum p_1 . At low frequencies, the impact of the non-thermal Q spectrum has less impact on the overall polarization spectrum because of the low number density of non-thermal electrons compare to thermal ones. Therefore at low frequencies, the thermal spectrum dominates over the non-thermal one, but at high frequencies (>1000 GHz) the polarization spectrum becomes entirely non-thermal.

Interestingly, the existence of a non-thermal distribution superposed on a thermal distribution has an impact on the value of the cross-over frequency ν_0 of the CMB octupole Q spectrum. Without a non-thermal distribution of electrons, we obtain $\nu_0 = 361$ GHz for $kT = 10$ keV, while in the presence of a non-thermal electron distribution with $p_1 = 1$,

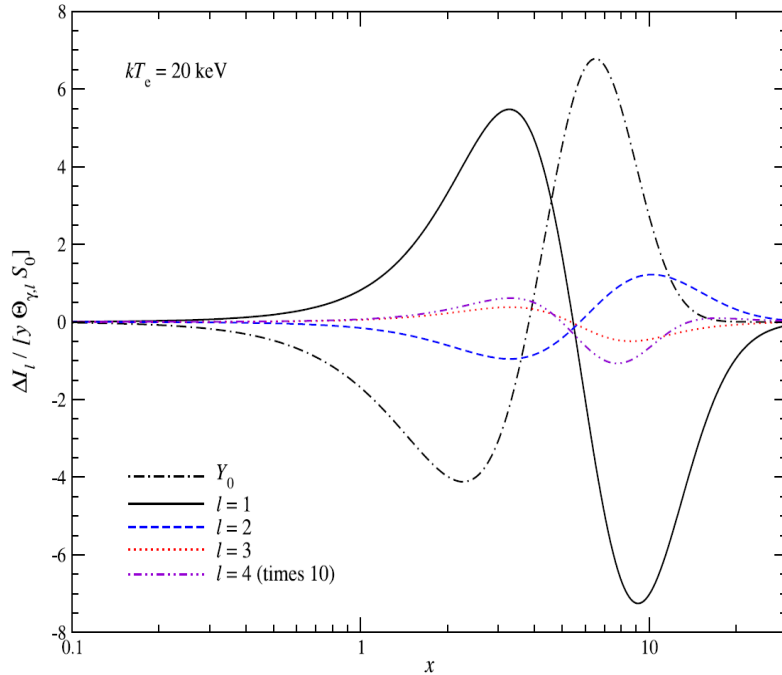


Figure 4.10: The scattering of primordial CMB anisotropies in intensity for a plasma temperature of 20 KeV showing the spectrum of Quad-I (blue) and Oct-I (red) (Fig from Chluba & Dai 2014). The quantity x is the dimensionless frequency.

$\nu_0 = 389$ GHz, $\nu_0 = 366$ GHz with $p_1 = 2$, and $\nu_0 = 361$ GHz with $p_1 = 3$. The presence of a non-thermal distribution of electrons with $p_1 > 1$ produces an additional cross-over frequency ν_0 , e.g. at ≈ 1000 GHz for $p_1 = 2$ and ≈ 1191 GHz for $p_1 = 3$. The cross-over frequency depends on the minimum momentum p_1 of the non-thermal distribution, as lower values of p_1 lead to higher cross-over frequencies. As in the case of a thermal electron distribution, it is possible to measure p_1 from the CMB octupole-induced spectrum at high frequencies and then disentangle the two electron populations in a galaxy cluster involving non-thermal activities. The SZE intensity spectrum can exhibit features from the dipole, quadrupole and octupole (eq. 4.69) of the CMB when the anisotropy of the radiation is taken into account. In the intensity case, the dipole, quadrupole and octupole spectrum are suppressed by $a_{l,0}$ and the Compton parameter $y = \tau kT_e/m_e c^2$. Therefore, it is interesting to compare the quadrupole (Quad-I) and octupole (Oct-I) spectrum of the intensity case to the ones that we have obtained in the polarization spectrum. The spectrum of Quad-I exhibits different spectral features compared to the polarization counterpart. The quadrupole induced spectrum in the polarization case is positive over all frequencies (see Fig. 4.3) whereas Quad-I is negative before 343 GHz and positive after that, meaning 343 GHz is a cross-over frequency for Quad-I for $kT_e = 20$ keV (see Fig 4.10). The amplitude of Quad-I is comparable to the octupole in our case, at 190 GHz Quad-I is $-0.01 \mu\text{Jy}/\text{arcmin}^2$

and the octupole in our case is also around $0.01 \mu\text{Jy}/\text{arcmin}^2$. In the case of Oct-I, it is even more suppressed compared to our case, for $kT_e = 20 \text{ keV}$ at 190 GHz , the Oct-I is $0.002 \mu\text{Jy}/\text{arcmin}^2$ and the octupole in our case is $0.01 \mu\text{Jy}/\text{arcmin}^2$. Also the cross-over frequency in the case of the Oct-I is approximately at the same cross-over frequency as Quad-I, 343 GHz for $kT_e = 20 \text{ keV}$ and not at the same frequency as our octupole's cross-over frequency, which for $kT_e = 20 \text{ keV}$ is 230 GHz (see Fig 4.10).

4.2.1 Application to the Bullet cluster

In this section, we investigate the possibility of detecting SZE polarization arising from the multipoles of the CMB for the case of the Bullet cluster. In order to do so, we calculate the Stokes parameter Q using the parameters derived from SZE intensity measurements of the cluster.

SZE measurements for this particular cluster are available over a wide frequency interval: ACBAR at 150 and 275 GHz (Gomez et al. 2004), with the SEST telescope at 150 GHz (Andreani et al. 1999), with APEX at 150 GHz (Halverson et al. 2009), the SPT at 150 GHz (Plagge et al. 2010), ATCA at 18 GHz (Malu et al. 2010) and Herschel-SPIRE at 600 , 850 and 1200 GHz (Zemcov et al. 2010). The availability of multifrequency data have allowed multiple components of the SZE intensity signal to be determined (Colafrancesco et al. 2011, Marchegiani & Colafrancesco 2015). Assuming spherical symmetry and neglecting the effect of possible variations of the electron temperature along the line of sight (see Chluba et al. 2013), the SZE signal of the main sub-cluster is better explained using two electron components, a thermal electron distribution with optical depth $\tau = 1.1 \times 10^{-2}$ and temperature $kT = 14.2^{+0.3}_{-0.2} \text{ keV}$ (Wik et al. 2014) that is co-spatial with a non-thermal electron distribution with optical depth 3×10^{-4} (Ota & Mitsuda 2004), $p_1 = 1$ and spectral index $\alpha = 3.7$ (Marchegiani & Colafrancesco 2015). Using these parameters, we determine the Q spectrum for this cluster by calculating the polarized flux integrated over a region of radius 5 arcmin from the center of this cluster.

Fig. 4.11 shows the SZE polarization spectrum (red curve) computed up to 10^4 GHz from the superposition of the CMB quadrupole (dashed-blue) and the octupole (dotted-blue) signals. At 215 GHz , the polarization signal (red) is maximum, $\approx 160 \mu\text{Jy}$, and the cross-over frequency of the octupole is found to occur at 383 GHz . At this frequency, there is no contribution from the quadrupole signal and for frequencies $> 383 \text{ GHz}$, the polarization spectrum (red curve) goes below that of the CMB quadrupole spectrum (dashed-blue). This demonstrates how the CMB octupole signal contributes constructively to the CMB quadrupole one below the cross-over frequency ($\approx 383 \text{ GHz}$) and for frequencies above this, contributes destructively. Using eq. 1.49, we can estimate the degree of polarization at some specific frequencies and we obtained for 10 GHz $\Pi = 1.65 \times 10^{-6}$, for 200 GHz $\Pi = 3 \times 10^{-6}$

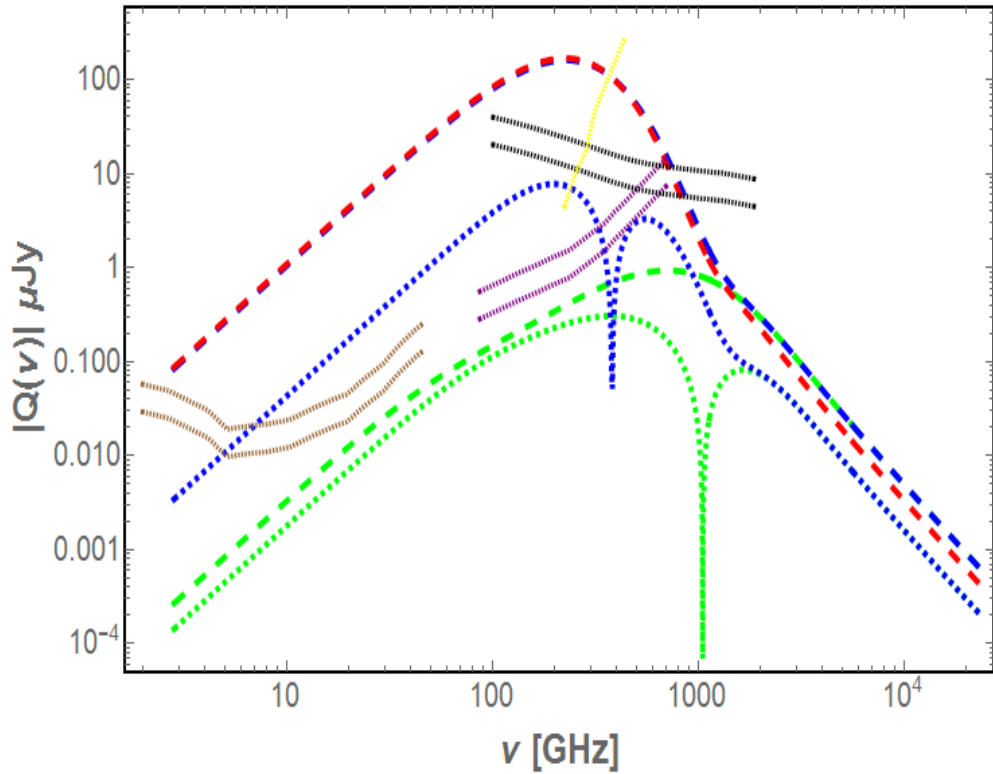


Figure 4.11: The polarization spectrum (dashed-red) of the Bullet cluster calculated over 5 arcmin^2 . The dashed- blue curve is the quadrupole spectrum whereas the dotted-blue is that of the octupole. The green curves represent the non-thermal quadrupole (dashed green) and octupole (dotted green). The brown, purple and the black curves represent the sensitivity of SKA, ALMA and *Millimetron* for 260 and 1000 hrs of integration. The yellow curve represents the sensitivity of CORE++ (Emritte et al. 2016).

and for 1000 GHz $\Pi = 7.7 \times 10^{-4}$.

The Q spectrum of the quadrupole (dashed-green) and octupole (dotted-green) produced by non-thermal electrons are also shown in Fig. 4.11 to highlight the impact of the non-thermal component. Due to the low value of the minimum momentum, $p_1 = 1$, for this particular cluster, the non-thermal components are not completely negligible over the whole spectrum. For frequencies < 2000 GHz, the overall polarization spectrum is mostly thermal whereas at frequencies $\gtrsim 2000$ GHz, the non-thermal component becomes more apparent. We also show in Fig. 4.11 the sensitivities of SKA (brown), ALMA (purple) and *Millimetron* (black) for 260 and 1000 hrs of integration. The sensitivities of SKA and ALMA are at 1σ while that of *Millimetron* is at 5σ . It is important to stress that these polarization sensitivities are estimated by assuming that the Stokes Q sensitivity is a factor of $\sqrt{2}$ higher than the Stokes I sensitivity. We have also shown the CORE++ sensitivity (yellow) (<http://www.core-mission.org/documents/CoreProposalFinal.pdf>).

4.3 Polarized IC scattering at high energies

Polarization arising from IC scattering of CMB photons has been calculated in the previous sections, taking into account relativistic effect and the spectral features associated with the polarization has been highlighted in the 100-2000 GHz frequency region. However, given the relativistic nature of the non-thermal electrons found in radio halos or lobes of radio galaxies, the non-polarized spectrum of IC scattering of CMB photons has been shown to extend up to very high frequencies e.g. X-rays and Gamma rays and hence is also expected for the polarization component.

Even if relativistic effects are taken into consideration, the Comptonization process that we have studied relies on the Thomson limit, $E \ll \gamma_e m_e c^2$, where E is the energy of the outgoing photon. This assumption is justified for gamma rays up to about 100 GeV, given the fact that the CMB comprises mainly of low energy photons. In fact, in the Thomson limit of IC scattering of the CMB, the energy of the outgoing photon is related to the electron energy via $E = 8(E_e/GeV)^2$ keV (e.g. Longair 1994) where E_e is the energy of the electron. Using this relation and inserting it into the Thomson limit validity relation, one can obtain $\gamma_e \ll 10^8$ which will correspond to maximum photon energy $E \ll 10$ TeV. Therefore it is fully justified to use the Thomson limit for an output photon energy of 100 GeV; this result is in accordance with some previous results (e.g. Fargion & Salis 1998, Birkinshaw 1999, Colafrancesco & Marchegiani 2010). Since this is the case for the IC scattering in intensity, this will also be true for the polarization component as well, which implies that eq. 4.80 or eq. 4.82 is still applicable to describe polarization due to the anisotropy of the CMB at high frequencies. Therefore, we extrapolate eq. 4.80 for the case of a single power law electron distribution (eq. 1.29) up to high frequencies, ≈ 10 GeV.

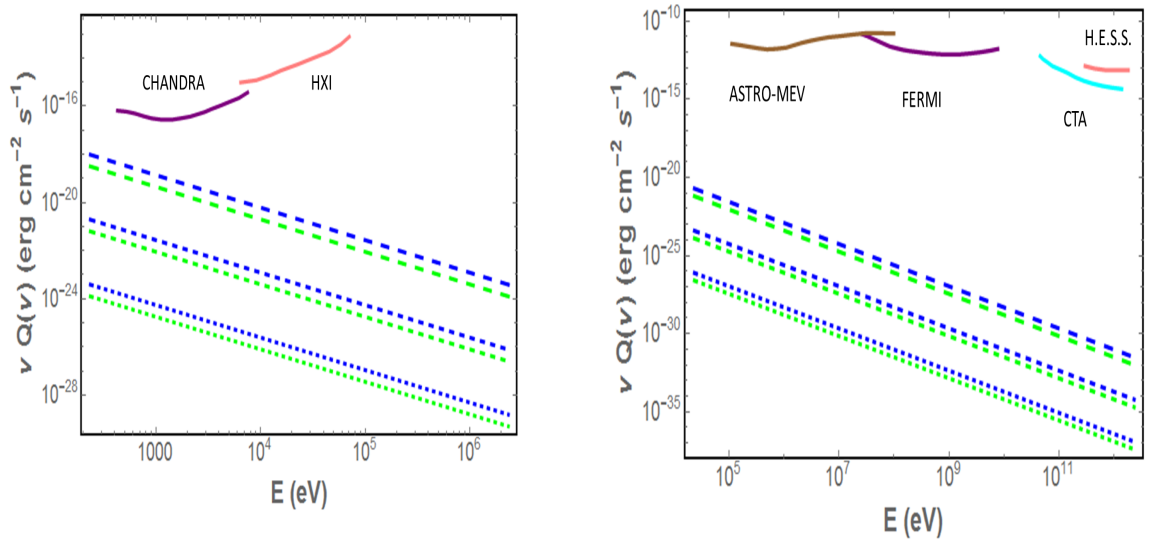


Figure 4.12: The polarized IC scattering of the CMB associated with the quadrupole (blue) and octupole (green) computed in the X-ray (left) and gamma-ray (right) bands for $p_1 = 1, 10, 100$ (bottom to top) and for $\alpha = 3.7$. In the left panel, we also show the sensitivity of *Chandra* for 5000 hrs at 3 sigma as well as *ASTROH-HXI* for 5000 hrs at 3 sigma. We also show in the right panel the sensitivity of *AstroMeV* for 10 years at 3 sigma, *FERMI* for 10 years at 5 sigma, *H.E.S.S.* and *CTA* at 5 sigma for 5000 hrs.

4.4 Polarization spectra at high frequencies

Using eq. 4.80, we calculate the IC polarized flux for the case of a typical galaxy cluster/lobes of radio-galaxies by assuming a spectral index of $\alpha = 3.7$ and we consider values of the momentum $p_1 = 1, 10, 100$ while holding $p_2 = 10^8$ fixed. Furthermore, we integrate the flux over a region of radius 5 arcmin assuming a value of $\tau = 3 \times 10^{-4}$. We demonstrate both in X-ray and gamma-rays, our calculated polarized flux in Fig. 4.12 for the case of the quadrupole (blue) and octupole (green), for a fixed value of $\alpha = 3.7$ and various values of $p_1 = 1, 10, 100$ (bottom to top). Higher values of p_1 lead to higher fluxes.

We also superimpose on Fig. 4.12 the sensitivities of various high energy instruments operating in the 1 keV–1 MeV and in the 0.1 MeV–0.1 TeV frequency intervals². However in both the X-ray region (1 keV–1 MeV) and the gamma-ray region (0.1 MeV–0.1 TeV), the polarization flux are very small and will be undetected by current and planned instruments.

²<http://astromev.in2p3.fr/?q=aboutus/pact>

4.5 Discussion and conclusions

By solving the polarized Boltzmann equation, we have been able to demonstrate the production of SZE polarization resulting from the anisotropy of the CMB when the photons of the latter are IC scattered by the electrons found in the atmosphere of cosmic structures. We derived under the Thomson approximation the Stokes parameters Q and U and when relativistic effects are accounted for, all the CMB multipoles are involved in the production of polarization even if the cluster is not moving. This can be contrasted with the non-relativistic counterpart, whereby only the quadrupole is involved. Contrary to previous calculations of the SZE polarization, we have calculated explicitly the Stokes parameter associated with the octupole of the CMB. The spectrum displays distinct spectral features compared to the quadrupole-induced polarization spectrum, in particular the existence of a cross-over frequency ν_0 . Although CMB multipoles higher than the octupole are involved in the production of SZE polarization, they have been neglected in our calculations. This is justified because their amplitudes will be comparatively small and the resulting signal will be well below the detection limit of current and upcoming instruments. Also, it has been demonstrated that higher order multipoles scatter at leading order of θ_e^2 and thus are indeed suppressed relative to the dipole, quadrupole and octupole scattering (see Chluba et al. 2013 and Chluba & Dai 2014).

Our present results have also shown that the SZE polarization spectrum is sensitive to the electron distribution involved in the IC scattering process. There are appreciable spectral differences between the SZE polarization spectra when the CMB photons are scattered by thermal electrons as compared to non-thermal ones. In the thermal case, the spectrum (quadrupole/octupole) is sensitive to the temperature of the electron plasma, whereas in the case of non-thermal electrons following a power-law electron distribution, the spectrum is sensitive to both the minimum momentum p_1 and the spectral index α . Also demonstrated in our results, is that the cross-over frequency associated with the octupole term is sensitive to the parameters of the electron distribution. The cross-over frequency depends on the temperature (e.g. 340 GHz for 1 keV, 365 GHz for 10 keV, 396 GHz for 20 keV) for a thermal electron distribution and on p_1 as well as α for that of a power-law electron distribution. Also, we have briefly discussed the source of biases in the determination of the cluster temperature and of the electron minimum momentum from the measurements of the cross-over frequency ν_0 , as well as the possibility to disentangle the CMB quadrupole and octupole terms from a prior measurement of the cluster temperature (or the minimum momentum of a non-thermal electron distribution) through either X-ray or SZE intensity observations.

Furthermore, we have also computed the polarization spectrum produced by combinations of electron populations occupying the same region of space. It is found that the

resulting spectrum is the superposition from each individual spectrum, e.g. in the case of two thermal electron distributions that occupy the same region within the ICM, the polarization spectrum is amplified by the distribution with higher temperature. Also, the cross-over frequency of the CMB octupole is displaced towards a higher frequency in the presence of an additional thermal electron distribution compared to the case of a single thermal electron distribution. In situations where there is a thermal electron distribution co-spatially existing with a non-thermal one, the polarization spectrum is only affected by non-thermal effects at higher frequencies. However for low values of p_1 (< 1), the non-thermal effects can also be apparent at lower frequencies. Again, the cross-over frequency of octupole polarization spectrum is shifted depending on the value of the momentum p_1 and the spectral index α .

Due to the possibility of accommodating two or more electron distributions, our approach has allowed us to use the parameters of the Bullet cluster derived from multifrequency SZE observations to determine its SZE polarization component. The spectrum of the Bullet cluster exhibits interesting spectral features that allow polarization arising from the CMB multipoles to be explored. In the frequency interval, 30 GHz to 700 GHz, the SZE polarization spectrum can be measured with a polarization sensitivity of $\approx 10 \mu\text{Jy}$. This frequency interval falls into the frequency coverage of ALMA and *Millimetron*, which cover approximately the interval 86 GHz up to 750 GHz and 100 GHz to 1800 GHz, respectively. Observing at ≈ 88 GHz where the sensitivity of ALMA is maximum, i.e. $\approx 0.3 \mu\text{Jy}$, the SZE polarization signal can be detected. The detection limit of ALMA is below both the predicted CMB quadrupole and octupole induced signals, which would render both signals observable.

The distinct spectral features of the CMB quadrupole induced polarization and that of the octupole one, would allow them to be disentangled using multifrequency observations. To achieve this, a strategy can be employed by observing at the cross-over frequency of the CMB octupole for clusters (e.g around 390 GHz for the Bullet cluster) whose temperature and optical depth are available from X-ray or SZE intensity measurements. At the cross-over frequency, the polarization spectrum consists of only the CMB quadrupole term without any contribution from the octupole one (being zero at its cross-over frequency). Then in order to recover the latter, one can measure the SZE polarization spectrum at another frequency where the CMB quadrupole-induced term can be subtracted to retain the octupole-induced one. However, this would require high spectral resolution in order to observe the signal with sufficient precision around the cross-over frequency.

Note, however, that knowledge of only the spectral shape of the quadrupole, octupole and the cross-over frequency may not be sufficient for the disentanglement of the two multipoles. Additional effects such as velocity corrections (Yasini & Pierpaoli 2016) and multiple scatterings (Chluba & Dai 2014) will have to be accounted for and their respective spectral shape

will also have to be known. Both the quadrupole and octupole spectrum are vulnerable to peculiar velocity effects. For moving clusters (non-zero peculiar velocities), the neighbouring CMB multipoles can leak into the quadrupole and octupole polarization spectrum. This effect is kinematic in nature, proportional to $\beta_c = V_c/c$ where V_c is the peculiar velocity of the cluster with respect to the CMB frame. The frequency weights of these leakages will impact the cross-over frequency of the octupole spectrum, hence for moving clusters, the peculiar velocity contribution to the polarization spectrum will have to be accounted for and treated properly. Multiple scattering impacts are less significant given that the amplitude is of the order of τ^2 except for rich clusters (where $\tau \approx 0.02$). In addition, multiple scattering effects can be reduced if measurements are performed symmetrically around the cluster's center.

We have also highlighted the promising experimental possibilities to measure the SZE that are offered by future experiments: the SKA can reach a sensitivity of $0.01 \mu\text{Jy}$ at 5 GHz and down to $0.1 \mu\text{Jy}$ at 45 GHz for 1000 hrs of integration time. This provides an opportunity for the SZE polarization spectrum to be measured with high accuracy at low frequencies. Unfortunately, low frequency measurements are vulnerable to the polarized synchrotron emissions coming from the radio halos or other sources. Nevertheless, their distinctive spectral features would allow them (Sazonov & Sunyaev 1999, Hall & Challinor 2014) to be treated and removed properly through multifrequency observations. In addition, if an r.m.s. value of the CMB quadrupole or the CMB octupole is what we are interested in, then by averaging over many clusters, the polarized synchrotron emissions would cancel each other. This is the case because the synchrotron polarization angle will not correlate from cluster to cluster. Hence combining ALMA and the SKA, the CMB quadrupole and the octupole-induced terms can be determined. The averaging process will also reduce the impact of polarization from kinematic effects, assuming the peculiar velocities of cosmic structures are uncorrelated.

The SZE polarization coming from non-thermal electrons reveals that polarization can also be searched for in the extended lobes of radio galaxies where IC emission have been observed. However high sensitivities ($\approx 0.01 \mu\text{Jy}$ at 20 GHz, $\approx 0.33 \mu\text{Jy}$ at 243 GHz) would be needed to at least measure the CMB quadrupole-induced spectrum. This would require at least 5000 hrs of integration time for SKA and ALMA.

It is important to mention that polarized foregrounds would have to be carefully taken into account and properly modelled when searching for SZE polarization. Measurements of polarized foregrounds over a wide range of frequencies would minimize modelling errors (see Dickinson 2014, Hall & Challinor 2014).

Another nuisance for both low and high frequency observations of SZE polarization from cosmic structures would be the background E-mode polarization of the CMB itself. Large scale E-modes will add a bias to the signal and also degrade the signal-to-noise (S/N) ratio.

However, the contribution from large-scale E-mode can be removed if SZE polarization measurement is done over a number of clusters. Since these E-modes are coherent from cluster to cluster, it can be removed from the desired signal. On the otherhand, small-scale E-modes will not affect the signal (see Hall & Challinor 2014).

Additionally, we have also been able to show that the polarized IC scattering of the CMB can manifest over the high-frequency portion of the electromagnetic spectrum and this is due to the relativistic nature of the non-thermal electrons that are present in cosmic structures such galaxy clusters and radio galaxies. Although our calculation has been done using the Thomson approximations, it is still valid at high energy. In addition we have also compared the computed flux with the sensitivities of various telescopes in the 1 keV–1 MeV and 0.1 MeV–0.1 TeV ranges. It is found that it is too difficult to measure the polarized flux as the latter are too small.

We finally discuss in the following the comparison between the results obtained in our work and previous ones.

The first difference between our work and previous ones (Sazonov & Sunyaev 1999, Challinor et al. 2000, Lavaux et al. 2004, Yasini & Pierpaoli 2016) lies in the generality of our approach, which allows the computation of SZE polarization for any electron distribution, whereas in previous works, a series expansion in terms of the temperature parameter, $\theta_e = k_B T_e / m_e c^2$, associated with a thermal electron distribution has been used to study the thermal SZE polarization only.

We also highlight our completely relativistic derivation of the SZE polarization spectra for both thermal and non-thermal electron distributions without any restrictive approximations other than the Thomson limit. Particularly, we have shown explicitly the SZE polarization spectrum produced by non-thermal electrons and therefore provides the possibility of searching for the signal in structures where non-thermal activities are taking place, such galaxy cluster radio-halos and lobes of radio-galaxies.

Furthermore we have also been able to compute the SZE polarization produced by a combination of electron populations occupying the same region of space within a cosmic structure.

We also stress here that we have computed for the first time the Q spectrum associated with the octupole in the case of a non-moving cluster, although for moving clusters the octupole does induce polarization via kinematic effects (Yasini & Pierpaoli 2016). In the case where the cluster is not moving, the usual SZE polarization is recovered, proportional to only the quadrupole. Our present results show that, in the presence of relativistic effects, the octupole is indeed involved in the production of SZE polarization, even though the cosmic structure is at rest with respect to the CMB frame. This octupole contribution becomes important in the case of high temperature clusters, as well as in lobes of radio-galaxies where

relativistic electrons are present. The Q spectrum of the octupole exhibits an interesting spectral feature, i.e. a cross-over frequency, which can be used to estimate the electron temperature (for a thermal electron population), or the minimum momentum p_1 and the spectral index α of non-thermal electron distributions. The existence of a cross-over frequency also shows the difference between the nature of the octupole-induced polarization due to relativistic effect and that of kinematic effects, whereby in the latter no cross-over frequency is found in the octupole spectrum. We also discussed how multifrequency observations, by taking advantage of the CMB octupole's cross-over frequency, would allow one to disentangle the CMB quadrupole and octupole-induced spectrum. However we also stress that to achieve this, velocity corrections and multiple scatterings will have to be treated properly.

Furthermore, we have also computed the complete polarization spectrum expected from the Bullet cluster using parameters derived from multifrequency observations of the SZE intensity. In the context of expectations from observed clusters, we have shown that telescopes like the SKA, ALMA, *Millimetron* and CORE++ have the sensitivity to measure the polarization spectrum from a typical Bullet-like cluster. A statistical study of the SZE polarization signals from a sample of high-T clusters will be presented elsewhere and will point to cosmological applications of this technique in large-scale observations of the polarized cosmic microwave background.

Finally, we have also shown that the spectrum produced by the IC scattering process between the CMB and non-thermal electrons can stretch up to very high very frequencies e.g. X-rays and Gamma rays. Although our calculations relies on the Thomson limit, but we have shown that our results are still valid up to ≈ 10 TeV.

Chapter 5

Conclusions and remarks

In this last chapter, we summarize the findings of this work and provide some discussions and suggestions for future work.

We have been able to successfully compute the SZE-21cm using four models representing the physical processes happening between redshifts $z = 45$ (30 MHz) and $z = 6$ (200 MHz). Two of the models take into account the role of dark matter annihilation during these early epochs. Our results on the SZE-21cm demonstrate that the study of the EoR and the DA is entirely possible through the use of the comptonization processes happening in large scale structures. The spectral features of the SZE-21cm are distinct for each model, hence the physical processes occurring can in principle be discerned using spectral analysis. Relativistic effects have appreciable impacts on the spectral feature of the SZE-21cm, in particular around frequencies, $\nu \approx 50, 60, 77, 95$ MHz. The SZE-21cm presents itself as a perturbation of the standard SZE, and the difference ($\Delta I_{\text{mod}} - \Delta I_{\text{st}}$) between them is on the level of $\approx \mu\text{Jy}$ which is within the reach of the SKA at 1000 hrs of integration time. Following a wise strategic approach by targeting high temperature cosmic structures (> 10 keV) and also observing at frequencies > 100 MHz, the signal can be observed with both SKA-1 and SKA-2 for the 21-cm background resulting from standard physical processes (benchmark model). For the other models, only SKA-2 will be able to detect the signal $\Delta I_{\text{mod}} - \Delta I_{\text{st}}$. Again, targeting high temperature structures and observing at high frequencies will maximize the chance of detection. We have also addressed the possible source of contamination from point sources within the targeted cosmic structure, noting that the synchrotron radio signals decrease with redshift. Since the SZE-21cm is independent of redshift, targeting high redshift structures is ideal in getting rid of unwanted signals.

The possibility of NP distortions associated with plasma effects have been addressed using current CMB spectral data both at low and high frequencies. Upperlimits have been placed on the value of the plasma frequency at 1σ , 2σ and 3σ C.I. (206, 346 and 418 MHz) and it is found that low frequency measurements, < 400 MHz, are appropriate for

probing plasma effects on the CMB spectrum. Additionally, we have shown the impact of a non-zero plasma frequency associated with the CMB on the SZE and the cosmological 21-cm background. The SZE_{NP} spectrum shows peaks occurring at the corresponding plasma frequency which is independent of the cluster parameters such as temperature, minimum momentum or spectral index, but the amplitude of the peak does depend on the cluster parameters mentioned. The SZE_{NP} can be detected with current and upcoming instruments e.g. the SKA1 and SKA50% can set constraints on the plasma frequency at 1,2 and 3 sigma with 1000 hrs of observation whereas the eVLA can observe up to 3 sigma on the plasma frequency at 12 hrs of observation. Our results also show the importance of taking into consideration the plasma effects when recovering the 21-cm spectrum related to the EoR and the DA.

The final portion of the thesis is related to the polarization component of the SZE. We have been able to solve the polarized relativistic Boltzmann equation for the CMB photons and the electrons residing in cosmic structures and show that, when relativistic effects are taken into account, all the multipoles of the CMB are involved in the production of polarization. Similar to the SZE in intensity, relativistic effects become more pronounced on the polarization spectrum at higher temperatures and for cosmic structures where non-thermal activities are taking place. The SZE polarization associated with CMB octupole spectrum have been shown explicitly, revealing the existence of a cross-over frequency. The latter is sensitive to cluster parameters such as temperature, minimum momentum and spectral index of the electron distribution. The possibility of measuring the Q spectrum of the quadrupole and octupole spectrum through the use of multifrequency observations is discussed, stressing the importance of taking into account velocity effects and multiple scatterings. We have also been able to calculate the SZE polarization, highlighting the non-thermal component, of the Bullet cluster using SZE parameters derived from multifrequency measurements. The SKA together with ALMA and *Millimetron* have the capability of measuring the SZE polarization at 260 and 1000 hrs of integration time. In particular, combining ALMA and SKA, would allow the octupole and the quadrupole to be separated provided others additional factors such as velocity corrections and multiple scatterings are accounted for.

We have also shown that our approach of calculating polarization from comptonization process is valid at high energies and hence allowed us to compute the polarization flux up to 10 GeV. Comparison with the sensitivity of various telescope working at high energies, we saw that the polarization fluxes in the 1 keV–1 MeV and 0.1 MeV–0.1 TeV ranges are too small and therefore will be undetected.

We have presented the use of the SZE in a cosmological context, focusing on the intensity and polarized spectra that can be produced in cosmic structures. Our approach of computing the SZE and its polarization benefits from its generality, in sense that it is fully relativistic

and also allow to accommodate any general or combination of electron populations. We have seen that the impact of relativistic effects is substantial when calculating the SZE-21cm and this is important in order to recover the precise spectrum describing the processes occurring during the EoR and the DA. The error when neglecting relativistic effects is non-zero over most of the entire spectrum, in particular around $\nu \approx 50, 60, 77, 95$ MHz. Therefore, the use of the Kompaneets equation or any non-relativistic approach should be avoided as far as possible, in particular when high temperature cosmic structures are involved or the input spectrum is irregular. Relativistic impacts are also appreciated in the polarized component of the SZE, whereby all the multipoles are involved in the production of polarization even if the cosmic structure is at rest with respect to the CMB. Relativistic effects and the applicability to general electron populations, would allow the SZE signals (SZE-21cm or SZE_{NP}) and its polarization to be searched for even in cosmic structures where non-thermal activities are taking place, such as galaxy clusters hosting radio-halos or lobes of radio-galaxies.

SZE measurements benefit from differential measurements towards and away from cosmic structures. Exact calibration using an external source is not needed and also the signal is less vulnerable from galactic foregrounds larger than the angular extent of the cosmic structure. Therefore, the SZE is ideal for probing the EoR, NP spectral distortions and the multipoles of the CMB.

Until now, the SZE has always been envisaged as a useful tool to investigate the properties of the ICM and some other traditional cosmological applications such as measuring the Hubble constant, probing dark energy among others. In this present thesis, we have been able to extend the use of the SZE spectral distortion and demonstrate its relevance for cosmological background studies such as the 21-cm background related to the EoR and the DA and NP effects due to plasma frequency on the CMB at the recombination. We have also presented an extensive study of its polarization component with detail analysis of the spectra. Therefore the SZE and its polarization present themselves as very relevant tools to study the primordial induced spectral distortions of the CMB and also its multipoles at various time and location in the cosmos. The general approach of the SZE that we have presented shows that it is possible to probe any other backgrounds, such as the Cosmic Infrared Background.

In summary, following the methods used in this present work, it will be possible to obtain new and important information about the properties of the Universe. Even if the effects we discussed are small corrections w.r.t. the CMB intensity, we showed that with a high sensitivity instrument like SKA it will be possible to derive strong information on them. This confirms the big impact that SKA will have on our knowledge of astrophysics and cosmology.

Bibliography

- [1] Abazajian, K. N., 2007, *Phys. Rev. D.*, 75, 6, 063511
- [2] Ade, P. A. R. et al., 2011, *A&A*, 536, A8, 28
- [3] Ade, P. A. R. et al., 2014a, *A&A*, 571, A15, 60
- [4] Ade, P. A. R. et al., 2014b, *A&A*, 571, A29, 41
- [5] Ade, P. A. R. et al., 2016a, *A&A*, 594, A16, 62
- [6] Ade, P. A. R. et al., 2016b, *A&A*, 594, A13, 63
- [7] Ade, P. A. R. et al., 2016c, *A&A*, 594, A27, 38
- [8] Ade, P. A. R. et al., 2016d, *A&A*, 594, A11, 99
- [9] Andreani, P. et al., 1999, *ApJ*, 513, 23
- [10] Arnaud, M. et al., 2010, *A & A*, 517, 92
- [11] Backer, D. C. et al., 2010, HERA Hydrogen Epoch of Reionization Arrays, submitted for consideration by the Astro2010 Decadal Survey Program Panel RMS: Radio (Meter/Centimeter) and Millimeter/Submillimeter (2010)
- [12] Barkana, R., & Loeb, A., 2001, *Phys. Rept.*, 349, 125
- [13] Barkana, R., & Loeb, A., 2005a, *ApJ*, 624, L65
- [14] Barkana, R., & Loeb, A., 2005b, *ApJ*, 626, 1
- [15] Baumann, D., 2009, *arXiv:0907.5424*
- [16] Bennett, C.L et al. 2003, *ApJS*, 148, 1 [[astro-ph/0302207](#)]
- [17] Bennett, C. L. et al., 2013, *ApJS*, 208, 54
- [18] Berera, A. & Gordon, C., 2001, *Phys. Rev. D.*, 63, 063505
- [19] Bertone, G., Hooper, D., & Silk, J., 2005, *Phys. Rep.*, 405, 279

- [20] Beutler, F. et al., 2011, MNRAS, 416, 3017
- [21] Bharadwaj, S., & Ali, S. S. 2004, MNRAS, 352, 142
- [22] Birkinshaw, M., 1979, MNRAS, 187, 847
- [23] Birkinshaw, M. 1999, Phys. Rep., 310, 97
- [24] Blandford, R.D. & Narayan, R. 1992, ARA&A, 30, 311
- [25] Bohringer, H. & Werner, ARA&A, arXiv:0907.4277
- [26] Bonafede, A., Feretti, L., Giovannini, G., et al. 2009, A&A, 503, 707
- [27] Bradac et al., 2006, ApJ, 652, 937
- [28] Bromm, V., & Larson, R. B. 2004, ARA&A, 42, 79
- [29] Calstrom, J.E., Holder, G.P. & Reese, E. D., 2002, ARA&A , p 643-680, 40
- [30] Carilli, C. L., Furlanetto, S., Briggs, F., et al. 2004, New Astron. Rev., 48, 1029
- [31] Carilli, C. L., 2008, arXiv:0802.1727
- [32] Carroll, S., 1997, arXiv:gr-qc/9712019
- [33] Cavaliere, A., & Fusco-Femiano, R. 1976, A&A, 49, 137
- [34] Cavaliere, A., Danese, L. & De Zotti, G., 1977, ApJ, 217, 6
- [35] Challinor, A., Ford, M. & Lasenby A., 2000, MNRAS, 312, 1129
- [36] Chandrasekhar, S., 1960, Radiative Transfer, Dover, Mineola U.S.A.
- [37] Chen, X. L., & Miralda-Escude, J. 2004, ApJ, 602, 1
- [38] Chen, X. L. & Kamionkowski, M., Phys. Rev. D., 70, 043502
- [39] Chluba, J., Khatri, R. & R. A. Sunyaev, 2012, 425, 1129, [arXiv:1202.0057]
- [40] Chluba, J. & Sunyaev, R. A., 2012, 419, 1294
- [41] Chluba, J. et al., 2013, MNRAS, 430, 3054, [arXiv:1211.3206]
- [42] Chluba, J., 2014a, arXiv:1405.6938
- [43] Chluba, J. & Dai, L., 2014, MNRAS, 438, 1324
- [44] Choudhury, T. R., & Ferrara, A. 2006, ArXiv e-prints [arXiv:astro-ph/0603149]
- [45] Ciardi, B., & Ferrara, A. 2005, Space Sci. Rev., 116, 625

- [46] Clowe, D. et al., 2006, ApJL, 648, L109
- [47] Colafrancesco, S., Marchegiani, P. & Palladino, E., 2003, A&A, 397, 27-52
- [48] Colafrancesco, S., 2004, A&A, 422, L23-L27
- [49] Colafrancesco, S., 2005, A&A, 435, L9-L12
- [50] Colafrancesco, S., & Marchegiani, P. 2008, A&A, 484, 51
- [51] Colafrancesco, S. & Marchegiani, P., 2010, A&A, 520, A31
- [52] Colafrancesco, S., Marchegiani, P., & Buonanno, R. 2011, A&A, 527, L1
- [53] Colafrancesco, S., Marchegiani, P., de Bernardis, P. & Masi, S., 2013, A&A, 550, A92, 19
- [54] Colafrancesco, S., Emritte, M.S., Mhlahlo, N. & Marchegiani, P., 2014a, A&A, 566, 9
- [55] Colafrancesco, S., & Marchegiani, P. 2014b, A&A, 562, L2
- [56] Colafrancesco, S., Marchegiani, P., & Palladino, E. 2003, A&A, 397, 27
- [57] Colafrancesco, S. ,2009, S.A.It, 81, 104
- [58] Colafrancesco, S., Emritte, M.S., & Marchegiani, P., 2015a, JCAP, 05, 006
- [59] Colafrancesco, S., Beck, G. & Marchegiani, P., 2015b, JCAP, 02, 032
- [60] Colafrancesco, S. & Beck, G., 2016a, JCAP, 05, 013
- [61] Colafrancesco, S., Marchegiani, P. & Emritte, M. S., 2016b, A&A, 595, A21
- [62] Colless, M. et al., 2001, MNRAS, 328, 1039
- [63] Cooray, A. 2004, Phys. Rev. D, 70, 063509
- [64] Cooray, A. 2006, Phys. Rev. D, 73, 103001
- [65] Datta, K. K., Bharadwaj, S. & Choudhury, T. R., 2007, MNRAS, 382, 809-818
- [66] de Oliveira-Costa, A., Tegmark, M., Gaensler, B. M., et al. 2008, MNRAS, 388, 247
- [67] Dermer, C.D., 1986, ApJ, 307, 47
- [68] Dewdney, P., Turner, W., Millenaar, R., et al. 2012, SKA baseline design document, http://www.skatelescope.org/wp-content/uploads/2012/07/SKA-TEL-SKO-DD-001-1_BaselineDesign1.pdf
- [69] Dickinson Clive, 2016, arXiv:1606.03606

- [70] Dillon, J. S., Liu, A., Williams, C. L., et al. 2014, *Phys. Rev. D*, 89, 023002
- [71] Ding, X. et al., 2015, *ApJL*, 803, L22, 5
- [72] Dodelson, S., 2003, "Modern Cosmology", Academic Press.
- [73] Dvorkin, C., Blum, K. & Zaldarriga, M., *Phys. Rev. D.*, 87, 103522
- [74] Einasto, J., 2009, [arXiv:astro-ph/0901.0632]
- [75] Eisenstein, D. J. et al., 2005, *ApJ*, 633, 560-574
- [76] Eisenstein, D. J. et al., 2011, *ApJ*, 142, 72
- [77] Ellis, G. F. R., Treciokas, R. & Matrauers, D. R., 1983, *Annals. Phys.*, 150, 487
- [78] Emritte, M.S., Colafrancesco, S. & Marchegiani, 2016, *JCAP*, 07, 031
- [79] Ensslin, T. A., & Kaiser, C. R., 2000, *A&A*, 360, 417
- [80] Evoli, C., Mesinger, A., & Ferrara, A., 2014, *J.Cosmol.Astropart.Phys.*, 11, 024
- [81] Fargion, D. & Salis, A., *Phys. Usp.*, 41, 823
- [82] Feretti, L. 2001, in *Constructing the Universe with Clusters of Galaxies*, Eds. D. Gerbal and F. Durret
- [83] Feretti, L., et al. 2005, *A&A*, 444, 157
- [84] Feretti, L., 2012, *ARA&A*, 20, 54
- [85] Ferrari, C., Govoni, F., Schindler, S., Bykov, A. M. & Rephaeli, Y., 2008, *Space. Sci. Rev.*, 134, 93
- [86] Field, G. B. 1959, *ApJ*, 129, 536
- [87] Fixen, D. J. et al., 1996, *ApJ*, 473, 576
- [88] Furlanetto, S. R., & Briggs, F. H. 2004, *New Astron. Rev.*, 48, 1039
- [89] Furlanetto, S. R., Oh, S. P., & Briggs, F. H., 2006, *Phys. Repts.*, 433, 181 [arXiv:astro-ph/0608032]
- [90] Galli, S. et al., 2009, *Phys. Rev. D.*, 80, 023505
- [91] Garrett, K. & Duda G., 2011, *Ad. Ast.*, 968283
- [92] Giovannini, M. 2004, *Int.J.Mod.Phys.*, D13, 391
- [93] Gomez, P. et al., 2004, *AIP conf.ser.*, 361

- [94] Govoni, F. & Feretti, L. 2004, *Int.J.Mod.Phys*, D13, 1549
- [95] Hall & Challinor, 2014, *Phys. Rev. D*, 90, 063518
- [96] Halverson, N. W. et al., 2009, *ApJ*, 701, 42
- [97] Hansen, F. & Lilje, P., 1999, *MNRAS*, 306, 153-160
- [98] Hinshaw, G. et al., 2013, *ApJS*, 208, 19
- [99] Howell, T.F. & Shakeshaft, 1967, *Nature*, 216, 753
- [100] Hu, W. & Dodelson, S., 2002, *ARA&A*, 40, 171
- [101] Hu, W., 2003, *Annals. Phys.*, 303, 203
- [102] Huetsi, G., Hektor, A. & Raidal, M., 2009, *A&A*, 505, 999
- [103] Itoh, N., Kohyama, Y. & Nozawa, S., *ApJ*, 502, 7
- [104] Jaewon, Y. & Watanabe, Yuki, 2012, *International Journal of Modern Physics D*, 21, 1230002
- [105] Kamionkowski, M. & Loeb, A., 1997, *Phys. Rev. D*, 56, 4511
- [106] Kittel, C., *Introduction to Solid State Physics*, Wiley, New York U. S. A.
- [107] Kolb, E. W. & Turner, M. S., 1990, *The Early Universe*, Addison-Wesley, Redwood City
- [108] Komatsu, E. et al., 2009, *ApJS*, 180, 330-376
- [109] Komatsu, E. et al., 2011, *ApJS*, 192, 18
- [110] Kompaneets, A.S 1956, *Zh.E.F.T.*, 31, 876. Translation in *Sov. Phys. JETP*, 4, 730 (1957)
- [111] Kopmans, L., 2010, *The EoR/Dark-Ages & SKA in phase 1&2*
[[http://www.mrao.cam.ac.uk/projects/aavp/presentations/Koopmans EoR SKA1.pdf](http://www.mrao.cam.ac.uk/projects/aavp/presentations/Koopmans%20EoR%20SKA1.pdf)]
- [112] kovac, J. et al., 2002, *Nature*, 420, 772
- [113] Kravtsov, A.V & Borgani, S., 2012, *ARA&A*, 50, 353
- [114] Lavaux, G. et al., 2004, *MNRAS*, 347, 729
- [115] Liu, A., et al. 2013, *Phys. Rev. D*, 87, 043002
- [116] Liu, G.-C et al., 2016, *MNRAS*, 460, L104-L108
- [117] Loeb, A., & Barkana, R. 2001, *ARA&A*, 39, 19

- [118] Loeb, A., & Zaldarriaga, M. 2004, Phys. Rev. Lett., 92, 211301
- [119] Longair, M. 1994, High Energy Astrophysics, Cambridge University Press
- [120] Maartens, R., 2011, RSPTA, 369, 5115
- [121] Markevitch, M. et al., 2002, ApJ, 567, L27 [astro-ph/0110468] [INSPIRE]
- [122] Mather, J. C. et al., 1990, ApJL, 354, L37
- [123] Mather, J. C. et al., 1994, ApJ, 420, 439-444
- [124] McQuinn, M., et al. 2006, ApJ, 653, 815
- [125] Medvedev, M. V., 1999, Phys. Rev. E., 59, R4766
- [126] Mesinger, A., Furlanetto, S., & Cen, R. 2011, MNRAS, 411, 955
- [127] Marchegiani, P. & Colafrancesco, S., 2015, MNRAS, 452, 1328-1340
- [128] Marchegiani, P. & Colafrancesco, S., 2016, JCAP, 11,033
- [129] Malu, S. S. et al., 2010, arXiv:1005.1394 [INSPIRE]
- [130] Morales, M. F., & Wyithe, J. S. B. 2010, ARA&A, 48, 127
- [131] Nozawa, S. & Kohyama, Y., 2009, Phys. Rev. D., 79, 083005
- [132] Nozawa, S., Kohyama Y. & Itoh, N., 2009, Phys. Rev. D, 79, 123007
- [133] Ota, N. & Mitsuda, K., 2004, A&A, 428, 757
- [134] Paciga, G., Albert, J. G., Bandura, K., et al. 2013, MNRAS, 433, 639
- [135] Padmanabhan, T., 1995, Structure formation in the universe, Cambridge University Press
- [136] Padmanabhan, T., 2000, Theoretical Astrophysics, vol 1, Cambridge University Press
- [137] Padmanabhan, T., 2002, Theoretical Astrophysics, vol 3, Cambridge University Press
- [138] Padmanabhan, N & Finkbeiner, 2005, Phys. Rev. D., 72, 023508
- [139] Page, L. et al., 2007, ApJS, 170, 335
- [140] Parsons, A. R., Liu, A., Aguirre, J. E., et al. 2014, ApJ, 788, 106
- [141] Peebles, P. J. E., 1993, Principle of Physical Cosmology, Princeton University Press
- [142] Penzias, A. A. & Wilson, R. W., 1965, ApJ, 142, 419
- [143] Perlmutter, S., et al., 1999, ApJ, 517, 56

- [144] Plagge, T. et al., *ApJ*, 716, 1118
- [145] Portsmouth, J. & Bertschinger, E., 2004a, arXiv:astro-ph/0412094v1.
- [146] Portsmouth, J. & Bertschinger, E., 2004b, arXiv:astro-ph/0412095v1.
- [147] Portsmouth, J., 2004, *Phys. Rev. D.*, 70, 063504
- [148] Primack, J. R., 2015, arXiv: astro-ph/ 1505.02821
- [149] Pritchard, J. R., & Loeb, A. 2010, *Phys. Rev. D*, 82, 023006 [arXiv:1005.4057]
- [150] Pritchard, J. R., & Loeb, A. 2012, *Rep. Prog. Phys.*, 75, 086901 [arXiv:astro-ph/1109.6012]
- [151] Procopio, P. & Burigana, C., 2009, *A&A*, 507, 1243
- [152] Prokhorov, D. A. et al., 2011, *A&A*, 529, A39
- [153] Reichert, A. et al., 2011, *A&A*, 535, 4
- [154] Riess, A. G. et al., 1998, *ApJ*, 116, 1009
- [155] Rudnitskiy, A. G., 2015, Istituto di Radioastronomia Bologna, Bologna Italy.
- [156] Rybicki, G. B. & Lightman, A. P., 1979, *Radiative Processes in Astrophysics* (New York Wiley)
- [157] Sachs, R. K. & Wolfe, A. M., 1967, *ApJ*, 147, 73
- [158] Sanderson, A. J. & Ponman, T. J., *MNRAS*, 402, 65-72
- [159] Sarazin, C. L., 1986, *Rev. Mod. Phys*, 58, 1-115
- [160] Sarkar, S.: 1996, *Reports on Progress in Physics*, 59, 1493
- [161] Sazonov S.Y. & Sunyaev R.A., 1999, *MNRAS*, 310, 76
- [162] Scott, D., & Rees, M. J. 1990, *MNRAS*, 247, 510
- [163] Shimwell, T. W. et al., 2014, *MNRAS*, 440, 2901-2915
- [164] Senatore, L., 2016, arXiv:1609.00716v1
- [165] Silk, L. & White, S. D. M., 1978, *ApJ*, 226, L103
- [166] Sironi, G. et al., 1990, *ApJ*, 357,301
- [167] Sironi, G., Bonelli, G. & Limon, M., 1991, *ApJ*, 378, 550
- [168] Skivie, P., 2009, ArXiv e-prints: 0909.0949

- [169] Smoot, G. F. et al., 1992, ApJL, 396, L1-L5
- [170] Smoot, G. F., 1997, astro-ph/9705101 [INSPIRE]
- [171] Spergel, D. et al., 2003, ApJS, 148, 175
- [172] Spergel, D. et al., 2007, ApJS, 170, 377
- [173] Steigman, G., 2004, Measuring and Modeling the Universe, from the Carnegie Observatories Centennial Symposia. Published by Cambridge University Press, as part of the Carnegie Observatories Astrophysics Series, edited by W. L. Freedman, 169
- [174] Sunyaev, R.A. & Zeldovich, Ya.B., 1970. Ap&SS, 7, 3
- [175] Sunyaev, R.A. & Zeldovich, Ya.B., 1972. Comments Ap&SS, 4, 173
- [176] Tashiro, H., 2014, Prog. Theo. Exp. Phys., 36, 1095
- [177] Trigger, S. A. & Khomkin, A. L., 2010, Plasma. Phys. Rep, 36, 1095
- [178] Trimble, V., 1987, ARA&A, 25, 425
- [179] Turner, M. S. & Tyson, J. A., 1999, Reviews of Modern Physics Supplement, 71, 145
- [180] Valdes, M., Evoli, C., Mesinger, A., Ferrara, A., & Yoshida, N. 2013, MNRAS, 429, 1705
- [181] Weller, J. Battye, R. & Kneissl, R., Phys. Rev. Lett., 88, 231301
- [182] Wik, D. R., et al., 2014, ApJ, 792, 48
- [183] Wouthuysen, S. A. 1952, AJ, 57, 31
- [184] Yasini, S. & Pierpaoli, E., 2016, Phys. Rev. D., 94, 023513
- [185] Yoshida, N., 2009, arXiv:0906.4372v1
- [186] Zackrisson, E., 2005, Introduction to Dark Matter, Thesis excerpts *Quasars and Low Surface Brightness Galaxies as Probes of Dark Matter*, Uppsala University
- [187] Zaroubi, S. 2013, The First Galaxies, Astrophys. Space Sci. Libr., 396, 45
- [188] Zel'dovich, Ya.B. & Sunyaev, R., A., 1969, Ap & SS, 4, 301
- [189] Zemcov, M. et al., 2010, A&A, 518, L16
- [190] Zwicky, F., 1933, Helvetica Physica Acta, 6, 110
- [191] [http://www.core-mission.org/documents/CoreProposal Final.pdf](http://www.core-mission.org/documents/CoreProposal%20Final.pdf).
- [192] <http://astromev.in2p3.fr/?q=aboutus/pact>

Appendix A

Fractional error analysis

In this appendix, we investigate using the four models of Fig 2.2, the relationship between the error produced when using a non-relativistic approach and the properties of the input radiation field.

For the standard SZE, the input radiation is the usual Planck spectrum, which at low frequency has a constant brightness temperature, and the resulting SZE ΔT_{st} is a constant as well (see Fig 2.4). It is important to note that the Planck spectrum is a smooth function, and as a result of this smoothness, the difference between the use of a relativistic approach and a non-relativistic approach in calculating the SZE is small for low electron temperatures and at low frequencies (see, e.g., Colafrancesco et al. 2003). However, the 21-cm background is not a smooth function and the spectral shape plays an important role in the determination of the error when neglecting relativistic effects.

To start our discussion on this issue, we show the spectra of the SZE-21cm in the relativistic and non-relativistic case for a temperature of 7 keV using our four models of the 21-cm background (see Fig A.1-A.4). In addition, we show as well, the standard SZE for the relativistic and non-relativistic case. It is noticed that the use of the non-relativistic approach introduces an overall numerical error into the standard SZE, and that this error is amplified in a frequency-dependent way for the SZE-21cm.

To study the spectral behaviour of the error, we also show the fractional error done in these cases, and we compare these results with the properties of the input spectra. As discussed in section 2.5.2, we expect that the most important factor in determining the error done with the non-relativistic approach is the curvature of the input radiation spectrum: if the input spectrum has a large curvature this implies that using a function $P_1(s)$ that is narrower than the correct relativistic one (like in the non-relativistic approach) gives a result that is more different than in the case where the input radiation field is smooth, such as the Planck spectrum of the CMB.

To check this conclusion, the same analysis is performed on the other models.

The maximum (minimum) points of the fractional error between the relativistic and non-relativistic results occur at frequencies where there is a peak (trough) in the second derivative, which corresponds to a maximum (minimum) in the input spectrum.

We noticed in the first model (solid line Fig 2.2) that two peaks occur within the frequency range 60-80 MHz in the non-relativistic case (see Fig A.1 (dashed line)). This can be explained by the fact that there are two peaks in the second derivative of the input spectrum and also that the non-relativistic approach introduces artifacts as a result of the convolution of the input spectrum with a narrow kernel. With the correct relativistic kernel, the input spectrum is convolved with a wider function and the two peaks are then smoothed in only one peak. Therefore, the use of a non-relativistic approach produces a spectrum which then gives incorrect value and shape of the SZE-21cm and the error becomes more significant as temperature is increased.

In the other models that we have considered, only one peak occurs within the frequency interval 60-70 MHz for the second derivative which as a result the non-relativistic SZE-21cm has only one peak in this frequency interval as well (Fig A.1-A.4). One can also noticed the occurrence of peak/troughs in the fractional difference at frequencies where peak/troughs occurs in the second derivative of the input spectrum (e.g. at ≈ 153 MHz for the second model). This demonstrate that the smoothness of the input radiation is an important factor that plays an important role in the error introduced between the relativistic and non-relativistic approach.

To conclude, we have shown in this Appendix that there is a substantial numerical error when computing the SZE using a non-relativistic approach, in particular when the input radiation spectrum is not a smooth function, as in the case of the modied CMB giving rise to the 21-cm background. This means that when using SZE of cosmic structures to study the cosmological 21-cm, it is imperative to use a full relativistic computation in order to obtainthe correct SZE amplitude and its spectral shape.

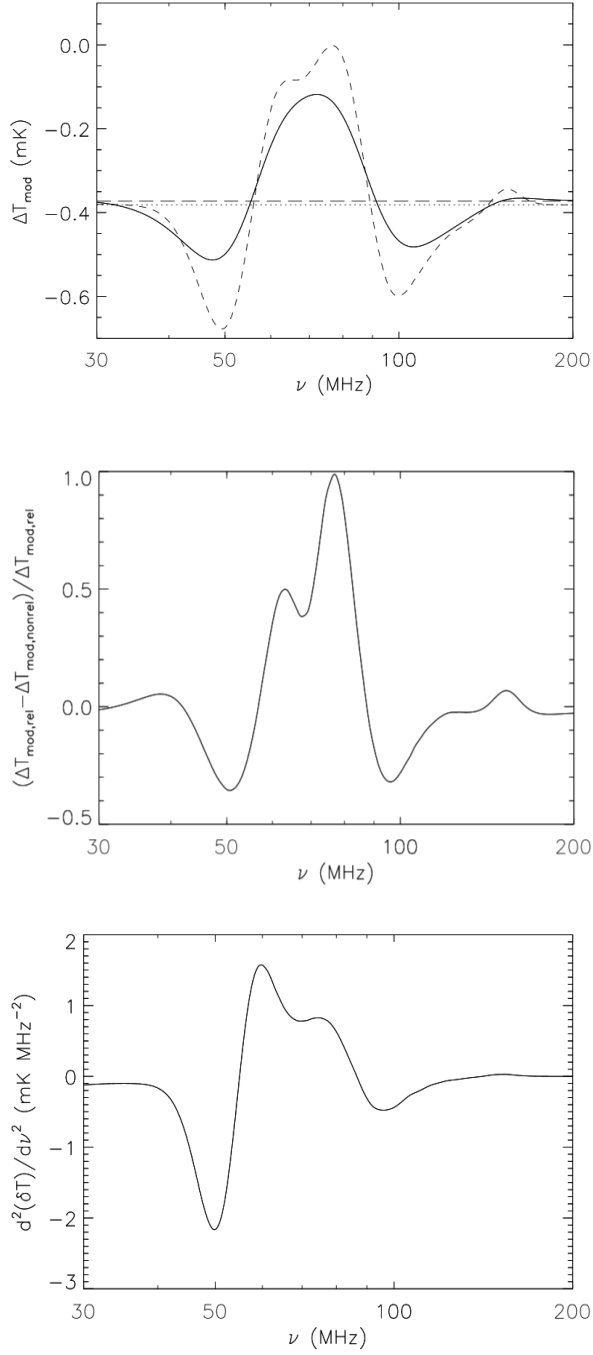


Figure A.1: Spectral analysis of the first model (solid line of Fig 2.2). Top-panel :The relativistic (solid) and non-relativistic SZE-21cm (dashed line) together with the standard relativistic (long-dashed line) and non-relativistic SZE (dotted line) calculated for a thermal plasma of temperature 7 keV and optical depth 5×10^{-3} . Middle-panel: The fractional difference between the relativistic and non-relativistic results. Bottom-panel: Second derivative of the input spectrum.

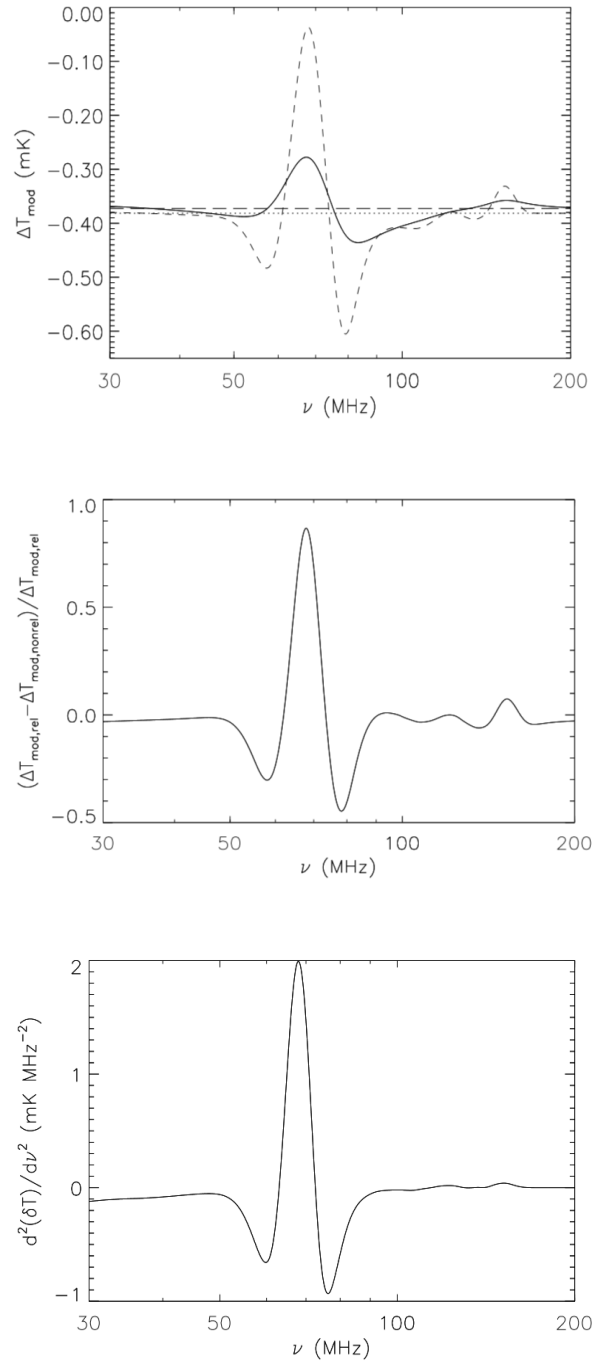


Figure A.2: Same as Fig A.1 for the second model (dashed line in Fig 2.2).

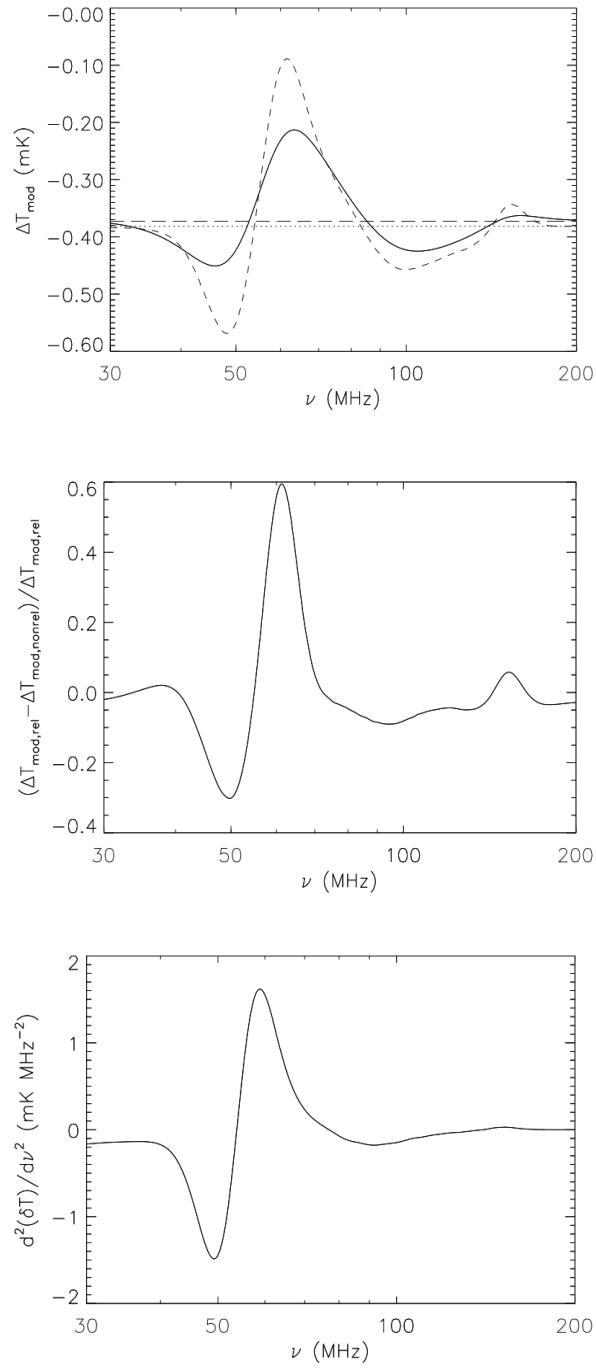


Figure A.3: Same as Fig A.1 for the third model (dashed line in Fig 2.2).

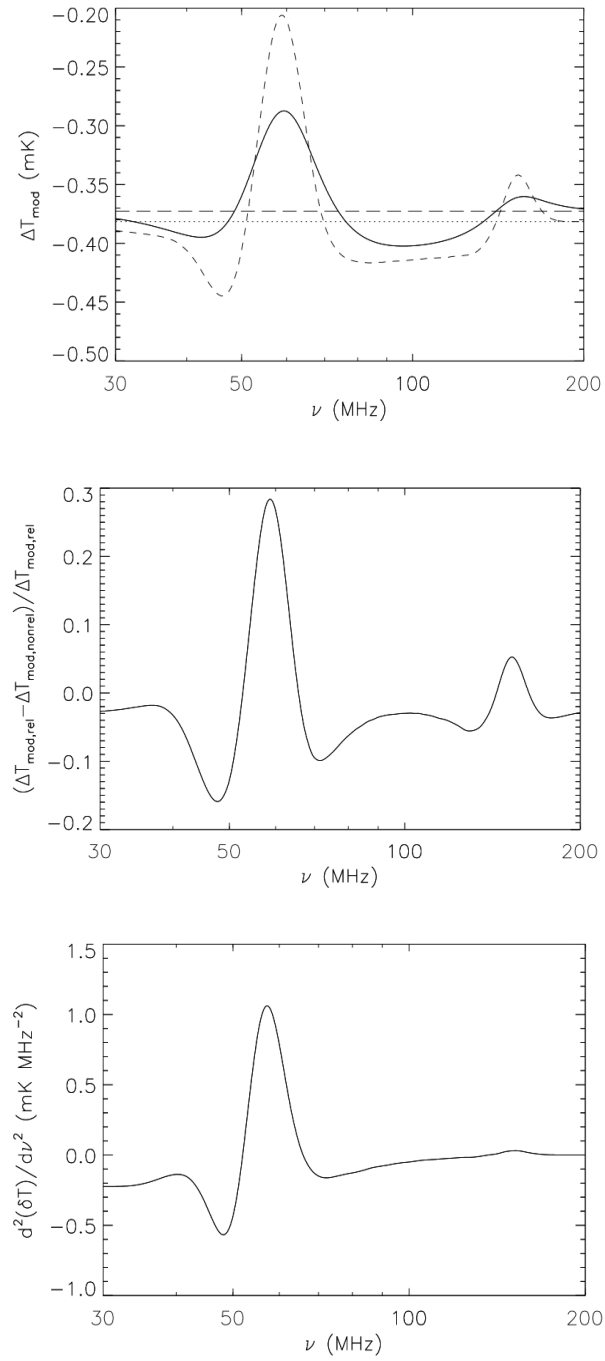


Figure A.4: Same as Fig A.1 for the fourth model (dashed line in Fig 2.2).